Spring 1994

Neutral gas plasma interactions in space plasma

Kan Liou
University of New Hampshire, Durham

Order Number 9506424

Neutral gas plasma interactions in space plasma

Liou, Kan, Ph.D.

University of New Hampshire, 1994

U·M·I

300 N. Zeeb Rd.
Ann Arbor, MI 48106

NEUTRAL GAS PLASMA INTERACTIONS IN SPACE PLASMA

BY
Kan Liou
B. A., National Central University, ROC, 1983
M. S., National Central University, ROC, 1985
M. S., University of Alabama in Huntsville, USA, 1988

DISSERTATION

Submitted to the University of New Hampshire
in Partial Fulfillment of
the Requirements for the Degree of

Doctor of Philosophy
in
Physics

May, 1994

This dissertation is dedicated to

my parents, my family, and my wife

whose love and encouragement

made this work possible.

ACKNOWLEDGEMENTS

I would first like to express my sincere appreciation to my advisor, Professor Roy Torbert, for his wisdom and guidance throughout the past five years. I appreciated and enjoyed the opportunity to work for Professor Torbert, and also the intellectual freedom with which I was allowed to conduct this research. I would like to thank Dr. Craig Kletzing for his countless and patient instructions on the field of experimental space physics. I want to thank Dr. Terry Onsager for his enthusiastic and valuable discussions on many plasma physics questions. I also want to thank Professor Roger Arnoldy, Professor Harvey Shepard, Professor Richard Kaufmann, and Professor Eberhard Möbius for serving on my committee and reviewing the manuscript.

I have highly valued the friendship, help, and thoughtfulness of my fellow students here in the past several years. Bill Peria (Mr. IDL with unlimited patience), Laurence Janoo (tough to beat at badminton), and Eric Dors (impetuous but very smart young student).

I am appreciative of the help of several of the support staff associated with the Experimental Space Plasma group in making my work easier. David Rau and Vincent Ye deserve special commendation for their valuable help.

The author gratefully acknowledge the financial support provided by NASA grant NAG-5-656.

Contents

List of Tables

List of Figures

ABSTRACT

NEUTRAL GAS PLASMA INTERACTIONS IN SPACE PLASMA

by

Kan Liou

University of New Hampshire, May, 1994

A sounding rocket experiment, CRIT-II, involving the injection of shaped-charge barium in ionospheric plasma was conducted on May 7, 1989, to investigate Alfvén's critical ionization velocity (CIV) hypothesis in space. The CRIT-II main payload was instrumented to make *in situ* measurements within the neutral barium beam. Among the detectors, UNH provided three energetic particle detectors and two photometers. The data from these detectors are presented. The typical features of the CIV effect were observed including plasma density enhancement, energy and momentum loss of a fast ion beam, excitation of plasma waves, and electron heating. It was found by optical observations that about 4% of the neutral barium was ionized. We believe that about one half of these barium ions were created by electron impact ionization – a CIV mechanism. The cross section for collisions between the barium atoms and the ionospheric oxygen ions was also calculated, assuming that the other half of ionizing barium ions were mainly generated by charge exchange, and found to be in the range from $1 \times 10^{-17}\ cm^{-2}$ at a velocity of 4 km/s to $1 \times 10^{-15}\ cm^{-2}$ at a velocity of 20 km/s. We also confirmed that the early observed ions were originally from the collisionally accelerated neutral oxygen which charge exchanges with the local oxygen ions. The early stage of electron heating was confirmed to be the result of lower hybrid instabilities excited by the precursor ion beam, using our quasi-linear model calculation. However, the wave spectrum during the passage of main

streaming barium was found to be inconsistent with the lower hybrid instabilities proposed by current CIV theories. This could be the main reason for a relatively low ionization yield that one otherwise would expect from CRIT-II. A multi-fluid model of the wave dispersion relation for an unmagnetized beam with finite width in a magnetized plasma was also derived. We found that the nonuniform beam density effect could be the main driver which altered the plasma wave spectrum from the typical lower hybrid waves. A quasi-DC electric field model based on the momentum coupling between an ionizing barium beam and an ionospheric plasma was developed. we found that CIV is a self-limiting ionization process in a conical type of neutral beam, which may have caused the low ionization yield in most of the shaped-charge CIV experiments.

CHAPTER 1

Introduction

Speculations about the origin of the celestial bodies must have started as soon as human consciousness, but the evidence needed to develop a scientific theory has been available for only 300 years. Since first raised by the Greeks, the question of the origin of the solar system has been frequently thought solved, but the wide variety of explanations including from the mythic creation by primitive societies to the highly imaginative universe by philosophers and to the more numerous recent attempts by scientists, have generally collapsed when faced with new information about the system. The principal difficulty to this fundamental question is due to the lack of information about the solar system, which extremely restricts us from acquiring the true answer. It is, therefore, no surprise that the origin of the solar system is still one of the oldest scientific questions to be resolved.

The solar system, besides the central body, the Sun, consists of nine known planets, 56 satellites discovered to date, and innumerable asteroids, comets, and meteoroids that orbit the Sun. One would intuitively ask whether our planetary system is a unique feature or just a special phenomenon. Unfortunately this question is beyond the scope of present knowledge. Even a planet like the Earth surrounded by a relatively large Moon may not be duplicable - except by chance. However, it

seems that most thinkers are driven by the wish to make planetary systems like ours common in the universe. Let's imagine about two billion years ago, the solar system was not yet completely formed, but a protosystem which simply consisted of a central body and homogeneous surrounding materials. Unlike the present planetary and satellite system, the surrounding materials consisted of the basic chemical elements in a form of gas atoms and plasmas which uniformly covered the central body. The size of this protosystem could have been much bigger than that of our present solar system. Due to the gravitational central force, the surrounding neutral gas started to fall in towards the central body. Due to electromagnetic interactions this gas may have been ionized and trapped by the central body's magnetic field at certain distances. The ionized gas was rooted in that region to form a secondary body by accretion. In a similar fashion, The non-ionized portion of the neutral gas continued to fall until it ionized and created another secondary body and so on. The location of these newly formed secondary bodies roughly corresponds to the present location of main groups of planets. At the late stage of the formation of the giant planets a similar process occurred around these bodies which led to the formation of the satellites.

This conjecture originated from Alfvén's highly speculative hetegonic theory developed in his book of "On the Origin of the Solar System" [Alfvén, 1954]. He started it out with analyzing the most abundant elements in the solar system and found that they can be categorized into three bands of ionization velocities, one for $v_{c1} = 5-7\ km/sec$, one for $v_{c2} = 13-16\ km/sec$, and one for $v_{c3} = 35-40\ km/sec$. Alfvén concluded that there would be three discrete bands of secondary bodies as a function of the distance from the central body. He suggested that these three

bands of abundances could have been braked from free falling gas due to ionization at different locations from the sun. Since the further the gas falls towards the sun, the higher its velocity, therefore this stopping distance can be determined by equating the gravitational energy with the ionization energy of infalling particles, *i.e.* $GM_cM/R_c = e\phi_{ion}$, where G is the gravitational constant, M_c is the mass of the central body, M_n is the mass of an atom of the gas cloud, R_c is the distance corresponding to a velocity V_c such that the kinetic energy of the atom is equal to its ionization energy. Based on this assumption, he reached a fairly satisfying result for the mass distribution for present solar planetary and satellite systems as illustrated in figure 1.1.

However, controversies with Alfvén's hetegonic theory have remained. Besides the major fatal objection of no correlation between elemental abundances and the ionization potentials of the elements, which should be expected on the basis of such a theory, the hypothesis of Critical Ionization Velocity (CIV) effect, the heart of Alfvén's hetegonic theory, is probably the biggest one among them. The CIV hypothesis [Alfvén, 1960], after generalizing its original assumption, predicts that an anomalous gas ionization occurs if the relative velocity between a neutral gas and a plasma perpendicular to the magnetic field exceeds the critical velocity determined by

$$V_c = \sqrt{\frac{2e\phi_{ion}}{M_n}} \tag{1.1}$$

where e, ϕ_{ion} and M_n are the unit charge, ionization potential, and mass of the neutral particles. According to this hypothesis, the relative velocity between the gas and plasma will be rapidly reduced until it reaches V_c.

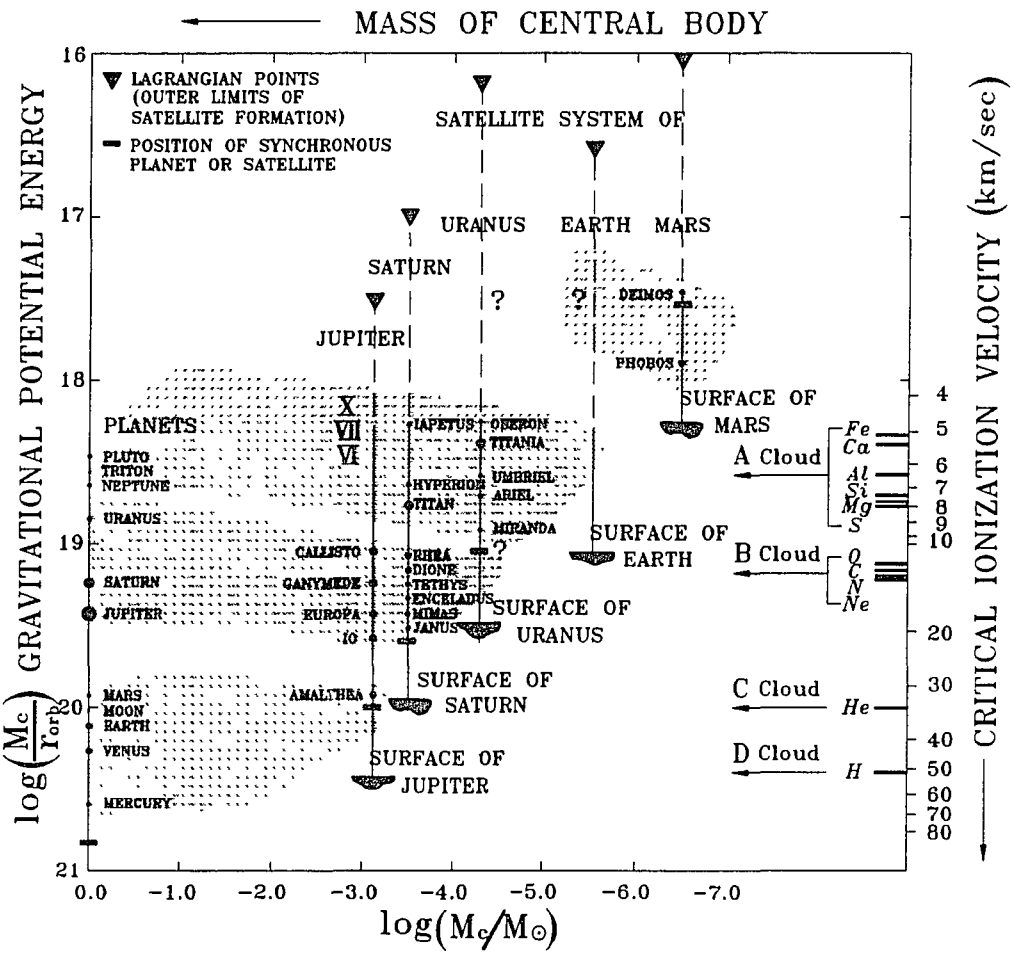

Figure 1.1: Structure of solar planetary and satellite system in terms of gravitational potential energy, the mass of the central body, critical ionization velocity. The A, B, C, and D clouds proposed by Alfvén are shown on the right (from Alfvén and Arrhenius, 1976).

Although the Alfvén's hetegonic theory has not been accepted, the idea of the CIV effect has been drawing a lot of attention, and the task concerning the identification of CIV hypothesis has been an active subject in experimental and theoretical plasma physics. Over 200 papers associated with the research of CIV have been published during the last three decades. Instead of going through all of the research reports in order to familiarize oneself with the history of CIV - it seems impractical and impossible, a review paper is probably the best alternative. The first comprehensive review of CIV laboratory experiments was given by Danielsson [1973] accompanying a theory review by Sherman [1973]. A brief review of both CIV experiments and theories was given later by Raadu [1981] followed by Möbius [1983] which concerned the space CIV experiments. A concise review of chemical releases in the ionosphere and its application to CIV was first given by Newell [1985]. However the most comprehensive CIV review concerning both space and laboratory experiments, as well as the existing theories up date, was recently given by Brenning [1992].

The subject of this chapter is to provide a basic guide to the research territory of CIV. The context will be ordered as follows. The laboratory experimental results will be briefly described in the first section. In section two the experiments of CIV in space will be introduced in a case by case fashion. The current theories concerning the CIV process will be concisely described in section three and followed by a brief discussion of possible applications of the CIV effect.

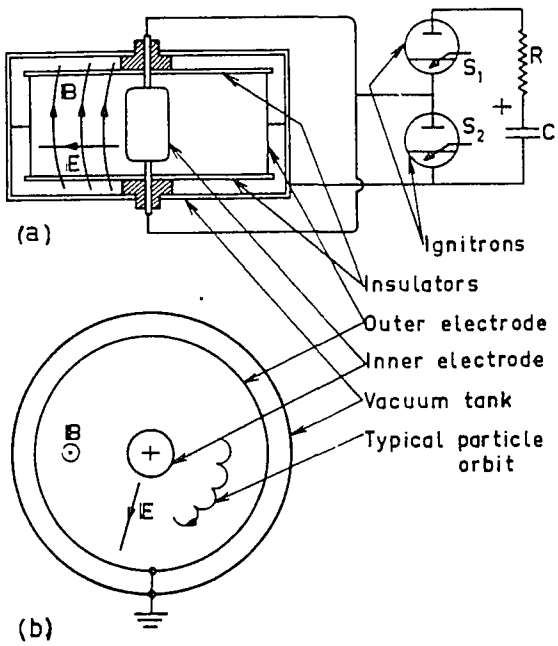

Figure 1.2: Rotating plasma device. (a) Front view: Electrical connections sketched. (b) Seen from above (from Fahleson, 1961).

1.1 Laboratory Search for CIV

Early attempts to verify the CIV hypothesis were started and carried out in the laboratory, and most of the experiments were conducted in a homopolar machine [Fahleson, 1961; Angerth et al., 1962; Himmel and Piel, 1973; Himmel et al., 1977], coaxial plasma gun geometry [Wilcox et al., 1964; Eninger, 1966; Axnäs, 1972] and impact plasma device [Danielsson, 1970; Danielsson and Brenning, 1975]. The homopolar machine is a co-axial cylindrical electrode with magnetic field applied along the axis. A rotating plasma driven by the $E \times B$ force was created to pass through a number of different neutral gases which were at rest (see figure 1.2).

Instead of measuring the relative velocity between the neutral gas and rotating

plasma, the saturation voltage of a gas discharge was measured. It was found interestingly that the plasma rotation velocity E/B was maintained constant throughout the anomalous discharge phase until the neutral gas was completely ionized. It was also found that E/B was close to the Alfvén's critical velocity given by equation (1.1) for all investigated gases over a wide range of parameters, such as magnetic field, gas pressure, and current. Although the identification of E/B as the plasma velocity is not quite justified, since in many cases the ion hall parameter is small and the ion motion is essentially in the direction of the electric field, the role of the CIV in the voltage limiting effect was established experimentally but the details of how the discharge phenomenon is connected to the CIV were still little understood.

In some respects the plasma gun type of arrangement is advantageous compared to rotating plasmas when studying the interaction between a plasma and a neutral gas. In this type of experiment an ionizing front is travelling through a neutral gas. The phenomenon in the front and in the plasma moving behind it are studied. It is much easier to observe the plasma velocity directly in this configuration. Futhermore, there are no centrifugal effects involving the plasma motion. Another important difference between this arrangement and rotating plasma device is that the magnetic field lines nowhere pass from the plasma into the wall where recombination can take place and give rise to neutral gases which can interact with the plasma to limit the electric field.

In the coaxial plasma gun device [Eninger, 1965], a toroidal sheath of plasma was driven along the axis of the discharge tube by the $J \times B$ force of a radial current across an azimuthal magnetic field. The magnetic field was generated by a separate current through the central electrode (see figure 1.3).

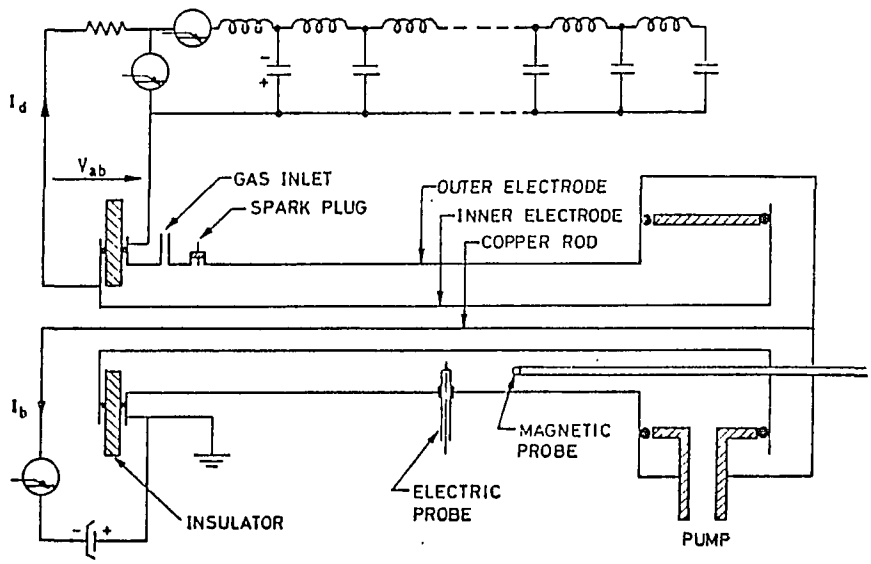

Figure 1.3: Schematic drawing of plasma gun and electric circuits (from Eninger, 1965).

The observations in this device were much more easily interpreted in terms of velocity than in the homopolar case: the problem with differential azimuthal rotation is eliminated, and an ionization front which has the same velocity everywhere is obtained by electric and magnetic fields which are both inversely proportional to the radius, as the vacuum fields. Futhermore, Doppler-shift measurements of the sheet velocity can be made at one radius, while such a measurement must be made along a chord in the homopolar geometry.

It was found that the ratio of saturation voltage to magnetic field is dependent on the gas used. The ratio E/B was independent of the plasma current and gas pressure over four orders of magnitude of these parameters.

The impact experiments are more directly applicable to the type of situations of interest in space plasmas in the sense that no external energy is applied during

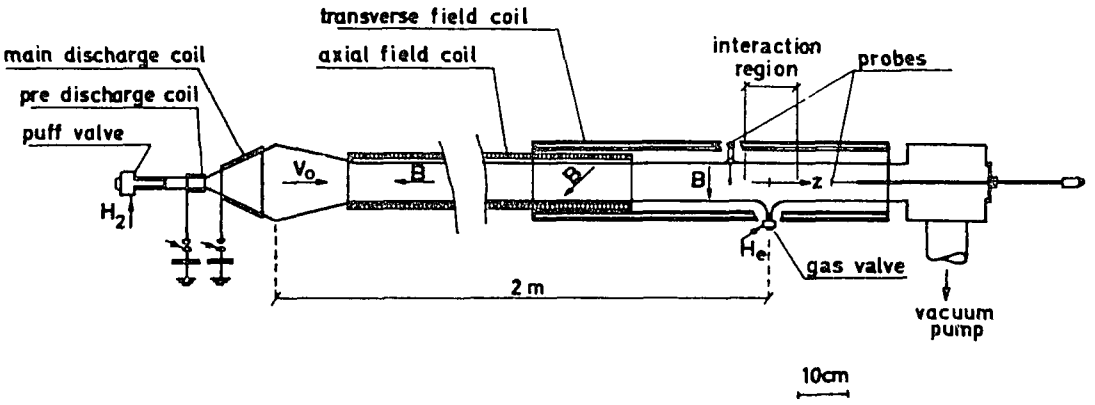

Figure 1.4: Experimental arrangement of Danielsson [1969].

the interaction. A fully ionized plasma is generated by a conical theta pinch and accelerated into a drift tube along a magnetic field (see figure 1.4). The magnetic field gradually changes direction into a transverse magnetic field. The field strength of this transverse field is maintained constant throughout the tube. As a plasma proceeds along this drift tube, a polarization electric field is developed and part of the plasma ends up drifting across the transverse magnetic field. A neutral gas is injected into the gun by a fast electromagnetic valve to make contact with the drifting plasma in the transverse magnetic field region.

In this type of experiments, the collisions of plasma with neutral gas were carefully excluded except the electron-atom collisions. The velocity of the plasma was determined by measuring the polarization electric field in the transverse magnetic field. It was found that the plasma is very efficiently retarded as it penetrates into the gas cloud. At the same time the electron energy distribution is found to change drastically toward higher energies, at least for a part of the population, and partial ionization of the gas is established.

To briefly summarize the laboratory CIV experiments, the occurrence of the critical velocity phenomenon has been first indirectly identified in the rotating plasma. The collisionless nature of the CIV process has been clearly demonstrated by the impact experiments. Moreover, the number of hot electrons has now been quantified . Finally, anomalous momentum loss has been observed, that exceeds the rate due to the ionization. In all CIV experiments, the presence of anomalous electron heating has become evident. Turbulent heating by means of a modified two stream instability has been proposed as the central step in the CIV process [Sherman, 1972]. The condition for onset of the modified two stream instability have been verified in rotating plasma [Piel et al., 1978]. However, due to the parameter regimes where the laboratory experiments were performed, the time scale of laboratory experiments is such that a detailed study of the development of instabilities, the waves spectrum, and the electron distribution is hardly conceivable. To conclude, the wide variety of observational evidence has formed a firm structure for the CIV model, the only thing left is to fill in the details and to determine whether it appears in space.

1.2 Space Search for CIV

Active experiments on the critical velocity effect in space have been performed more than a dozen times over the last two decades (see Table 1.1). Most of them were carried out by injecting an artificial shaped-charge gas, usually Ba ($v_c = 2.7\ km/s$) or Sr ($v_c = 3.5\ km/s$), into an ionospheric plasma either transverse or oblique to the geomagnetic field with typical velocities ranging from a few km/s to 15 km/s. An alternative attempt at an orbital spacecraft release in the upper ionosphere has been conducted recently by CRRES project. The neutral gas cloud is released by

thermite evaporation with a typical orbital velocity of 8 km/s.

Table 1.1: Summary of ionospheric chemical release experiments for CIV effect and their results (from Torbert).

Rocket Chemical Jet Experiments				
Experiment	Year	Beam type	Angle to B	Prompt Yield
Chachalaca	1972	Ba Conical(30°)	$10° - 15°$	few%
Porcupine	1979	Ba Conical(15°)	28°	$\sim 10\%$
Bubble Machine	1982	Ba+1%Sr Radial	90°	$\sim 0\%$
Star of Lima	1983	Ba Conical(20°)	90°	$< 0.2\%$
Star of Condor	1983	Sr Radial	all angle	$< 0.003\%$
SR90	1986	Sr Conical(15°)	48o	0.17%
CRIT-I	1986	Ba Conical(15°)	48°	$< 0.5\%$
CRIT-II	1989	Ba Conical(15°)	57°	$2 - 4\%$
Satellite Orbital Thermite Release Experiments				
CRRES-CIV I	1990	Ba	80°	
CRRES-CIV II	1990	Ba	79°	3.4%
CRRES-CIV I	1990	Sr	80°	0.33%
CRRES-CIV II	1990	Ca	80°	0.31%

The advantage of the space CIV experiment is to diminish the importance of the boundary conditions, and hence provides a closer look of the Alfvén's original CIV hypothesis. Futhermore, the time and length scales enable scientists to diagnose the microstructure of CIV interactions. On the other hand, space CIV experiments are expensive and the conditions in which the experiments are conducted are usually not controllable or repeatable. All of which usually make the measurements difficult.

A summary of the results of space CIV experiments is shown in Table 1.1. It's clear to see that all of the space CIV experiments, contrary to the laboratory experiments, have indicated negative results except Porcupine [Haerendel, 1982a] and probably CRIT-II [Torbert et al., 1992; Stenbaek-Nielsen et al., 1990b]. A comparison among each of them, however, is not quite obvious because they were carried out

Table 1.2: Parameters of ionospheric CIV experiments.

Experiment	$N_n(cm^{-3})$	$N_e(cm^{-3})$	B(Gauss)	ω_e/Ω_e	$v_A(km/s)$
Chachalaca		?			
Porcupine		6×10^5	~ 0.3	8	210
Bubble Machine		?			
Star of Lima	6.7×10^7	$2 - 3 \times 10^4$	0.22	2.5	700
Star of Condor	2×10^8	?	0.22		
SR90		1.5×10^4			
CRIT-I	4×10^7	3.3×10^4	0.44	1.3	1320
CRIT-II	1.7×10^8	5.4×10^5	0.43	5.5	320
CRRES-CIV I	5.1×10^7	3.4×10^6	0.31	19	92
CRRES-CIV II	2.4×10^7	1.5×10^6	0.35	11	156
CRRES-CIV I	4.9×10^7	3.5×10^6	0.31	19	90
CRRES-CIV II	2.5×10^7	1.6×10^6	0.35	12	151

at much different situations and most of them lack *in situ* measurements. Table 1.2 shows the experimental conditions for each of the experiments. We will also make a brief discussion and summary of each of the experiments in the rest of this section.

1.2.1 Chachalaca

Not intended for CIV experiments, Chachalaca was an attempt to do geomagnetic field tracing at the auroral zone. A 30° conical shaped-charge barium was injected upward from the Earth's shadow to sunlight into the magnetosphere oblique to the local geomagnetic field line by 10° [Wescott et al., 1975]. This barium release was intended to be carried out in the sunlight such that it, after photoionization, could be tracked by television and camera systems on the ground. Owing to a partial rocket malfunction, the detonation took place 56 *km* below the solar UV screening height. The differential velocity distribution of ions with initial velocities of at least 20 km/s were observed, with appreciable density distributed between 9 and 15 km/s

and peak density near 12 km/s [Wescott et al., 1975]. Considering the geometry of the cone angle width and the velocity distribution, a small fraction of barium had perpendicular velocity greater than critical velocity. It was analyzed that a few percent of the barium was ionized before it was exposed to sunlight. Although the ionization mechanism was not fully understood, it is believed that no classical ionization mechanism can give this significant barium ion yield so rapidly. Thus, it is suggestive of the operation of the critical ionization velocity effect.

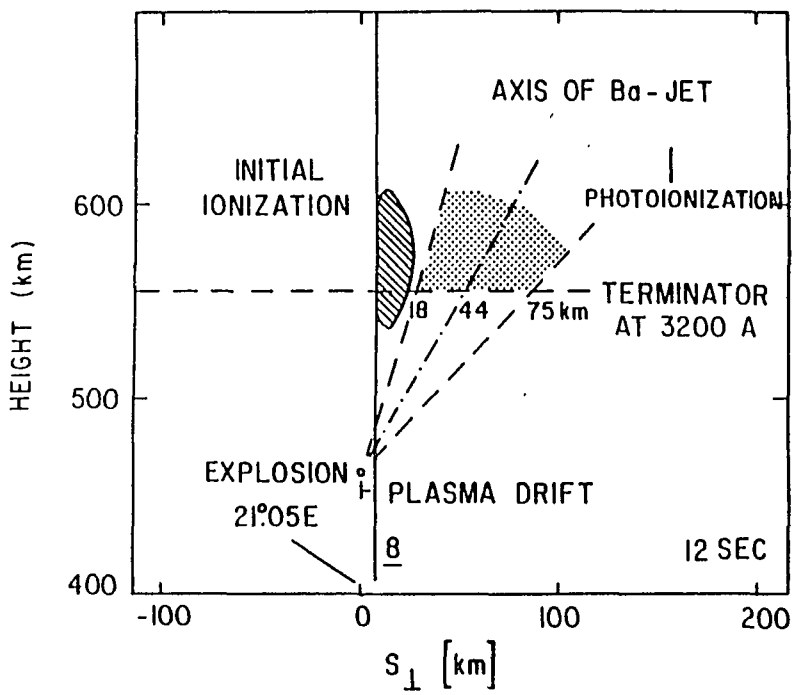

Figure 1.5: Geometry of the Ba gas jet injected from the Porcupine rocket above ESRANGE on March 19, 1979. The shaped-charge was ignited about 100 km below the terminator with the axis inclined towards the east by 28° (from Haerendel, 1982).

1.2.2 Porcupine

The most persuasive experimental result to support Alfvén's CIV hypothesis was given by Project Porcupine [Haerendel, 1982a]. The geometry was similar to that

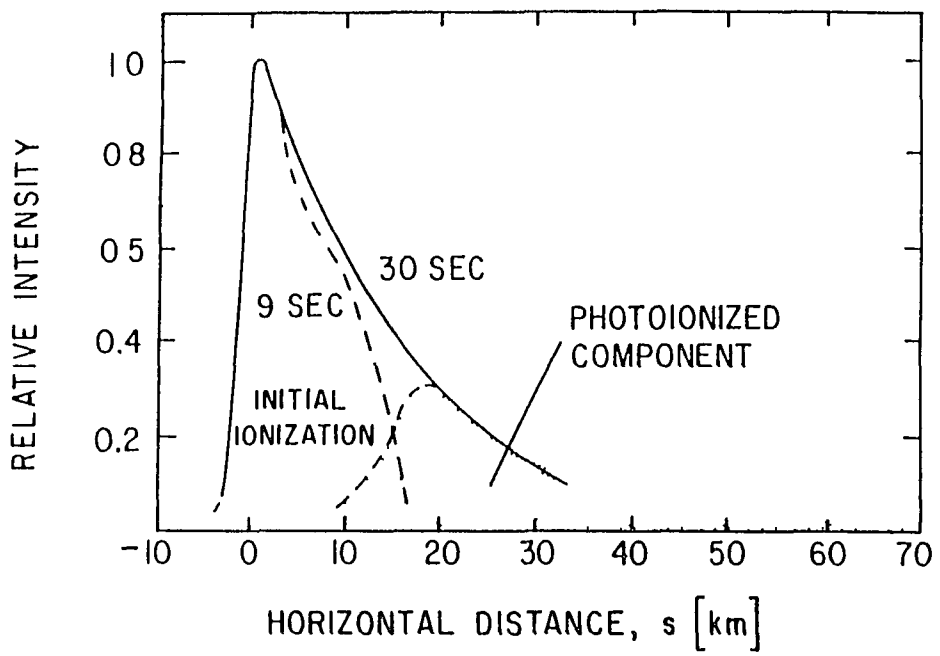

Figure 1.6: Densitometer traces of the ionized barium cloud appearing above the terminator. The dotted part is a fit of the data to the expected contribution from photo-ionization. Nearly all ions to the left of $s = 15$ km are the result of an initial ionization in darkness (from Haerendel, 1982).

for Chachalaca except for a larger beam angle (28°) with respect to B_0. Since the explosion was far below the solar UV terminator, two separate ionizing barium clouds were detected after they entered into sunlight as illustrated in figure 1.5 [Haerendel, 1982a]. As explained by Haerendel, the western edge of the ion cloud appeared to be confined within 15 km of the field line where the explosion occurred. These ions were created near the explosion point. The eastern wing of the cloud which had a more diffusive profile should be the remaining neutral atoms photo-ionizing after reaching the terminator. Figure 1.6 shows densitometer traces of the ionized barium cloud appearing above the terminator.

After 9 seconds from the explosion, the initial cloud ions were estimated corresponding to about 28% of atoms with perpendicular velocity greater than the critical velocity. The thermal ionization in the explosion phase was estimated no more than 0.1%. Haerendel suggested that no explanation other than a beam plasma discharge appears to be possible. The relatively fast cut-off of the initial ionization at a transverse range of about 15 *km* was interpreted as the result of the neutral density falling below the lower threshold for the critical velocity effect. However, there was no *in situ* measurement made inside the barium cloud, which made the identification of ionization process impossible.

1.2.3 Bubble Machine

Bubble Machine [Deehr et al., 1982] was the second in a series of rocket flights, the first was called KING CRAB [Wescott et al., 1980], utilizing the radial shaped-charge technique on the upper atmosphere to trace the configuration of the Earth's magnetic field, to determine the electric field profile, and to study the auroral physics. To provide another capability for the investigation of the CIV hypothesis, the shaped-charge liner was doped with 1% of Sr, and the release took place above barium's UV shadow such that the barium could be photoionized but under strontium's UV terminator. Thus, any ionization of strontium should be considered to be due to another ionization process. The shaped-charge was radially injected in a plane perpendicular to the local geomagnetic field with velocity up to 14 km/s. Results from the photometer showed that 15%-50% of the strontium was ionized [Deehr et al., 1982]. A small fraction of fast ionization of barium atoms was also observed and was ascribed to CIV.

However, the interpretation of this result has never been self-consistent, as

pointed out by Stenbaek-Nielsen [1982]. Firstly, only a small fraction of barium was ionized and it might be attributed to photoionization. Secondly, if CIV was operating, one would expect that the ionization ratio of the two atoms would be proportional to the mixing ratio in the explosive liner because the two atoms have similar electron impact ionization rates. However this is not what was observed.

1.2.4 Star of Condor

In light of the high yields from the Bubble Machine, the Star of Condor [Wescott *et al.*, 1986] was another critical velocity experiment using radial strontium injection into the upper ionosphere. The Sr charge liner detonated radially into a plane parallel to the geomagnetic field such that a full pitch angle distribution of strontium was obtained. About 42.5% of strontium had velocity exceeding its critical velocity (3.3 km/s). However, no Sr ion emissions were detected shortly after the burst with usual TV integration times. The total ionization of the Sr was only 0.00036% [Wescott et al., 1986b]. The fraction of the thermal ionization for the conical barium shaped charges ranged from $10^{-3} - 10^{-4}$ [Haerendel, 1982a]. If 15% of the Sr was vaporized and 0.1% was ionized by the high-temperature Maxwellian tail in the explosion process, then 1% ions would have been produced initially. Thus the Alfvén CIV mechanism proposed for space plasmas did not produce an ionization cascade in this experiment.

1.2.5 Star of Lima

Star of Lima is similar to Star of Condor except that a high explosive conical barium shaped-charge was used on Star of Lima and it consisted mother-daughter payload instrumented with a diagnostic payload to perform an *in situ* measurement in the

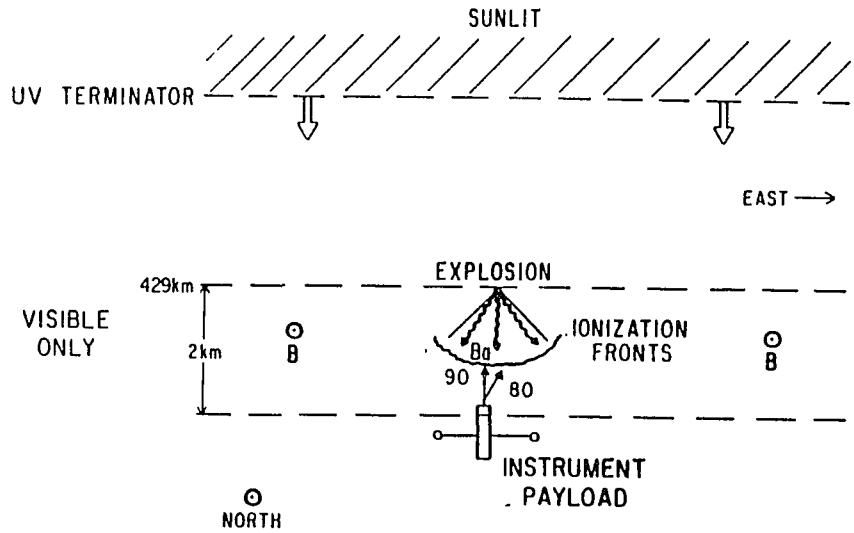

Figure 1.7: Critical velocity experiment over Chilca, Peru (from Torbert and Newell, 1986).

neutral beam for the first time. The geometry of the experiment is shown in figure 1.7 [Torbert and Newell, 1986]. The conical charge had a full opening angle of 30° and it directed the barium beam almost directly across magnetic lines toward the instrumented payload. The rocket, however, flew too high such that the barium was partially exposed on sunlight. Although this should have provided an excellent seed ionization to ignite the CIV interaction, the net yield was very low. The optical observations conducted from ground [Wescott et al., 1986a] indicated that about 0.13% - 0.25% of barium was ionized. The particle detector measured a fractional yield of about 5×10^{-4} [Torbert and Newell, 1986].

In spite of this negative result, the electric field measurements [Kelley *et al.*, 1986] and the particle measurements [Torbert and Newell, 1986] performed inside the stream showed many phenomena associated with the critical velocity effect such

as: superthermal electron tail accompanied by intense waves near the ambient oxygen lower hybrid frequency, energy loss in the ion energy spectrum. It seems that the electrons were energized at the expense of ion kinetic energy through a collective process. Although the Alfvén CIV mechanism may not have been very efficient in the present geometry, some of the essential features of the CIV mechanism were identified.

1.2.6 SR90

SR90 [Wescott et al., 1990] was one of two sounding rocket experiments carried out in 1986 attempting to understand the apparent failure of the Alfvén mechanism to produce a cascade or ionization in Star of Condor and Star of Lima. SR90 was the first space CIV experiment used a conical strontium shaped-charge. The conical shaped-charge was expected to created higher neutral density and slower density decay than the radial shaped-charge used in Star of Condor. SR90 was carried out in full solar UV and there was no *in situ* diagnostic. The ambient plasma density was $1.5 \times 10^4\ cm^{-3}$, similar to that in Peru. The optical results showed that less than 0.18% of the vaporized Sr were probably ionized by CIV mechanism. It was suspected that this low yield result could be due to the low ambient plasma density. Note that the plasma density was $6 \times 10^5\ cm^{-3}$ in the high yield of Porcupine experiment.

In spite of the negative result, SR90 gave the best neutral velocity distribution for an alkali-metal shaped-charge release. The differential velocity was shown in figure 1.8.

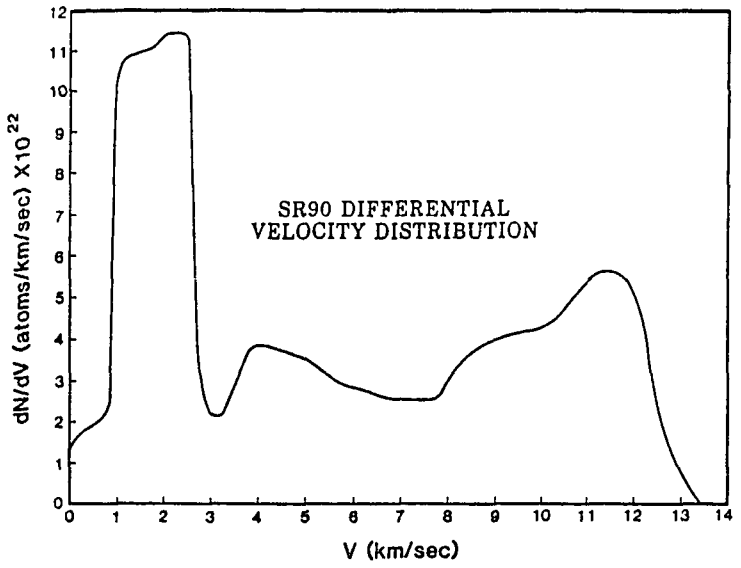

Figure 1.8: Differential strontium neutral velocity function. The scale is derived from the assumption that 15% of the liner is vaporized (from Wescott *et al.*, 1990).

1.2.7 CRIT-I

Unlike SR90, CRIT-I payload was in a mother-daughter configuration instrumented with a full diagnostic payload to perform *in situ* measurement inside and outside of the neutral beam. The geometry was similar to Chachalaca and Porcupine with the expectation that ions would be created near the release by a relatively short lived critical velocity process to form a field aligned jet along the release field line. There were two separate conical barium shaped-charge releases at 1.99 km/s and 4.34 km/s from the diagnostic payloads. The beam has $\sim 14°$ full open angle and was made a 46° from the magnetic field (see figure 1.9). According to ground based observations of the ions which came up into sunlight $5 - 10$ s after the burst, the ionization yield in CRIT-I was extended over 40 km and comparable to the low ionization in Star of Lima. The rate of ion production could be matched by an ionization rate (per

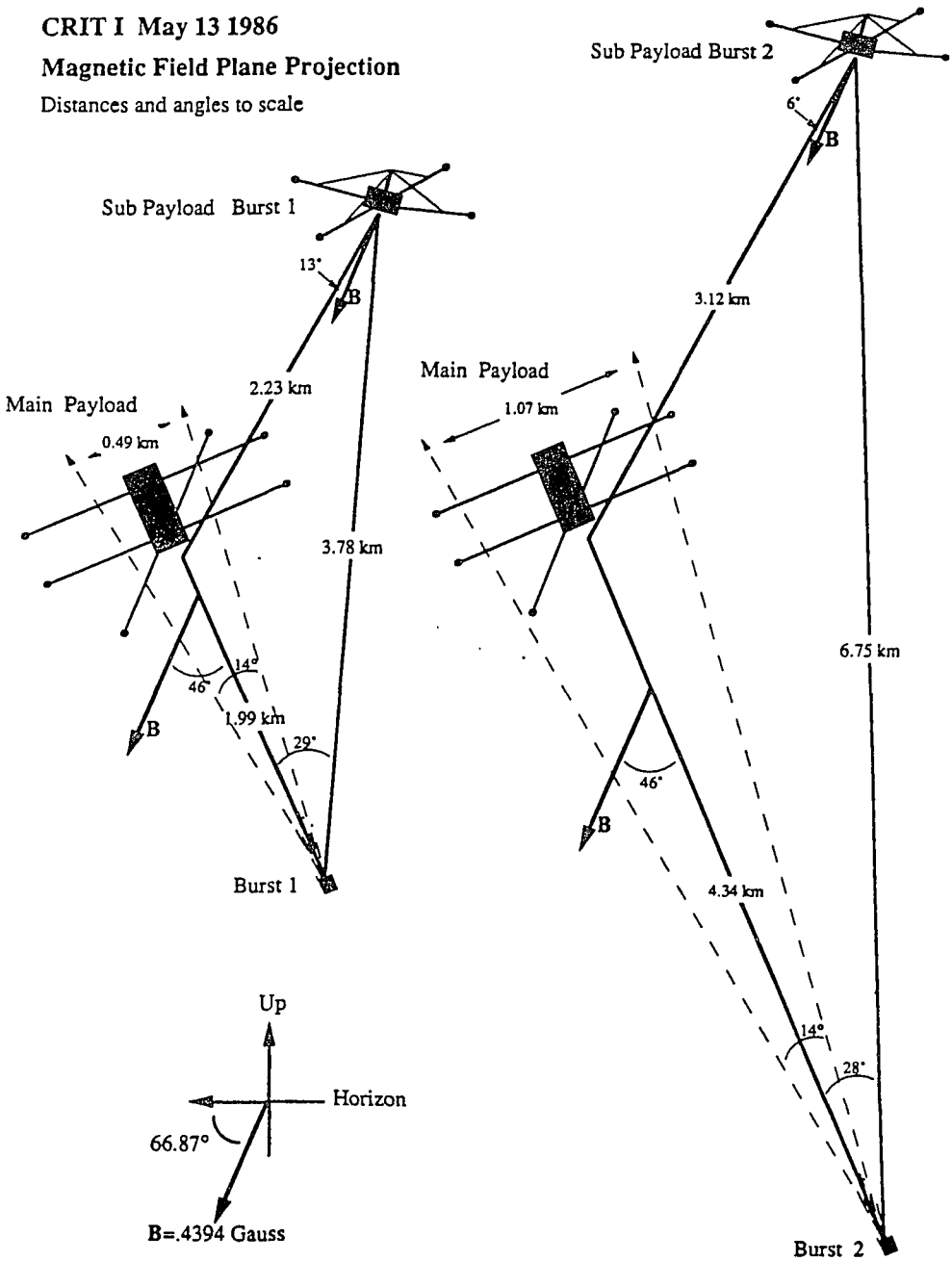

Figure 1.9: The release geometry projected on the plane of the magnetic field and the barium stream direction (from Kelley *et al.*, 1991).

barium atom) within the beam of $1/1800\ s^{-1}$, independent of the distance from the explosion [Stenbaek-Nielsen et al., 1990a]. The probable source of this ionization is due to charge exchanges with ambient ions and collisions with ambient neutrals (charge stripping). Since the observed image is almost exclusively due to ions with initial neutral velocities above the threshold of 8.4 km/s (5.21 eV in the center of mass frame) for collisional ionization, they concluded that the charge stripping could be the major source of the barium ion inventories. By using a computer simulation, they gave this charge stripping cross section of order $10^{-17}\ cm^2$ to match the observations.

Although the critical ionization velocity effect did not go into a charge cascade phase, remarkable electromagnetic effects were seen in the neutral beam-plasma interaction. A very large quasi-dc electric field was detected antiparallel to the beam velocity as well as a comparable large quasi-dc electric field ($\sim$ 500 mV/m) along the magnetic field. The fluctuating electric fields were also quite large, in fact, of the same order of magnitude as the quasi-dc pulse. The wave energy was found to maximize at frequencies below the barium lower hybrid frequency and included strong signatures of the oxygen cyclotron oscillation. Brenning *et al.* [1991a] argued that there could have been a higher ionization rate close to the explosion point, which escaped detection in the optical observation because the ions were scattered in the strong electric field. Unfortunately, the on board particle detector failed due to software errors.

1.2.8 CRIT-II

CRIT-II was a payload almost identical to CRIT-I, and was flown with the same purpose in mind. The major difference between these two experiments is that the

plasma density was higher in CRIT-II than in CRIT-I, thus it was expected that the ionization yield will be higher in CRIT-II than in CRIT-I. A convincing result of 4% ionization yield has been reported by Stenbaek-Nielsen [1990]. Although the ionization yield was not as high as that in Porcupine and the detail of ionization mechanism has yet to be justified, it is believed that a high plasma density is a necessary condition for high ionization yield. The success of the *in situ* measurements from both field and particle detectors provided a great chance to understand the space CIV mechanism. A complete explanation of CRIT-II experiments will be given in the next two chapters.

1.2.9 CRRES-CIV

There were four critical ionization velocity tests carried out by NASA orbiting spacecraft CRRES chemical release program [Wescott et al., 1993] in September, 1990. Two bariums and one strontium and one calcium were thermite released. The relative velocity of the gas cloud and the ambient plasma is given by the orbital velocity of 9.4 km/s, a value much greater than the critical velocities of three atoms (2.7 km/s for Ba, 3.5 km/s for Sr, and 5.4 km/s for Ca). Compared to a shaped-charge injection cloud, an orbiting release cloud has a small expansion velocity, therefore it can produce a continuous high density neutral beam cloud, can last longer in space, and perhaps, consequently, can produce more ionization. In light of the high ionization yield from Porcupine and CRIT-II, four releases were conducted at dusk to achieve a high plasma density background, and well below the solar UV terminator, therefore any ions created in the darkness can be observed as soon as they travel up into the sunlight. All four releases had the same angle between beam and B, close to 78°. Only optical measurements, at a remote distance, were available. Its

result, reported by Wescott *et al.*, indicated that all four experiments have not been able to reproduce high ionization yields as was expected (see Table 1.3). However the quick loss of ion energy was observed. After examining all the possible ion energy loss mechanisms, they conclude that the $Ba^+ - O$ charge exchange can only explain half of the ionization while the other half could be due to inelastic ion-ion coulomb collisions. They also suggested that probably a small unknown number of ions, produced by a non-solar UV process, probably lost so much energy that they were unable to travel up along the field lines to be observed.

1.3 Review of Current CIV Theories

The Alfven's CIV hypothesis involves energy conversion from the kinetic energy of beam ions to the ionization energy of neutral atoms. The definition of critical velocity by equation (1.1) indicates that the energy transfer needs to be 100% efficient. Thus, the identification of this process has been the fundamental problem which experimental and theoretical scientists have been working on for decades. However, a theoretical model which can explain all the CIV experiments is yet to be established. The current CIV theories can be categorized into macroscopic and microscopic points of view. The macroscopic theory concerns the basic physics: conservation law such as energy and momentum, while the microscopic theory deals with the detailed dynamic process of energy conversion and ionization mechanisms.

1.3.1 Microscopic Theories

In Alfvén's original thoughts, the CIV effect was expected to occur in a plasma in which the ion-neutral collision is negligible. This is because only the kinetic energy in the center of mass frame can be converted to another form of energy in an inelastic

collision. Accordingly, one can prove that at least twice the energy given by equation (1.1) will be needed in order to make an ionization collision for two particles of equal mass. On the other hand, a single electron has a much higher ionization frequency than an ion of equal energy. Therefore, heating of electrons is a key ingredient to ignite an efficient CIV effect. Now the question is how can the free energy, in its relative motion between a neutral gas and a plasma, be effectively transferred to electrons?

It was first suggested by Sherman [1972] that the lower hybrid instability (LHI) could be the most promising one for electron heating in the CIV effect. Several laboratory experiments have also shown that the electron heating is associated with collective wave-particle interaction [Raadu, 1978; Möbius et al., 1979; Piel et al., 1980]. To excite this instability, it is necessary to assume that the neutral gas contains seed ions, which could be produced by non-CIV mechanism such as charge exchange ionization. As they pass across the plasma, electrons will be captured by the magnetic field immediately but ions due to their relatively large gyroradius can keep moving forward and excite electrostatic waves in the lower hybrid frequency range (in a low beta plasma) whose electric field is predominantly perpendicular to the ambient magnetic field, a small but important component of the unstable wave vector k_z and its associated electric field lies along the magnetic field. This parallel component of the wave field is responsible for heating the electrons to high energies. This process will continue until the electrons gain enough energy to ionize gas atoms upon collisions.

The theoretical and numerical simulation studies have indicated that the lower hybrid mode may be very efficient in transferring ion kinetic energies to electrons.

The first computer simulation done by McBride [1972] found that at the final stage of LHI anomalous heating, about 50% of initial kinetic energy of streaming ions was transferred to the thermal energy of plasma and partitioned almost equally to the electrons (parallel to B_0) and ions (perpendicular to B_0). Similar results were also given by later simulations [Tanaka and Papadpoulos, 1983; Machida and Goertz, 1986]. According to the quasi-linear theory, the electrons are heated preferentially in the high energy range so that a hot electron tail distribution is formed. Undoubtedly, this is a more efficient way for energy transfer than bulk heating. The efficiency of ion beam to electron energy transfer has also been theoretically calculated by Formisano *et al.* [1982]. When the ionization rate is greater than the ion gyrofrequency, *i.e.* $\nu_{ion}/\Omega_i > 1$, the ion beam can be considered as an unmagnetized beam with straight trajectory, they gave $\eta_e = 2/3$, where η_e is the fraction of ion beam energy available for electron heating. If the ionization rate is small such that $\nu_{ion}/\Omega_i < \sqrt{m_e/m_a}$, the ion distribution will be a ring type, then η_e becomes 0.025.

It is very important to know that the above results can only be applied for a low β plasma and a sub-Alfvénic beam as pointed out by McBride *et al.* [1972]. Otherwise the instability will be stabilized by electromagnetic effects. In general, the value of β is very small in the laboratory and the ionospheric plasmas but it could be large in the solar wind plasma.

1.3.2 Macroscopic Theories

Energy Balance

Alfvén's CIV effect is a self-sustaining discharge process. To maintain this process, the kinetic energy of a moving cloud must exceed the ionization potential energy. If only a fraction η_e of free energy is available for electron heating, the energy balance equation for electrons is given by [Haerendel, 1982a]

$$\dot{n}_i \tau_{inj} \left(\eta_e \frac{Mv^2}{2} - e\phi_{ion} \right) = T_h n_h + T_c n_c + L \tag{1.2}$$

where T_h and T_c are the energy of hot and cold electron, they are separated by the ionization energy $e\phi_{ion}$, n_h and n_c are their corresponding density, L is the energy loss term, τ_{inj} is the passage time of a given plasma element over the gas cloud, and the ionization rate, $\dot{n}_i$, is defined by

$$\dot{n}_i = n_n n_h < \sigma_{ion} v_h > \tag{1.3}$$

Since equation (1.3) depends on n_n and η_e, for a given η_e the lower limit on the neutral density can be given. After further analysis, Haerendel [1982a] reaches at the Townsend condition [Danielsson and Brenning, 1975] which states that in order to have a steady discharge process a hot electron has to make at least one ionizing collision during the time of contact with the neutral beam. Also, he found that the fraction of ion beam energy transferred to the hot electrons must be greater than 0.5 ($\eta_e > 0.5$) to achieve the high ionization yield as observed by Porcupine. This is not impossible, since theoretically η_e can be as high as 2/3. However, any non-CIV ionization mechanism such as charge exchange, charge stripping, etc. which can supply more available energy should also be considered. Then the equation (1.3)

should be replaced by

$$\dot{n}_i = n_n(\nu_{ion} + \nu_{exc} + \nu_{stp} + etc.) \tag{1.4}$$

The condition for η_e in equation (1.2) is therefore somewhat relaxed. Also, from equation 1.2, one can obtain a threshold velocity of the neutral cloud for a positive energy feedback condition.

$$v_{thr} = \eta_e^{-1/2}\sqrt{\frac{2e\phi_{ion}}{M}} \tag{1.5}$$

where the possible value of η_e is given by microscopic theory.

By considering energy balance, a possible CIV feedback loop can be illustrated as in figure 1.10.

Despite the fact that theoretical studies have suggested that the lower hybrid instabilities could be the promising candidate for electron heating in the CIV effect, the collective wave-particle interaction in the CIV experiment does not have to be associated with the LHI because there is no strong experimental evidence to support this theory. Since the efficiency of energy transfer is crucially dependent upon the type of collective wave-particle interaction, the efficiency of a specific collective process is dependent on the physical situation. To expect an efficient CIV process, an efficient energy transferring process is necessary.

Momentum Balance

In the critical velocity process described above, the energy of ion beam needs to be transferred to much lighter electrons. Since electrons can not efficiently carry the momentum which corresponds to the amount of energies being transferred to electrons from heavy ions, in order to conserve the momentum, the background plasma has to take up the momentum which is lost from the beam cloud. By any

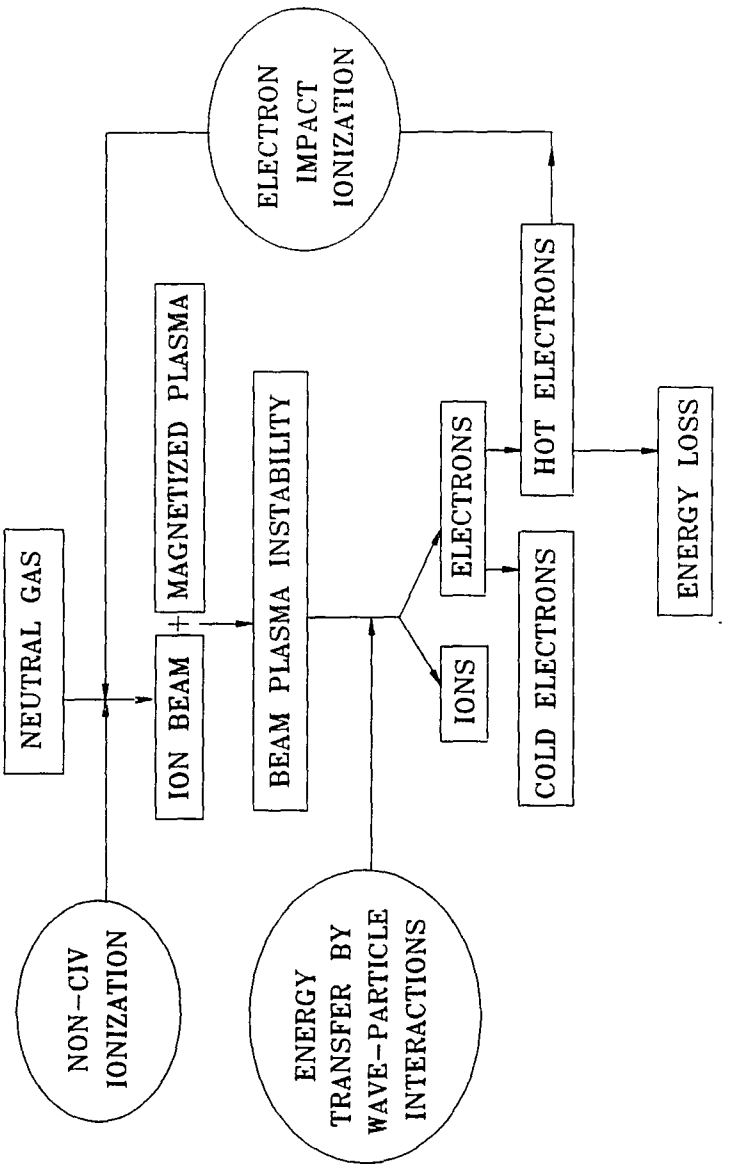

Figure 1.10: A possible CIV feedback loop.

means, if this momentum transfer does not effectively proceed, the energy transfer will be quenched, and consequently the CIV effect will be prohibited.

Momentum coupling between a neutralized plasma beam and an ionospheric plasma has first been analyzed by Scholer [1970]. Haerendel [1982a] used a more intuitive way by analogy of collision between two particles to achieve a similar conclusion: the momentum exchange between the beam cloud and the ambient plasma is through emission of Alfvén waves along the magnetic field line from the interaction region to the ambient plasma. To effectively transfer the momentum from the beam cloud to the ambient plasma, the mass of the beam cloud in the interaction volume must be equal to the mass of plasma covered by Alfvén waves. This mass ratio, λ_M, is called the mass loading factor [Haerendel, 1982a; Torbert, 1987] and is given by

$$\lambda_M = \frac{M_n \dot{n}_i L_{\|}}{4\rho_a v_A} \tag{1.6}$$

where $\dot{n}_i$ is the ionization rate per unit volume, $L_{\|}$ is the length scale of the interaction cloud along the magnetic field, and ρ_a is the mass density of the ambient plasma. One can realize that $\lambda_M = 1$ means two volumes of equal mass colliding with each other. The physical significance of this mass loading effect can be understood by the polarization electric field induced by the injection of ions into a magnetized plasma. This polarization electric field is given by

$$\mathbf{E}_p = -\frac{\lambda_M}{1+\lambda_M}\mathbf{v}_b \times \mathbf{B} \tag{1.7}$$

and is created in a direction such that the ambient plasma will be accelerated to reduce the relative velocity between the neutral beam and ambient plasma [Torbert, 1987]. If this relative velocity is reduced below the critical velocity, the CIV effect will stop.

Table 1.3: Parameter regimes of critical velocity situations.

Laboratory Experiments				
	B(Gauss)	$N_n(cm^3)$	$N_p(cm^{-3})$	ω_e/Ω_e
Rotating plasmas	$100 - 10^4$	$10^{13} - 10^{16}$	$10^{12} - 10^{15}$	$0.3 - 10^3$
Coaxial plasma gun	$100\text{-}2.5 \times 10^3$	$10^{14} - 3 \times 10^{16}$	$10^{12} - 10^{15}$	$0.1 - 10^3$
Impact experiments	$150\text{-}4.4 \times 10^3$	$2 \times 10^{11} - 10^{14}$	$10^{11} - 10^{13}$	0.1-100
Astrophysics				
Io	0.01	$10^{10} - 10^{12}$	10^4	30
Comets	5×10^{-5}	$10^4 - 10^6$	$10^2 - 10^3$	600-2000
Solar wind	5×10^{-5}	1-10	1-10	60-200
Space Experiments				
Barium jets	0.3	$3 \times 10^5 - 10^9$	$10^3 - 6 \times 10^5$	0.3-3
Ionospheric clouds	0.3	$10^5 - 10^9$	$10^3 - 10^5$	0.3-3
M/S clouds	$1 - 4 \times 10^{-4}$	$10^6 - 10^9$	$10 - 10^3$	25-1000
Solar wind clouds	5×10^{-4}	$10^6 - 10^9$	$10 - 10^3$	200-2000

1.4 Application of CIV Concept

In spite of the lack of solid foundation for the CIV theory, the concept of a critical ionization velocity effect has been applied to the explanation of many phenomena in space such as the rapid ionization within cometary comae [Haerendel, 1986; Galeev et al., 1986], the strong interaction of Io with the Jovian magnetosphere [Cloutier et al., 1978; Galeev and Chabibrachmanov, 1983], an additional ionization mechanism for the interstellar gas which penetrates the heliosphere [Petelski, 1978; Petelski et al., 1980], and shuttle glow [Papadopoulos, 1984]. These applications, in other words, somehow provide evidence of the existence of CIV in space plasmas in various parameter regimes. Reviews concerning the application of the CIV concept in space have been given by [Petelski, 1981] and Newell [1985]. The importance of the CIV concept in astrophysics was also discussed by Petelski [1981] in many possible areas such as stellar bubbles and planetary nebulae, the deceleration

of supernova remnants by interstellar matter, the expansion of H II regions into molecular clouds, and the physics of radio galaxies. In this section, we will briefly review several applications of the CIV effect in space.

1.4.1 Space Vehicle Glow

Since the first report by Heppner and Meredith [1958], optical contamination in the wakes of spacecraft has drawn much attention due to the fact that it is very important to more and more space experiments associated with low light level optical detectors.

The basic features from the early investigations indicated that strong visible light emissions from the wakes of rockets were observed [Wallis and Anger, 1968]. Stegman *et al.* [1982] and Lopez-Moreno *et al.* [1982] also reported that bright emissions in both the ram and wake directions, particularly in the visible light spectrum, were observed.

More recently, following the third flight of the space shuttle in March, 1982, the presence of a diffuse optical emission surrounding surfaces of the vehicle exposed to the atmosphere in the ram direction was reported by a series papers [Banks et al., 1983; Mende et al., 1983]. A similar glow was also observed on the Atmospheric Explorer satellites [Torr, 1983]. This vehicle surface glow was usually attributed to pure chemical effects, namely, the interaction between atmospheric oxygen with the surface of the vehicle body [Yee and Abreu, 1983; Slanger, 1983]. Papadopoulos [1984] , on the other hand, suggested an alternative for the shuttle glow. The shuttle has orbital velocity near 8 km/s, below the oxygen's critical ionization velocity (12.7 km/s). He conjectured that a small fraction (2-3%) of ramming plasma being reflected in the tail region can form a counter-streaming ion beam with the ambient plasma in the shuttle rest frame, but in plasma frame, this

reflected plasma has a velocity of 16 km/s which exceeds the critical velocity of oxygen. He concluded that the shuttle glow is due to the anomalous ionizing CIV effect by collision of hot electrons which were energized by beam plasma instabilities.

1.4.2 Io Plasma Torus

One of the most surprising findings by the Pioneer 10 is that the satellite Io, the innermost Galilean satellite of Jupiter, possesses an ionosphere [Kliore et al., 1974]. Since Io is constantly being overtaken by Jupiter's corotating magnetosphere, as first suggested by Cloutier *et al.* , the corotating Jovian magnetospheric plasma with a speed of 57 km/s relative to Io's atmosphere, suffices for any gas to be ionized by Alfvén's critical ionization velocity effect. He constructed a model which partially incorporates the CIV theory to simulate the electron density-altitude profile on Io's ionosphere reported by Kliore *et al.* . He came to a conclusion that the critical ionization velocity effect is important at the initial stage.

Later observations made by Voyager 1 and 2 indicated that the Io is the source of particles in the Jovian magnetosphere and a dense plasma torus enveloping Io's orbit [Brown, 1974; Bridge et al., 1979; Bagenal and Sullivan, 1981]. The charge exchange ionization of neutral particles sputtered from the Io surface with the corotating magnetospheric plasma of Jupiter has been identified as the main ion source of the torus [Pontius and Hill, 1982]. Once a neutral atom is ionized, it carries the same energy as its mother atom. However direct measurements indicated that the characteristic temperature of the plasma torus is about 40 eV which is much smaller than a sulfur ion's pick-up energy of 540 eV. Galeev and Chabibrachmanov proposed that this cooling process could be accomplished by the critical ionization velocity effect. They employed the same quasilinear theory formulated by Formisano *et al.*

to calculate the electron heating by lower hybrid instabilities with an assumption that the energy which the ion beam loses goes to the high energy tail population of electrons. They came up with results which were fairly consistent with the observations and they also suggested that the ultraviolet emission of the plasma torus is a consequence of the collision of superthermal electrons with atoms or ions.

More recently, in a similar situation of an oxygen torus in Saturn's ring system Morfill *et al.* suggested that the superthermal electrons observed by Sittler *et al.* could be due to the critical ionization velocity effect. However, an inefficient CIV process is required in order to explain the low ion density reported by Broadfoot *et al.* [1981].

1.4.3 Cometary Neutral Gas Ionization

Rapid ionization of the cometary neutrals has been an interesting feature of the interaction of the solar wind plasma with the neutral atmosphere of comets. According to the observations, neither the well known photoionization nor the charge exchange with solar wind protons can explain this anomalous collisionless ionization. Both these processes take place typically with time scales of the order of 10^6 s at a heliocentric distance of 1 AU. Wurm [1943] suggested that an unknown internal ionization source which is capable of ionizing the cometary neutrals with a short time scale in the order of 10^4 s is therefore needed. Axford [1964] and Beard [1966] proposed that if the solar wind electrons can be energized to keV range by the passage of upstream outgoing shock, the time scale for ionization can reach 10^5 s, still falling short by an order of magnitude. However, it was pointed out by Wallis [1972] that the electron heating by a common cometary bow shock can only achieve 10 eV rather than keV. Besides the dissociative ionization, a search for an effective mecha-

nism for electron energization has been undertaken since then. The first attempt to simulate the CIV interaction in the cometary coma by laboratory experiment was made by Danielsson and Kasai [1968] and later in a similar experiment by Podgorny and Andrijanov [1970]. These experiments support the CIV effect, but without explaining the role of any instability or magnetic field strength. The latest comet experiment was conducted by Chang *et al.* [1989] who found that a plasma cloud surrounding the comet is visible only when the solar wind velocity and IMF are both above certain minimum values. This lower limit of magnetic field is consistent with the CIV experimental results by Brenning [1981] .

The theory of anomalous ionization of cometary atmospheres associated with CIV was developed much later by Formisano *et al.* [1982] who suggested that the relative velocity between the solar wind and neutral gas sublimated from the nucleus of the comet can excite electrostatic lower hybrid instabilities which then transfer the kinetic energy of the solar wind to electrons. They used quasi-linear theory to investigate the efficiency of the energy transfer, η_e, and found out it ranges from 0.025 to 0.67 depending upon the ratio of the ionization rate to the ion gyrofrequency. Since η_e is less than unity, Formisano *et al.* proposed a threshold velocity for CIV effect given by

$$v_{th} = \eta_e^{-1/2} v_c \tag{1.8}$$

They also show that the Townsend criterion requires that $r < 1000\ km$ for a comet such as Halley at 1 AU. However, Mendis *et al.* [1985] questioned whether the solar wind could penetrate so close to the cometary nucleus. This remains an open question.

1.5 Thesis Overview

This dissertation will be organized as follows. The CRIT-II experiment will be first reviewed in chapter 2 and its results will will be presented in Chapter 3. In Chapter 4 we will focus on the issue of the barium ionization mechanism by electron impact ionization and charge exchange. A particle simulation based on the Liouville theory will be developed to calculate the ion density measured by the CRIT-II main payload. In Chapter 5 an elastic scattering model will be developed to explain the early observed ions. The early stage of electron heating will be investigated in Chapter 6. We will examine the effect of a finite width inhomogeneous beam on the lower hybrid instabilities in Chapter 7. In chapter 8 the momentum coupling between an ionizing barium cloud and ionospheric plasma will be studied. In the last chapter, we will summarize the whole research work and make a conclusion. A suggestion will be also given for possible future space CIV experiments.

CHAPTER 2

CRIT-II Experiment

A Black Brant X sounding rocket, numbered 35.019 (CRIT-II), was launched from Wallops Island, Virginia, at dusk on May 4, 1989, to investigate Alfvén's critical ionization velocity effect in the ionosphere. CRIT-II is the sequel to the CRIT-I experiment. Having in mind the high ionization yield of Porcupine, CRIT-II was carried out at local dusk to achieve high ambient plasma density instead of low density in CRIT-I.

The method employed in the CRIT series experiments to test Alfvén's critical ionization velocity effect is to utilize a shaped-charge barium release into the ionosphere. A neutral beam created by detonation has typical velocities perpendicular to the ambient magnetic field, B_0, much greater than the critical ionization velocity of barium atoms. The neutral barium beam was expected to have interactions with the ambient plasma. A well instrumented rocket payload was waiting on the path of neutral beam to perform *in situ* measurements.

In this chapter, we will describe the CRIT-II experiments, including its on board instrumentation and the experimental configuration. However, the particle detectors provided by UNH will be emphasized. A brief discussion of the geometrical factor of the detectors will be given and lastly, a numerical simulation of one of the detectors

will be fully described.

2.1 Experimental Configurations

CRIT-II was a two section mother-daughter type sounding rocket. The mother, or main, was designed to diagnose the beam-plasma interactions inside a streaming neutral beam, and the daughter was deployed on the same geomagnetic field line as the mother, but outside the beam to monitor charged particles and waves mapped out from the location of the mother payload along the field line. In this experiment, two identical shaped-charge canisters, provided by the University of Alaska, were released to perform the same experiment at two sides of apogee. Both conical shape barium beams had $\sim$ 15° of full angle and pointed oblique to the geomagnetic field about 45°. The major difference between the two releases is the separation distance of the release point from the main payload (1.585 *km* for the first release and 3.881 *km* for the second release). To avoid illuminating the neutral barium by sun light, both releases were conducted at local dusk at 410 *km* altitude, about 100 *km* below the barium solar UV terminator. Once the neutrals are ionized, barium ions will follow the magnetic field line up and be exposed to the sunlight where they can be observed with a camera. An approximate release configuration of the CRIT-II experiment is shown in figure 2.1.

2.2 Payload Instrumentation

2.2.1 Main Payload

CRIT-II was instrumented to measure AC and DC electric fields, background magnetic field, plasma density, and nonthermal electrons and ions. The electric and mag-

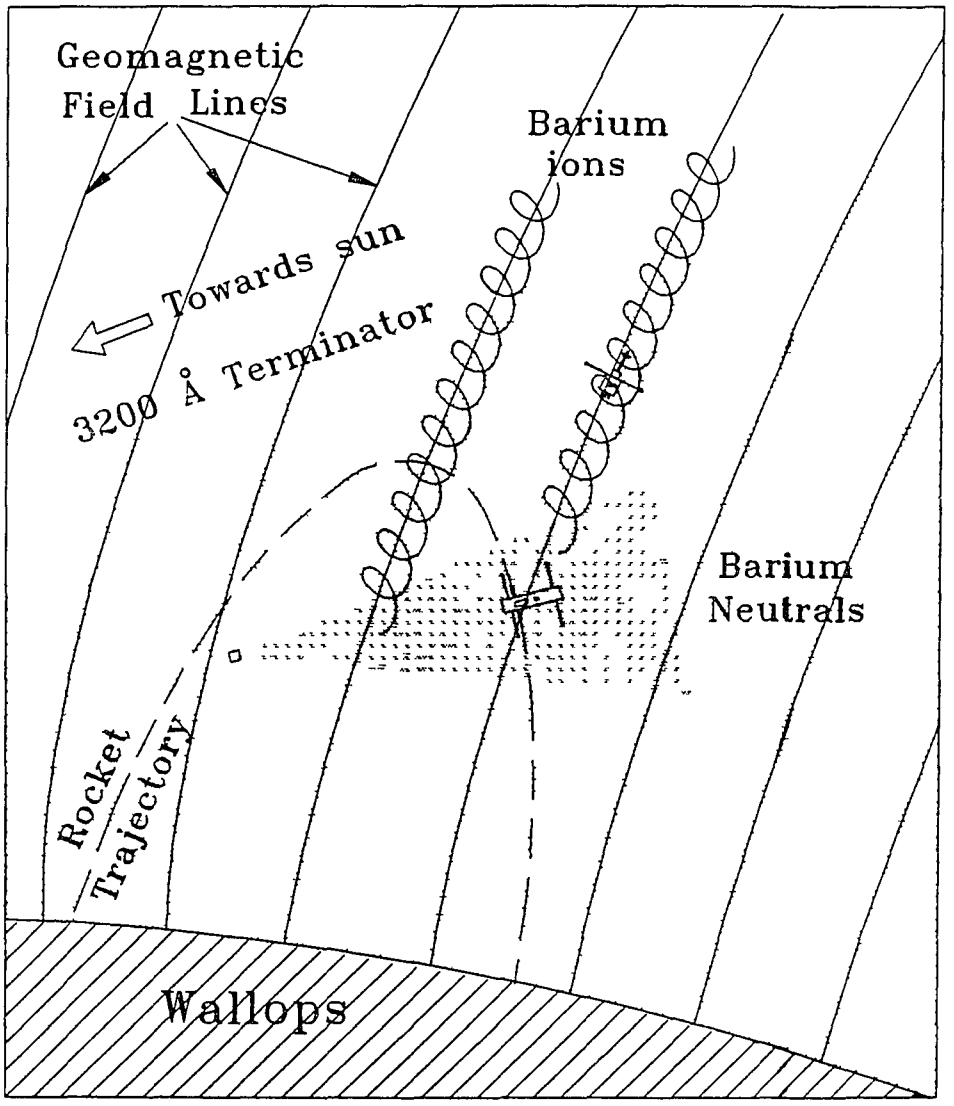

Figure 2.1: A cartoon of release configuration of the CRIT-II experiment.

netic fields measurement packages were provided by Cornell University. The electric field measurements were made via the standard double probe technique whereby the potential difference between spherical probes is determined [Swenson, 1992]. There are three sets of electric field probes which enable three dimensional electric field measurements. A well calibrated magnetometer was used to measure three components of perturbations of the geomagnetic field caused by the beam-plasma interactions. Plasma density measurements were made by the Plasma Frequency Probe (PFP), provided by Utah State University. This instrument excites the probe, or dipole antenna, with a variable low-level frequency that sweeps around the upper hybrid frequency from which the plasma density can be determined, provided the magnetic field is measured simultaneously.

On CRIT-II, UNH provided two solid-state photometers. The "green" photometer had an optical window centered at 5500 Å and band width 100 Å to look at the barium 5535 Å resonance line. The "red" photometer had an optical window centered at 6330 Å and band width 100 Å to exclusively measure the oxygen 6300 Å excitation line. Both photometers, had 13° of view angle, were installed on the payload aft surface and deployed to look on to the chemical canister release point. The main purpose of the photometers is to determine the actual barium release time and to measure the population of nonthermal electrons.

UNH also provided two electrostatic analyzers (ESA) of the Berkeley 'top-hat' design [Carlson et al., 1983] and one collimated potential analyzer (CPA) to measure the nonthermal part of charged particles: one ESA for ions, one ESA and one CPA for electrons. The ESA detector consists of three concentric spherical plates to provide 360° of angular resolution of measurement. Figure 2.2 shows a cross-sectional view

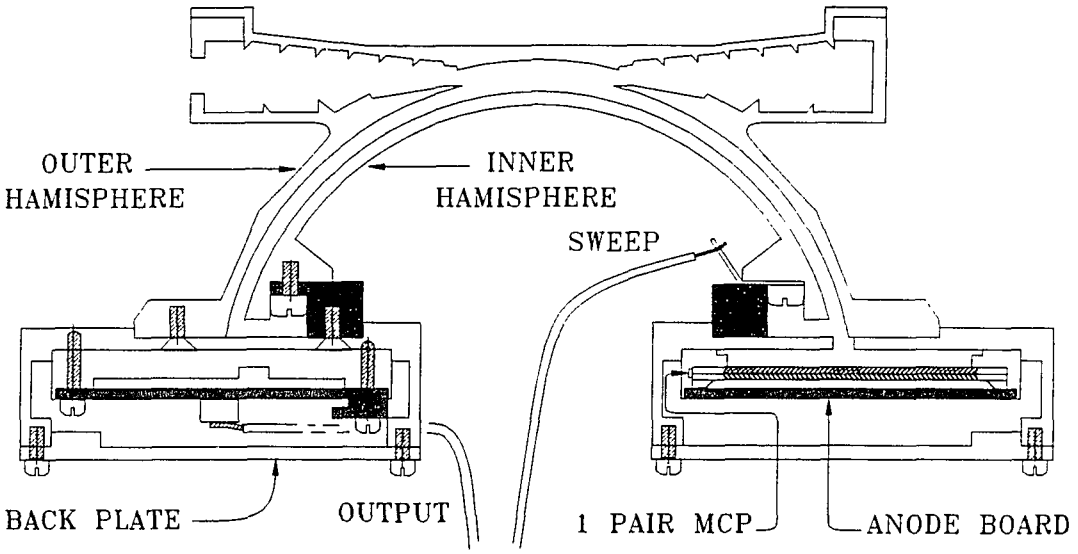

Figure 2.2: A cross-sectional view of ESA detector.

of the ESA detector layout.

The top-hat plate and a hole underneath it in the outer hemispherical plate constitutes a 360° entrance aperture for the particle. A charged particle entering between these two plates which are held at ground will be deflected by the inner hemispherical plate which is charged at voltage V (positive for electrons and negative for ions) into the gap between the inner and the outer plates. Only particles with proper E/Q (energy to charge ratio) will go through the gap and strike on the sensor to make counts. The separation between the hemispheres determines the energy bandpass, $\Delta E/E$. On this flight, the energy bandpass was 0.06 for electrons and 0.15 for ions. Once the particles leave the exit aperture, they strike a pair of chevron configured micro-channel plates (MCP) which provide a saturated gain of $\sim 2 \times 10^6$ with a narrow pulse height distribution. This current pulse of cascading electrons produced by MCP then will be gathered by an anode board underneath it

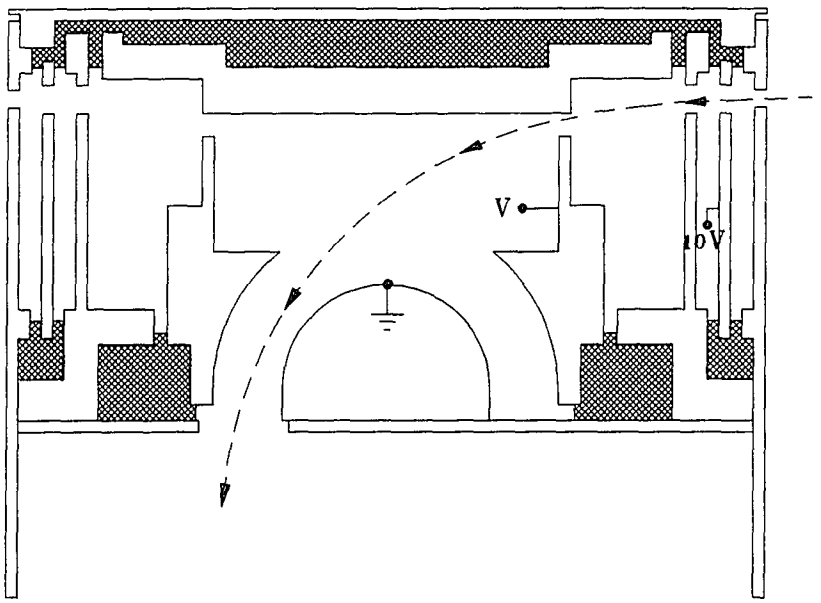

Figure 2.3: A cross-sectional view of CPA detector.

and pass out of the detector along the wire labeled "output". The inner hemisphere is swept over a range of voltage values to produce a corresponding energy spectrum as indicated in figure (2.2) labeled with "SWEEP". The pitch angle resolution is determined by the angle binning and position encoding anode on the anode board. On this flight, the electron ESA had 20 bins of 8° to cover 360° of image plane, the ion ESA had only 10 bins.

The CPA is a small, light-weight, inexpensive detector designed by Kletzing and Liou [1988]. Its cylindrical design provides 360° of angular resolution around its symmetric axis. Figure 2.3 shows a cross-sectional view of the CPA detector.

The CPA is an electrostatic retarding potential analyzer. The outer part of the analyzer, functioning as a collimator, consists of three pieces of conducting barrier with a small hole on each plate composing the entrance aperture. The center piece

of barrier is held at fixed voltage of 10 *volts* for rejecting the unwanted incoming ions while the others are grounded. Once an electron passes through the entrance aperture, it enters the inner part of electrostatic section from which the electrons are selected according to the voltages V being applied on the inner electrode. In figure 2.3 one can see that once an electron leaves the entrance aperture of the outer section, it suffers an electrical force from the inner electrode and deviates its trajectory towards the electrode. Electrons having too much energy will hit the top cap and too little energy will hit the electrode. Only electrons with energy within a certain window will be able to pass a small gap between the electrode and top-cap and successively go through the electrostatic section of the analyzer. The CPA is designed to analyze incoming particles in one plane. To achieve this, the energy coverage is substantially reduced at the high end. The energy to voltage ratio is about 1.7 and the energy window $\Delta E/E \sim 15\%$ on this flight. The CPA was deployed such that the local geomagnetic field is on the plan of entrance aperture to cover $0° - 180°$ full range of pitch angles.

The entire assembly was deployed outside the payload skin on an arm (See figure 2.4) so that the detector has unimpeded access to the plasma to reduce the effects of spacecraft potentials.

To acquire complete particle distributions fully in energy and angle in few milliseconds, to sample a large number of analog signals at rates over 10 Mhz, and to accept serial digital inputs from the PFP, a micro-processor based fast-event PCM system was used for system control. This system monitors and controls the performance of the particle detectors, accepts analog signals from the electric field measurements and magnetometer, and accepts serial digital inputs from the plasma

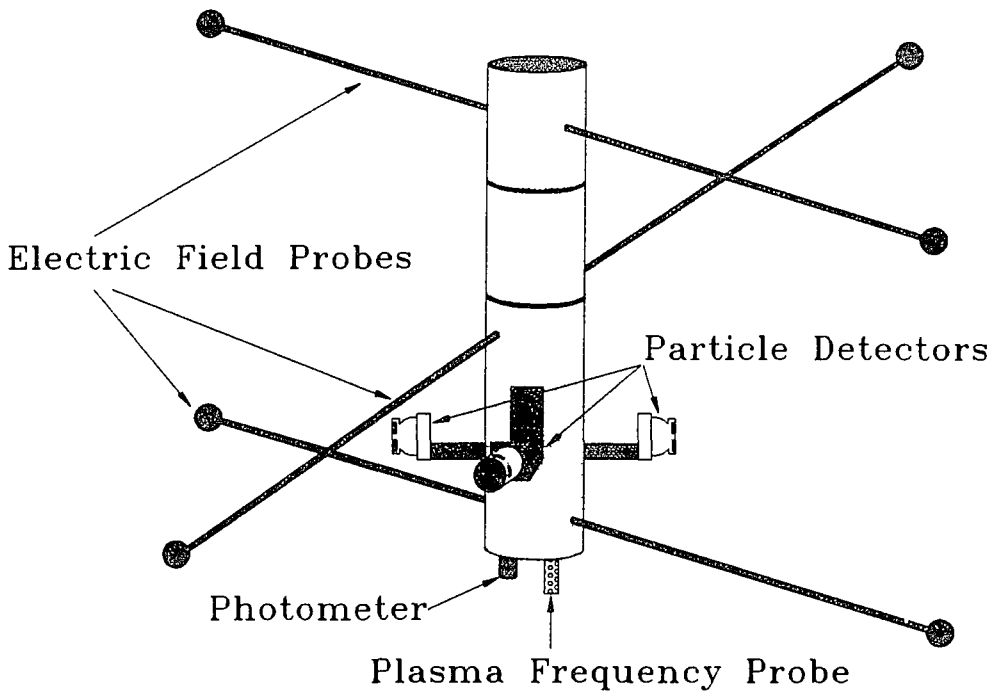

Figure 2.4: Payload configuration at main subsection.

frequency probe. All the data is then formatted into the digitally encoded telemetry stream and fed to the transmitter to be telemetered to the ground. There are four distinct operation modes executed by the micro-processor on CRIT-II experiment. The payload deployment was executed during the "engineering" mode in which few measurements were actually done except some routine data needed for ground check-out. In "preburst" mode, the HV was activated and the particle detectors started to accumulate data at the same rate as the telemetry link (in this case, 750 Kbits/sec). The "burst" mode, activated at the same time as the command to detonate the chemical canister, collects data at a much faster rate than the transmission rate of telemetry. All the collecting data were stored in a solid state memory for later transmission. When the memory is full, it enters the "postburst" mode in which the data

were sampled at a lower rate to allow burst data to be dumped into the telemetry stream. The buffer memory was completely emptied by transmission before entering the second "burst" mode. The sequence of events in the CRIT-II experiment is listed in Table A.1 in Appendix A.

2.2.2 Subpayloads

There were two particle detectors, one ESA and one CPA, provided by the University of New Hampshire to measure the nonthermal part of ions and electrons. Both detectors were identical to the ones used on the main payload. Electric field instruments, provided by Cornell University, consist of two sets of dipole probes and a single probe. These probes are positioned such that three components, but nonorthogonal, of electric field can be measured. The magnetometer was provided by the Danish Space Research Institute. It had about 2nT resolution and was capable of doing three dimensional measurement.

2.3 Geometric Factor of Particle Detectors

For an analyzer placed in an ambient differential flux $j(particles/sec\ cm^2\ str\ eV)$, the number of particles transmitted per second, or count rate $\dot{C}$, is given by

$$\dot{C} = \int_E \int_\Omega \int_A \delta(\mathbf{x}, \mathbf{v}, E) j dA d\Omega dE \tag{2.1}$$

where E refers to the kinetic energy of input particles, $\delta(\mathbf{x}, \mathbf{v}, E)$ is a unitless response function, $d\Omega$ is the incremental solid angle of incoming particle with respect to the normal direction of the entrance surface at the point of entrance, and A is the entrance area projected onto the plane normal to the particle direction. If the differential flux is constant over the entrance surface, the response function δ,

for a given applied voltage and look-direction, has the value of 1 for each of (x, v, E) corresponding to trajectories which strike the detector and zero otherwise. Therefore it determines the limits of integration over solid angle and energy. The surface integral is taken over any surface that is crossed once and only once by each trajectory reaching the detector. Usually this is the entrance aperture of the analyzer.

In practice, it is useful to define a factor which is a function of geometry of the analyzer only. This factor, called the energy dependent geometric factor, is defined by

$$g(E) = \int_{\Omega} \int_{A} \delta(\mathbf{x}, \mathbf{v}, E) dA d\Omega \tag{2.2}$$

in unit of $cm^2 - str$, if integrating $g(E)$ over E, we obtain the total geometric factor

$$G = \int_{E} g(E) dE \tag{2.3}$$

where the unit of G is $cm^2 - str - eV$. Since each particle striking the detector produces the same response, the variation of j within the range of acceptance of the detector cannot be measured. Hence the observed differential flux j can be approximated by

$$j = \dot{C}/G \tag{2.4}$$

This approximation will be used in chapter 3 for acquiring the differential flux from the measured count rate and the total geometric factor.

As mentioned earlier, there are two particle detectors used for the charged particle measurements. The ESA is a "capped hemisphere" type of analyzer which was first developed by the combined efforts of researchers at the University of California at Berkeley, the Max Planck Institute for Physics and Astrophysics at Garching, and

the University of Toulouse and it has been flown successfully for several sounding rocket and satellite experiments over a decade. A detector of this type can be easily modified to suit different physical parameter regimes. It's transmission performance has been tested in the laboratory by Carlson *et al.* [1983] at the University of California at Berkeley. A summary of their work is illustrated in figure 2.5(a) wherein Δ_1 is the gap of inner plate $(R_2 - R_1)$, Δ_2 is the gap of outer plate $(R_3 - R_2)$, Θ and σ are two truncation angles, which are the major design parameters as illustrated in figure 2.5(b). In figure 2.5(a) the normalized geometric factor, G/R_1^2, the mean of the product of the fractional velocity bandpass and the azimuthal angular bandpass, $< (\Delta v/v)\Delta\theta >$, and the particle energy to voltage ratio per unit charge, T_∞/qV, are expressed by different curves as functions of design parameters. It should be noted that the normalized geometric factor given in figure 2.5(a) is defined in velocity space, in units $str - \Delta v/v$. To convert it to the conventional total geometric factor G, in units $cm^2 - str - eV$, given by equation (2.3), it should be multiplied by a factor of $2ER_1^2$.

The CPA detector, however, has not been fully calibrated mainly because of the lack of laboratory instruments. The geometric factor which will be used to obtain the count rate was , according to the comparison with the ESA under the same source, similar to that of the ESA detector. In the next section, a simulation code will be developed to numerically calculate the transmission performance and the geometric factor.

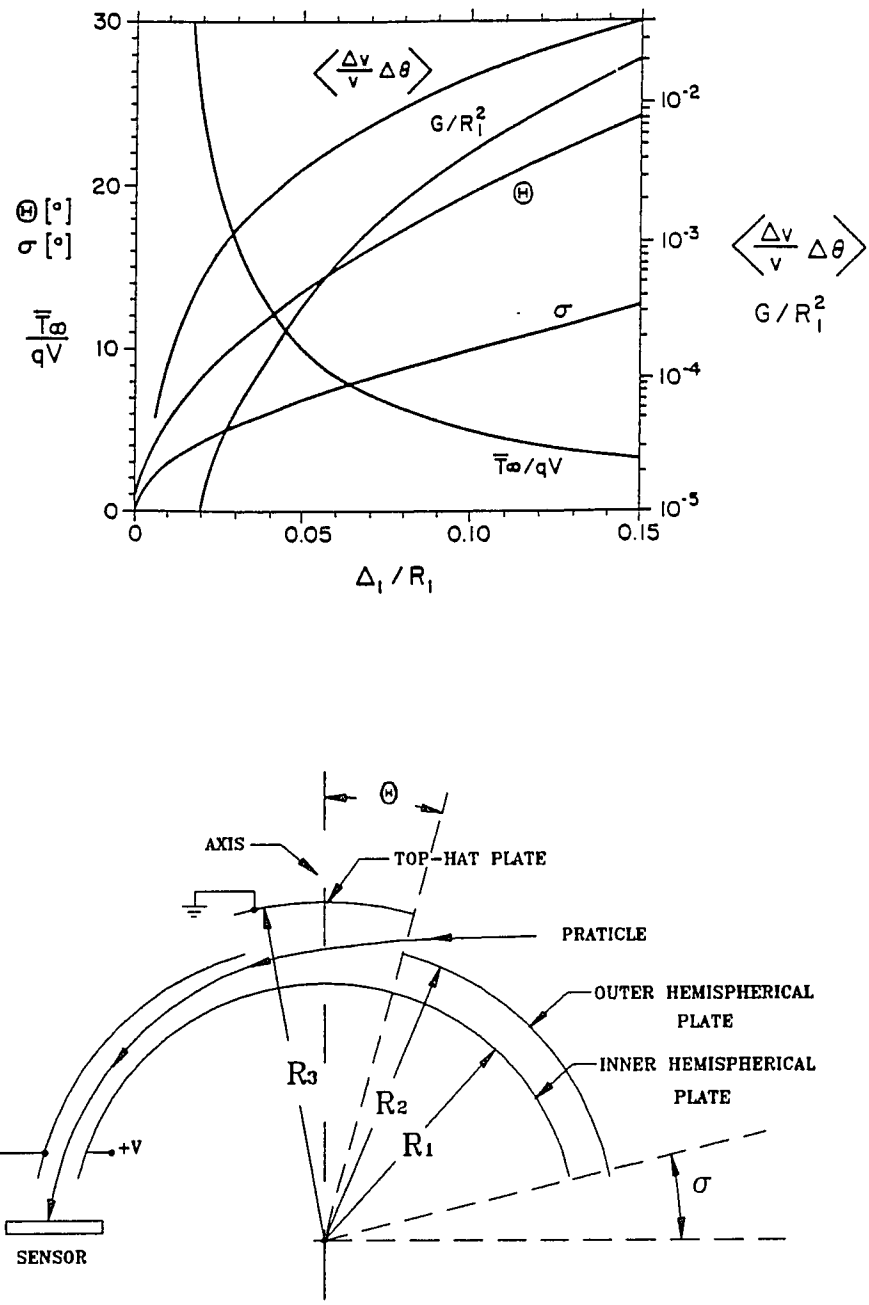

Figure 2.5: (a) Scaling of geometric factor as functions of design parameters (From Carlson, 1983). (b) Equivalent Cross-sectional view of "top-hat" electrostatic analyzer. Top-hat angle Θ, sphere truncation angle σ, and plate radii R_1, R_2, and R_3 are indicated.

2.4 Numerical Simulation of CPA

To calculate the geometric factor of CPA, the electrostatic potential inside the detector needs to be solved first. The response function, $\delta(\mathbf{x}, \mathbf{v}, E)$, in equation (2.1) then can be determined by solving a large number of the charged particle's trajectories.

The potential field, ϕ, inside a detector can be determined by solving the Laplace equation subjected with proper boundary conditions. The technique that was used to solve the Laplace equation is called the finite-element method (for example, see Huebner and Thornton [1982]). One advantage of the finite-element method over the finite-difference method is the relative ease with which the boundary conditions of the problem are handled. Many physical problems have boundary conditions involving derivatives and, in general, the boundary of the region is irregularly shaped like our particle detectors. Boundary conditions of this type are very difficult to handle using finite-difference techniques, since each boundary condition involving a derivative must be approximated by a difference quotient at the grid points, and irregular shaping of the boundary makes placing the grid points difficult. The finite-element method includes the boundary conditions as integrals in a functional that is being minimized, so the construction procedure is independent of the particular boundary conditions of the problem.

The general idea of the finite-element method is to minimize a functional instead of solving a differential equation. In our case, the system Laplace equation and its associated boundary conditions are

$$\nabla^2\phi = 0 \quad in\ D \tag{2.5}$$

$$\phi = V \quad on\ \Sigma_1 \tag{2.6}$$

$$\partial\phi/\partial\mathbf{n} = 0 \quad on\ \Sigma_2 \tag{2.7}$$

where D is the system domain, Σ_1 and Σ_2 compose the boundary of D, and $\mathbf{n}$ is the unit vector in the normal direction of the surface of Σ_2. By applying the variational principle and Green's theorem, the solutions of the differential equation (2.4) uniquely satisfy the functional

$$\begin{aligned} \delta I(\phi) &= \delta \int_D \frac{1}{2} \bigtriangledown \phi \cdot \bigtriangledown \phi d^3x + \int_{\Sigma_1+\Sigma_2} \delta\phi \mathbf{n} \cdot \bigtriangledown \phi d\sigma \\ &= 0 \end{aligned} \tag{2.8}$$

where $d\sigma$ is a differential surface area. Since $\phi = V$ on Σ_1, $\delta\phi = 0$ on Σ_1, and $\mathbf{n} \cdot \bigtriangledown\phi = \partial\phi/\partial\mathbf{n} = 0$ on Σ_2, thus we have

$$I(\phi) = \int_D \frac{1}{2} \bigtriangledown \phi \cdot \bigtriangledown \phi d^3x \tag{2.9}$$

and all functions ϕ that give the integral $I(\phi)$ a maximum or minimum value, or render it stationary, satisfy the Laplace equation and the boundary conditions. The finite-element method approximates this solution by minimizing the functional $I(\phi)$ over a smaller class of functions. Since the structure of the CPA is cylindrically symmetric, the Laplace equation reduces to

$$\frac{1}{\rho}\frac{\partial}{\partial\rho}\left(\rho\frac{\partial\phi}{\partial\rho}\right) + \frac{\partial^2\phi}{\partial z^2} = 0 \tag{2.10}$$

Then the equation (2.9) has an explicit form as

$$I(\phi) = \pi \int \left\{ \rho \left(\frac{\partial\phi}{\partial\rho}\right)^2 + \rho \left(\frac{\partial\phi}{\partial z}\right)^2 \right\} d\rho dz \tag{2.11}$$

Suppose that the domain D is divided into polygonal elements and that the potential field of ϕ within each element is assumed to be [Burden and Faires, 1985]

$$\phi^{(e)}(\rho, z) = \sum_{i=1}^{m} N_i(\rho, z)\phi_i \tag{2.12}$$

where r is the number of nodes assigned to element (e), the $N_1, N_2, ..., N_m$ are linearly independent piecewise linear polynomials, and $\phi_1, \phi_2, ..., \phi_m$ are the discrete nodal potential. Some of these constants, say, $\phi_1, \phi_2, ..., \phi_n$ are used to minimize the functional I, while the remaining constants, $\phi_{n+1}, \phi_{n+2}, ..., \phi_m$ are used to ensure that the boundary condition $\phi = V$ on Σ_1. By substituting equation (2.12) into equation (2.11) we obtain the discretized functional $I(\phi^{(e)})$ for one element expressed in terms of the discrete nodal potential. Requiring that $I(\phi^{(e)})$ be a minimum is equivalent to requiring that

$$\frac{\partial I(\phi^{(e)})}{\partial \phi_i} = 0, \; i = 1, 2, ..., r \tag{2.13}$$

Hence for a typical node i we have

$$\frac{\partial I(\phi^{(e)})}{\partial \phi_i} = 0 = \sum_{i=1}^{r} \phi_j \int_D \left\{ \frac{\partial N_i}{\partial \rho} \frac{\partial N_j}{\partial \rho} + \frac{\partial N_i}{\partial z} \frac{\partial N_j}{\partial z} \right\} \rho d\rho dz \tag{2.14}$$

This set of equations can be written as a linear system:

$$A\mathbf{c} = \mathbf{b} \tag{2.15}$$

where $A = (\alpha_{ij})$ is an $n \times n$ square matrix defined by

$$\alpha_{ij} = \int \int_D \left\{ \frac{\partial N_i}{\partial \rho} \frac{\partial N_j}{\partial \rho} + \frac{\partial N_i}{\partial z} \frac{\partial N_j}{\partial z} \right\} \rho d\rho dz \tag{2.16}$$

$\mathbf{c} = (\phi_1, ...\phi_n)^T$ and $(\beta_1, ..., \beta_n)^T$ are defined by

$$\beta_i = - \sum_{k=n+1}^{m} \alpha_{ik} \phi_k \qquad i = 1, 2, ..., n \tag{2.17}$$

The particular choice of basis functions is very important since an appropriate choice can often make the matrix A positive definite and banded. The remaining procedures are choosing the element shape and the interpolation function $N(\rho, z)$. To

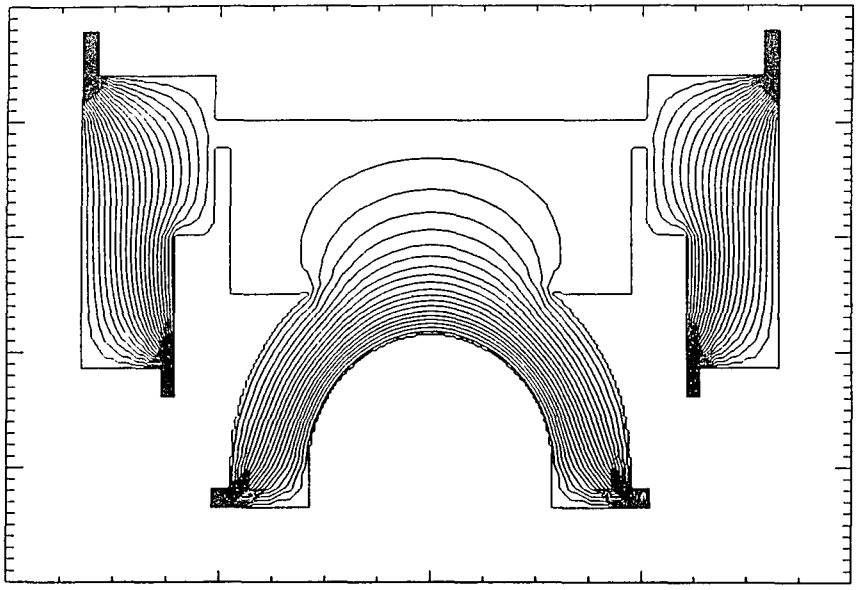

Figure 2.6: Potential contour for the CPA detector.

begin the procedure we divide the region D into a collection of triangles. The interpolation function is chosen as a linear function of independent variables. For each $i = 1, 2, ..., n$ elements we have

$$N_j^{(i)} = a_j + b_j\rho + c_j z \qquad for \;\; j = 1, 2, 3 \tag{2.18}$$

where $N_j^{(i)}(x_k, y_k) = 1$ if $j = k$, otherwise $N_j^{(i)}(x_k, y_k) = 0$. The coefficients a_j, b_j, and c_j will be determined by the coordinates of the three nodes of ith element.

Substituting equation (2.18) into equation (2.16) and boundary conditions into equation (2.17), the linear system equations (2.15) can be solved numerically. The potential at each node is the simultaneously solution of the linear system. The final solution of the contour potential inside the detector is shown in figure 2.6.

Once the potential field is solved, we can use it to calculate the geometric factor of

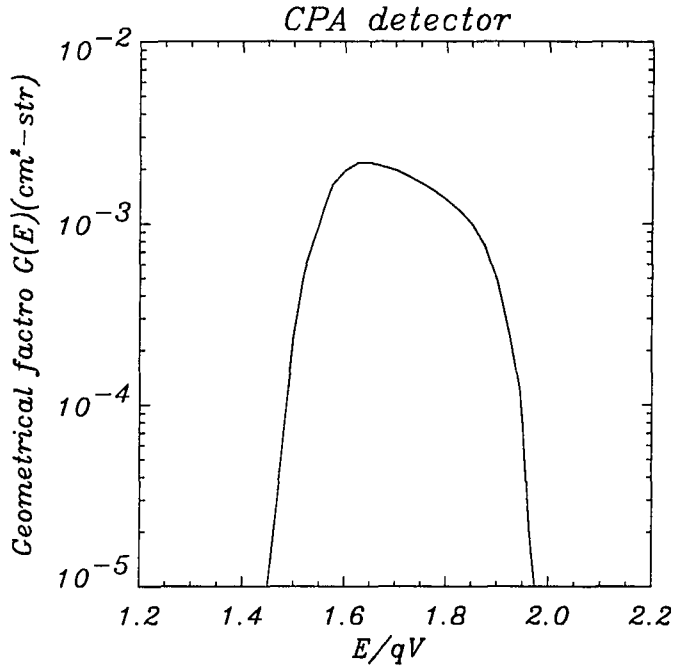

Figure 2.7: Geometric factor as a function of E/qV shows the energy window of CPA detector.

the detector by solving the response function. The particle trajectories will be solved by using the 4th order Runge-Kutta method [Press et al., 1986]. This simulation was done by using about $5. \times 10^5$ test particles to cover over all the possible distribution of the particles and its result is shown in figure 2.7.

The E/qV peaks at 1.7 and $\Delta E/E \sim 0.18$ are consistent with the laboratory testing. The total geometric factor can be given by integrating $G(E)$ over the energy, this gives $G = 3.53 \times 10^{-4}\ cm^2 - str$ for single bin and is very close to what we expected from calibration by comparing it with the ESA detector. This number will be used for converting the observed count rate to the differential flux.

CHAPTER 3

CRIT-II Data Overview

3.1 Introduction

The CRIT-II sounding rocket experiment perhaps is the most successful rocket campaign to date to test the Alfvén's critical ionization velocity hypothesis in space. It incorporated the electric and magnetic field detectors and the particle detectors to perform *in situ* measurements inside and outside of the barium stream. In addition to its immense amount and reliable data output, unlike others, the CRIT-II offered two barium release experiments at once. Both releases, almost identical, were conducted at the same altitude, and it was expected that the two releases would generate an identical barium beam. The only difference between the two releases was the separation of release points from the main payload. The consequence of this was the difference in the neutral barium density and beam width at the observation location. This arrangement enables us to study the same phenomenon in different parameter regimes. The ionospheric and beam parameters for the two releases are listed in Table 3.1.

The preliminary measurement result from the first release has been analyzed and published [Swenson et al., 1990; Torbert et al., 1992], but there are still many results which remain unknown and need to be analyzed in detail. The main subject of this

Table 3.1: Table 1:Ionospheric plasma and barium beam parameters.

Ionospheric plasma parameters	
Magnetic field B_0	0.43 $Gauss$
Plasma density n_p	$5.41\times10^5 cm^{-3}$
Neutral oxygen density $n_n(420km)$	$1.66\times10^9 cm^{-3}$
Alfvén velocity v_A	319 km/sec
Barium beam parameters	
Main payload to first release	1.585 km
Main payload to second release	3.881 km
First release injection angle	$57°(L_{\|\|} = .38km)$
Second release injection angle	$44°(L_{\|\|} = .72km)$
Barium gyro-radius ($12km/sec$)	400 $meters$
Barium energy ($13km/sec$)	120 eV

chapter is to overview and, if possible, to systematically explain the whole data output from the particle detectors for both releases. The basic results show a high consistency in regard to the physical intuition and theoretical expectation. However, as will be seen, there are a lot of phenomena that cannot be fully understood and need to be investigated in detail.

This chapter is organized as follows. We will begin our discussion with the data originating from the main payload for the first release, then follow with the second release. The raw data will be generally presented in the style of a time-energy spectrogram for both ions and electrons. The quantitative analysis of the data for densities, temperatures, and barium production rates will be also given. Lastly, a brief summary is to end this chapter.

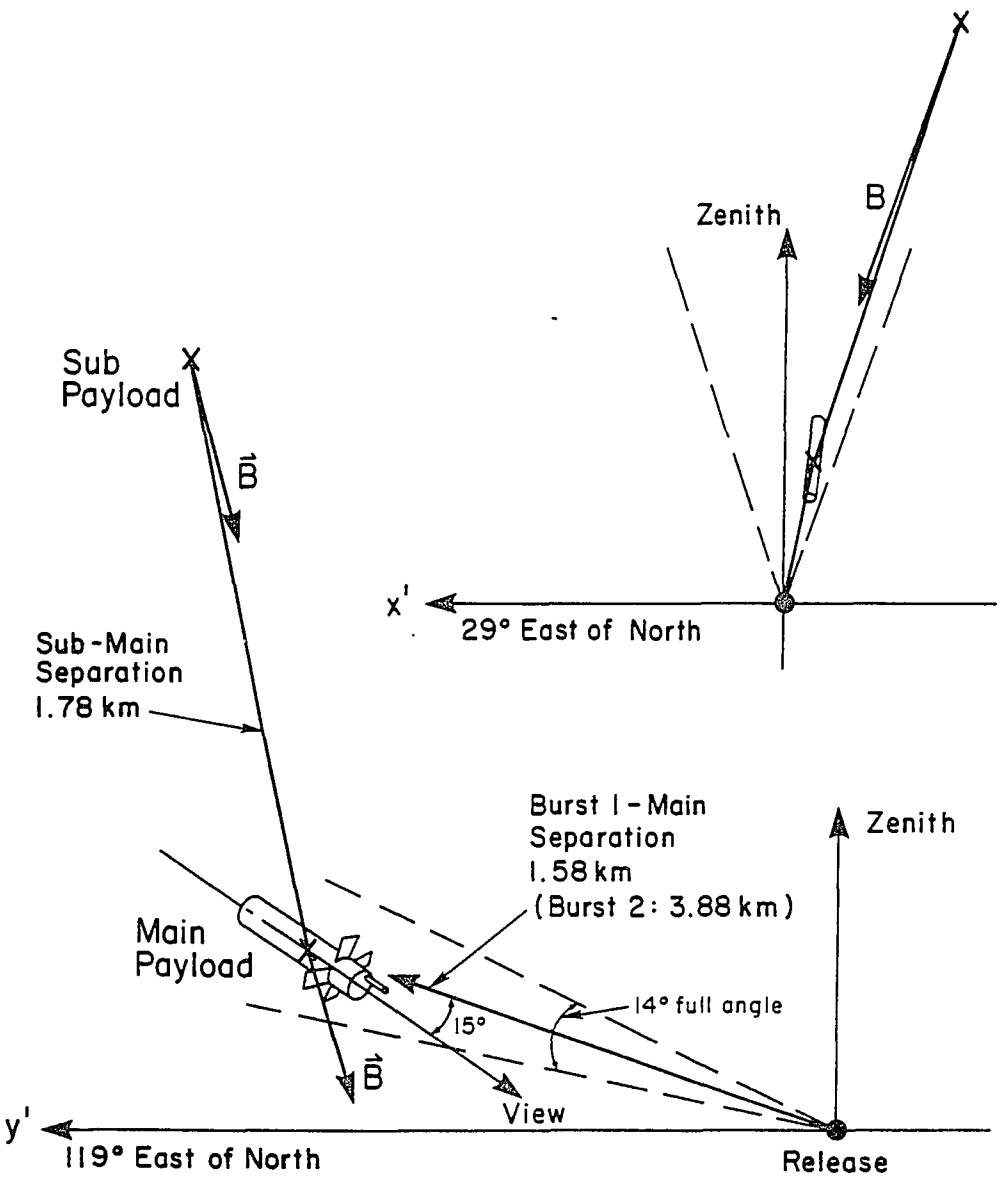

Figure 3.1: Release orientation of CRIT-II (from Torbert *et al.*, 1992).

3.2 CRIT-II Release One

The main payload was deployed near the center of the path of the neutral barium beam to diagnose the CIV activities inside the neutral cloud. Besides the electrostatic analyzer, The University of New Hampshire provided two state-of-the-art photometers on board. They were mainly used to determine the detonation time of the chemical canister and to measure the electron flux. The use of the "Green" photometer was for measuring the resonant line of atomic barium ($^1S_0 - ^1P_1$) at 5535 Å and the "Red" photometer for the atomic oxygen ($^3P - ^1D$) emission line at 6300 Å, respectively. Both photometers had $\sim$ 13° field of view and were deployed to be pointed back along the rocket axis to the release, but due to errors in the Attitude Control System (ACS), this direction was 16° off the direct view as indicated in figure 3.1. Thus only a small fraction of barium came to the field of view of the photometer initially. Since CRIT-II was launched at dusk (8:40 pm local time), both photometers were unfortunately exposed in the twilight. One can see that both surface brightnesses were modulated by rocket spin period at 4.92 seconds (see figures in Appendix B), and thus showed a directional property of the source of photons. Also, the "Red" brightness was brighter than the "Green" by order of two, this can justify that the background photons were coming from the sunset. After taking off the background photons, both results are illustrated in figure 3.2. The time axis is referenced to the zero time of the burst mode or 348.262 s of the flight time. One can see that a burst of light was measured by both photometers, starting at about 12 ms. Therefore the zero time for the barium release should be offset by this time delay from the burst time (348.274 s of the flight time). One will see later that this requirement for time accuracy is important to the data interpretations.

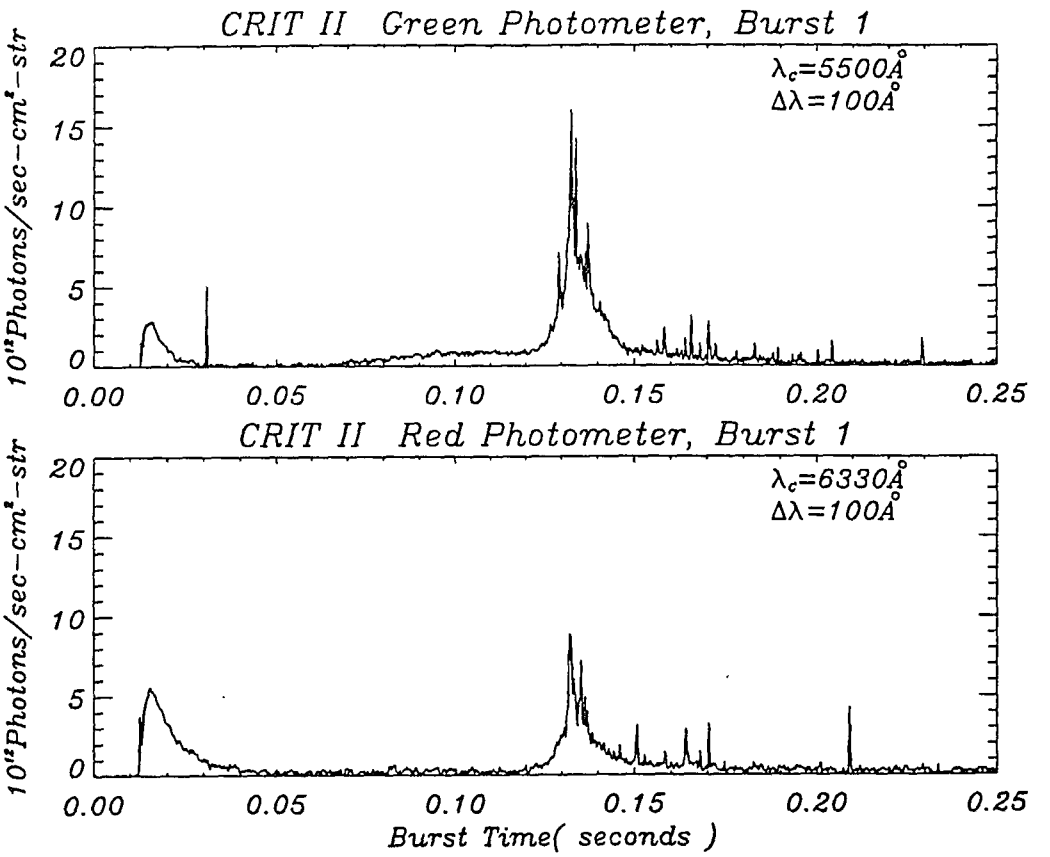

Figure 3.2: Brightness from the Green (top) and Red (bottom) Photometers during the first release of CRIT-II.

For a given distance, one can determine the energy of the neutral barium as a function of time. The neutral barium time-energy dispersion for both releases is shown in figure 3.3. Based on the SR90 strontium release results, the observed neutral barium distribution was angularly near Gaussian and azimuthally independent. By utilizing the differential velocity distribution of the neutral barium [Stenbaek-Nielsen et al., 1990a], the neutral barium density at distance r and angle θ (measured from the beam axis) at time t can be expressed by

$$n(r,\theta,t) = \left(v\frac{\partial N}{\partial v}\right)_{v=r/t} \frac{f(\theta)}{r^3} \tag{3.1}$$

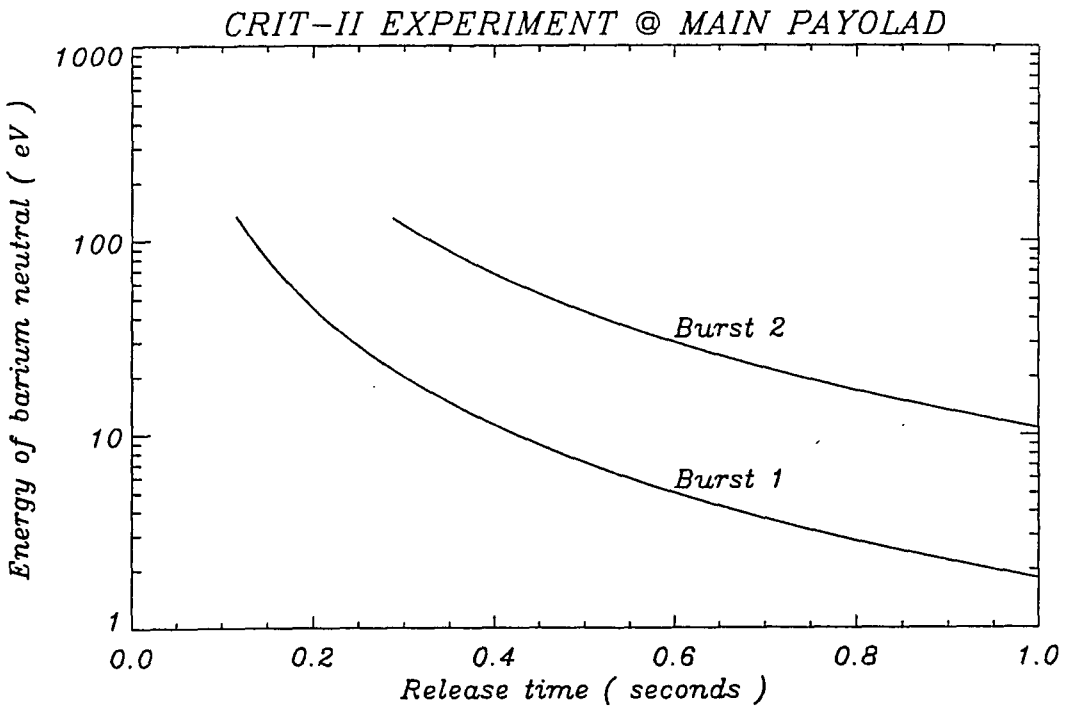

Figure 3.3: Energy of Barium beam for two releases.

where $f(\theta) = Cexp(-\theta^2/\theta_w^2)$ and θ_w is the e-folding maximum half angle of the neutral beam. The constant C is determined from the normalization condition

$$\int_\Omega f(\theta) d\Omega = 1 \tag{3.2}$$

Accordingly, the time evolution for the neutral barium density at the location of the payload for both releases is calculated and illustrated in figure 3.4. One of the most important features predicted by this neutral barium model is that the neutral barium beam cannot reach the main payload until 0.13 seconds of the burst time.

The brightness of the barium (BaI) excitation line, after detonation, increased with time from 0 to 1×10^{12} $photons/cm^2 sec\ str$. This is simply due to the fact that more excited barium atoms, probably due to the electron impact collision, came into the field of view of the photometer which initially looked at directions about 15° off

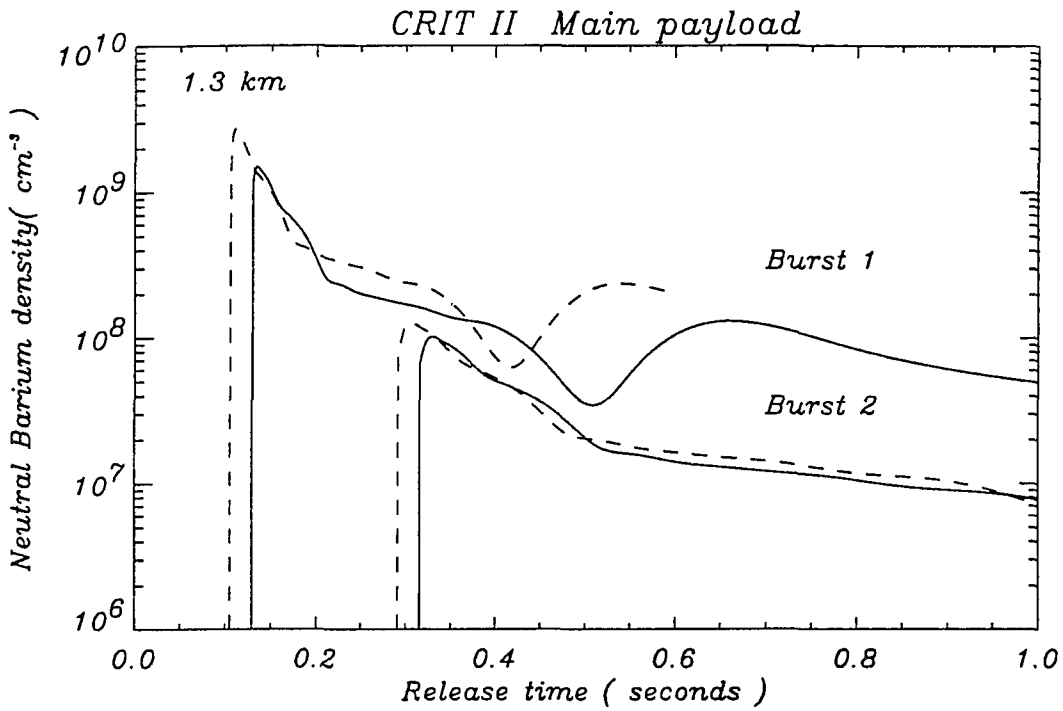

Figure 3.4: Modeled neutral barium density at main payload (solid lines) for both CRIT-II releases. The broken lines are the neutral barium density at 1.3 *km* and 3.6 *km* from the release point

from the release point. There is a big "flash" occurring at ~ 0.13 *s*. Coincidentally, this is the exact time the dense barium beam reaches the payload as predicted by the neutral barium model. It is believed that this "flash" could not be created by barium-electron collisions because it requires a hot electron flux at least 100 times higher than that observed. It has been suggested by N. Brenning (unpublished manuscripts) that this flash could result from hot electron excitation of water vapor, sputtered by neutral barium collisions upon the payload surface, emitting a continuous light spectrum. The "red" emission from oxygen atoms was less intense than the "Green" emission from barium atoms after detonation. Presumably, both excitation lines were mainly induced by the electron impact collision. The cross section for the

excitation state of atomic oxygen ($^3P - ^1 D$) is about 2.5×10^{-17} cm^2 [Thomas and Nesbet, 1975], which is smaller than the barium resonance cross section by two orders of magnitude. With the same electron source, it would imply that the ionospheric neutral oxygen density (about 1.6×10^8 cm^{-3} according to the MSIS Neutral Atmosphere Model) should be two orders of magnitude larger than the neutral barium density. However, this is not consistent with the neutral barium model from which the neutral barium density was greater than the density of neutral oxygen until $\sim$ 0.4 seconds (see figure 3.4). This suggests that the electron impact may not be the only source of the red emission. A possible source of the red line emission could be attributed to the excitation of ground state $O(^3P)$ atoms into the metastable $O(^1D)$ state by collision with fast neutral barium or oxygen beams. On the other hand, since the oxygen metastable state, $O(^1D)$, is known to have a radiative lifetime of 110 seconds, the source of the red light seen by photometer could be the residue of metastable atomic oxygen excited by detonation.

3.2.1 Ion ESA

There was an ESA on the CRIT-II main payload provided by UNH to measure the ion particles. Since there is no mass resolution for this detector, pre-selected ion energies from 5 eV to 1000 eV were set to measure the nonthermal part of ions only. There are a total of 10 channels with angular resolution varying from 20 to 60 degrees to look in 10 different directions. By using the linear interpolation technique, a full 360° view of the ions energy spectrogram can be reconstructed. There are three continuous ion energy spectra starting from 0.089 to 0.105 seconds of burst time (.533 ms for a complete energy sweep) shown in figure 3.5. In each pancake-like energy spectrogram, the vertical axis represents the direction of the neutral barium beam and its scale represents the energy of ions in electron volts. A straight line segment which shows the direction of the Lorentz force is also provided (the ambient magnetic field is approximately pointing out from the paper). An electric field component along the beam direction is illustrated on the top panel to provide a better understanding of the wave-particle relations. The unit for the electric fields is in $volt/m$. In figure 3.5, a narrow energy band of less intense ions (blue strip) with central energy of 25 eV was first seen at about 0.089 seconds then followed by three discrete energy bands of ions at 0.094 seconds. One can see clearly that a band of 120 eV ions was seen in the direction of the beam but with small angular spread. It could be the first locally ionized barium seen by the detector. However, this time would correspond to a velocity of 19.4 km/s of barium neutrals, it is about 6 km/s faster than that predicted by neutral barium model. There are two lower energy bands of ions with larger angular spread from the beam direction to the direction of $\mathbf{V} \times \mathbf{B}$. They must be ions with smaller mass and consequently have smaller

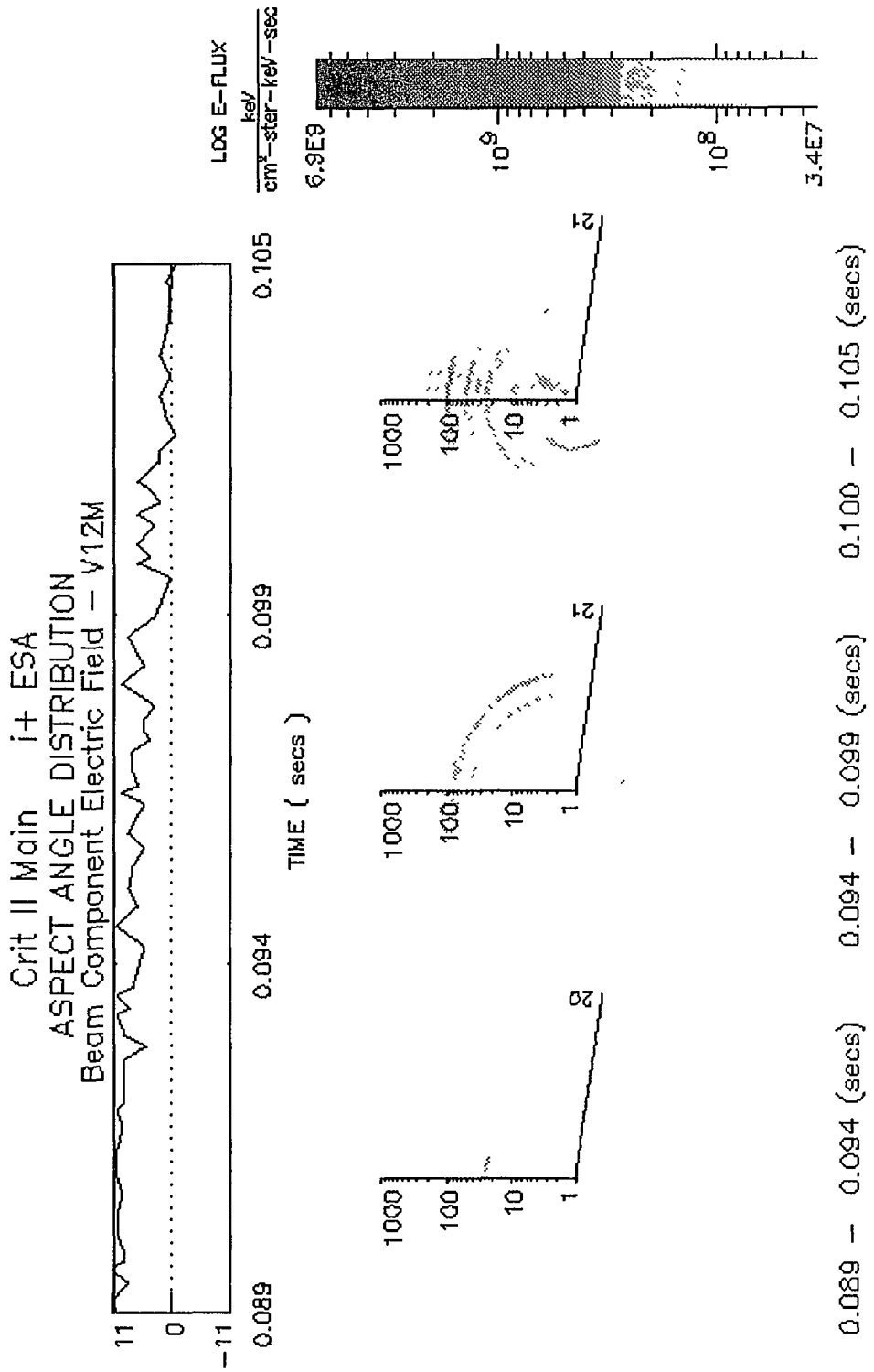

Figure 3.5: Ion differential energy flux spectrogram in the first release. The ambient magnetic field is approximately pointing out from the paper.

energy and gyration period to allow more angular diffusion before being observed. At about 0.1 seconds, ions were scattered into lower energy. From the energy point of view, what are these ions with energy far below the barium neutral energy? As was proposed by Torbert *et al.* [1992], these are the collisionally accelerated oxygen atoms being pushed ahead of dense neutral barium then charge-exchanged with the ambient oxygen ions. A simple theoretical model based on this suggestion has been constructed and successfully explained this low energy ion precursor. We will present it in chapter 5.

The first substantial ions (green spot), with differential energy flux of $\sim 4 \times 10^8$ $keV/cm^2 sec\ str\ keV$, were observed at 0.105 seconds as shown in the first panel of figure 3.6. These ions have a wide energy band ranging from 20 eV to 120 eV. At about 0.12 seconds, the ion differential energy flux drastically increased ten-fold to about 6×10^9 $keV/cm^2 sec\ str\ keV$. During this time, the center point of the energetic ions was 10° off from the beam direction. This 10° off could be due to the Lorentz force which deflected the ion trajectories before they were detected. However there would be due to the poor angular coverage provided by the detector. There was no channel which looked exactly at the beam at that time. The nearest one, 4AB, was about 10° to the right of the beam direction on the detector plane, which is the exact place where the most intensified ions were located. Therefore, we can conclude that these are the new born ions which were picked up almost immediately by the detector in the leading edge of the ionizing neutral cloud. If we consider the fastest barium which reaches the payload at $\sim$ 0.12 seconds (third panel in figure 3.6), it gives a barium velocity of 15 km/s, which is still faster than 13.5 km/s predicted by the neutral barium model. This timing inconsistency could be due to the errors in

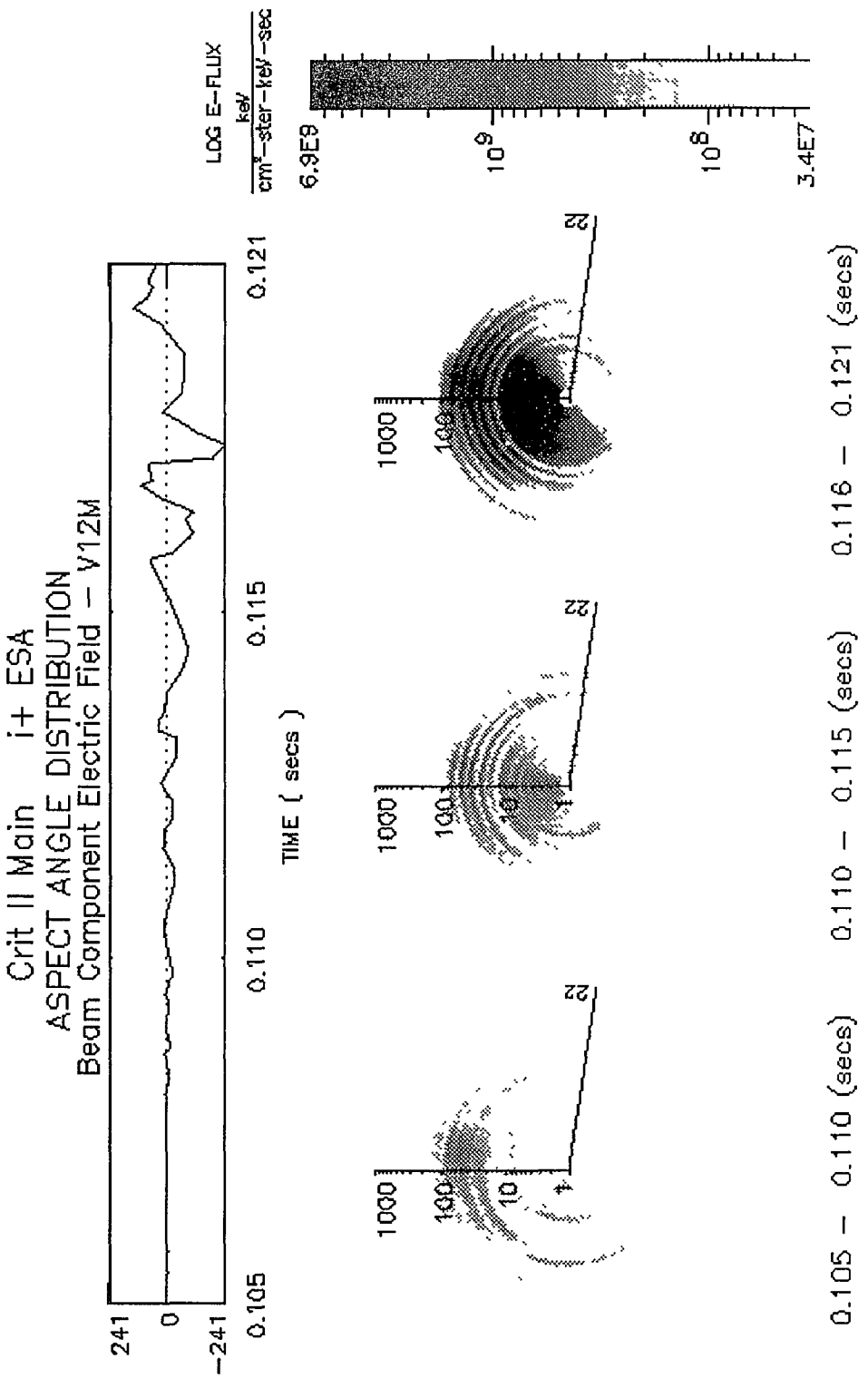

Figure 3.6: Ion differential energy flux spectrogram in the first release. The ambient magnetic field is approximately pointing out from the paper.

determining the separation distance of the main payload from the release point. On the other hand, the optical measurement, performed on the ground, which is used for modeling the neutral barium distribution could have missed the very fast but optically thin barium cloud in the leading edge of the barium beam. One important phenomenon in figure 3.6 is that ions were diffused into lower energy all the way down to 5 eV. At the same time, the wave activity was very strong. It could be that the ion energy was fed to the electric field perturbations during this time.

A time-energy spectrogram, 3CD, of one of the ion ESA channels is shown in figure 3.7. The pitch angle (angle between the neutral beam and the magnetic field) and the aspect angle (measured from the neutral beam direction) of this channel are provided on the top panel in the same plot. The main barium activity begins at 0.13 seconds with intense fluxes at 120 eV/q, which is precisely the energy indicated in figure 3.1. In fact, the energy-time dispersion curve follows very closely the bright red intensified band in figure 3.7 that ends around 0.45 seconds. These barium ions were thought to be created locally to the payload. However, this is not consistent with the measurement of the aspect angle, which was about 70° off the beam direction. On the other hand, these barium ions could have been created some time about 30 ms earlier and then gyrated about 1/6 of its cycle before reaching the payload. In fact, the 4CD channel, which was set to measure the direct beam ions, does agree with the energy dispersion curve in the first 200 ms after arrival of the fastest barium beam as shown in figure 3.8, but the ions disappear after that time. It suggests that the local ionization might be too weak after 0.3 seconds because the neutral density is too low. However, during this time the density is still high enough at a point of about one gyro-radius up stream to the main payload, also the hot electron density may

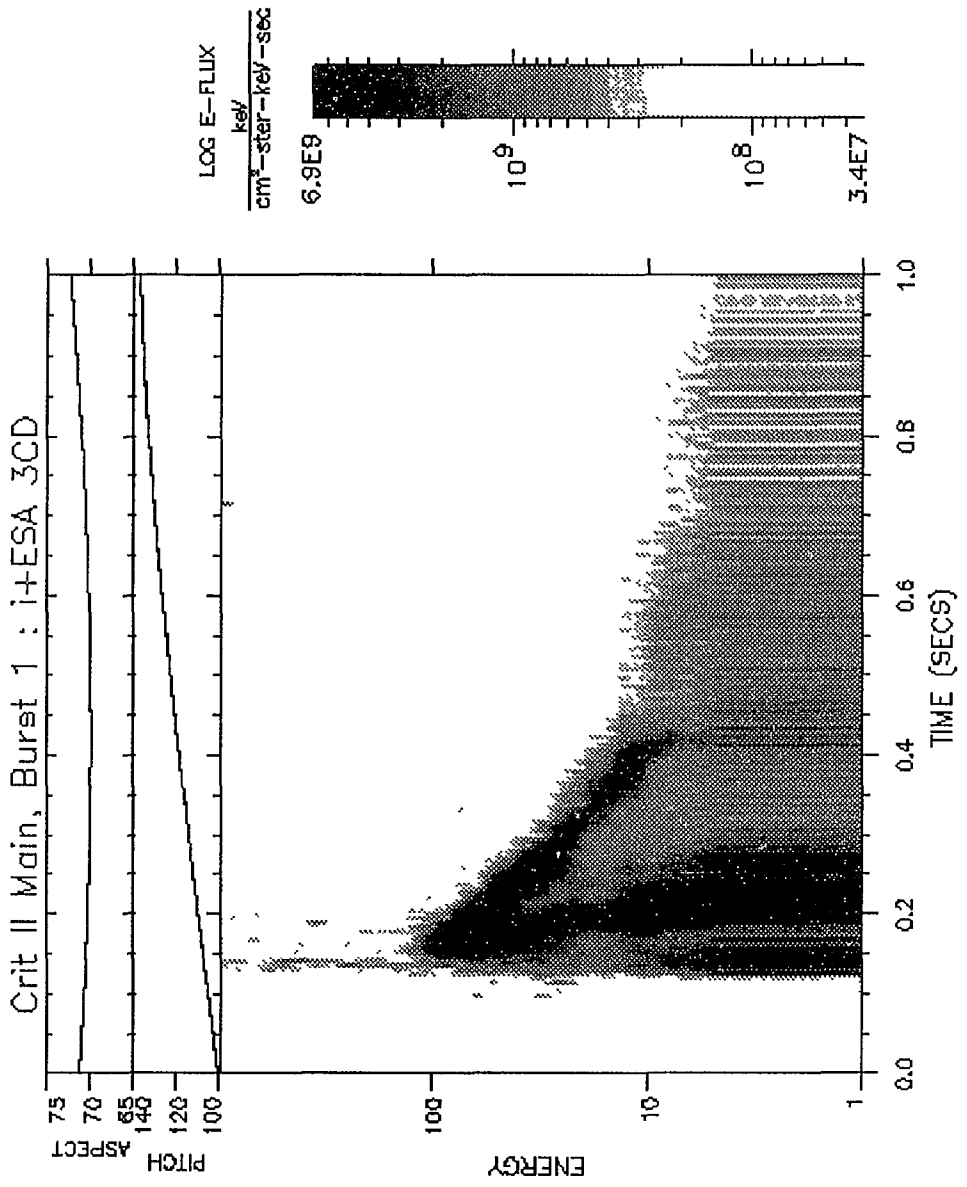

Figure 3.7: Ion differential energy flux spectrogram of channel 3CD in the first release.

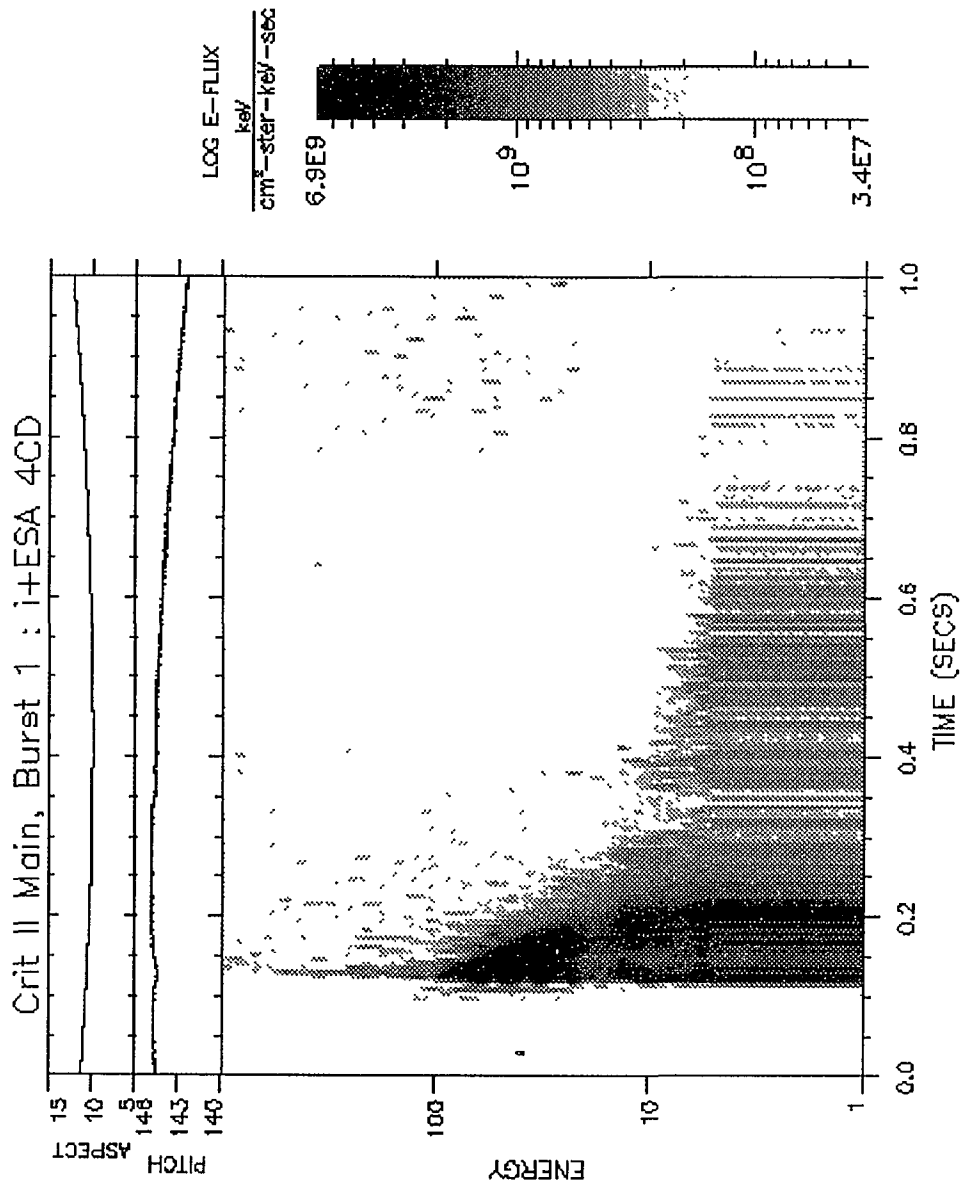

Figure 3.8: Ion differential energy flux spectrogram of channel 4CD in the first release.

be higher. Therefore, the ionization of barium could have lasted longer there. The new born ions can travel to the payload and be measured by 3CD. Coincidentally, the neutral density minimum occurs at $\sim$ 0.4 seconds which is exactly the time that ionization ceased at 3CD channel.

Interestingly, there is a second band of ions in 3CD, decaying from the early energetic ions at 120 eV into a low energy distribution, that terminates around 0.24 seconds. According to the wave data [Swenson, 1992], the most active large amplitude waves occurred at $\sim$ 0.13 seconds, the time at which the fastest main barium beam arrived on the payload, and lasted for about 0.1 seconds (see figure 3.8). It suggests that the kinetic energy of ions was fed to the waves quickly. Actually, at the same period, this barium ion energy decay can be seen on other channels (see figure 3.9) Therefore, barium ions were not only losing their energy to the waves but also were scattered into different direction by large wave fields. Another possibility is that during this time period (from 0.1-0.24 seconds) the electron energy and density are very high and double ionization is very likely to occur. For a doubly charged barium having the same energy as a singlely charged barium, it requires less voltage to be collected by the electrostatic detector, which results in a lower energy spectrum.

Figure 3.10 shows the time-energy spectrogram of a near 90° pitch angle channel, 5AB. One can clearly see that a large ion spike appears at 0.13 seconds and repeats itself but in weaker image at 0.32, 0.53, and at 0.74 seconds. Also loop-type ions were seen at 0.45 seconds and reappears itself but weaker at 0.7 seconds. These times are separated approximately by the ion gyro-period. Apparently, these are "bunches" of barium ions gyrating around the payload. On the other hand, one can also see that the low energy population of ions were modulated by oxygen gyro-

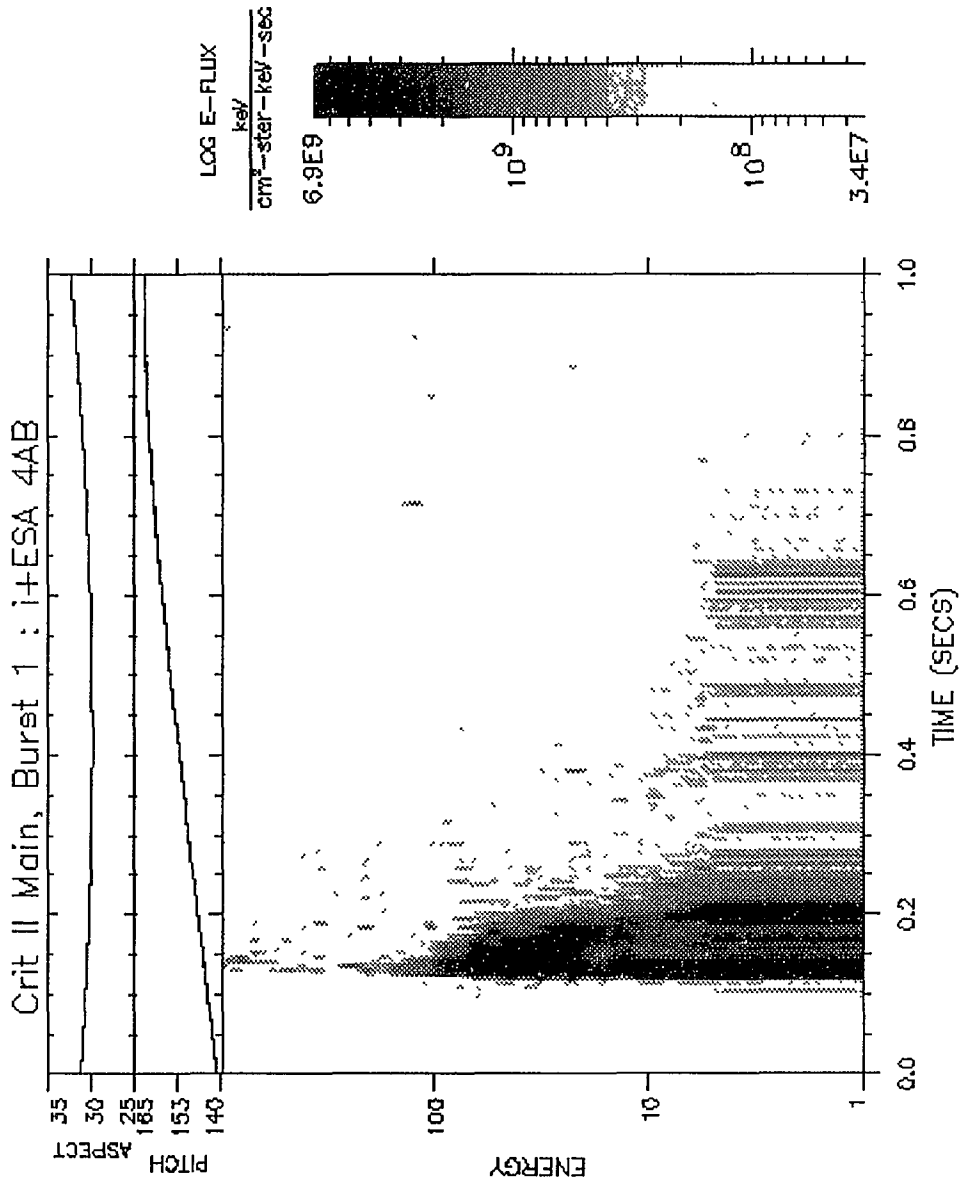

Figure 3.9: Ion differential energy flux spectrogram of channel 4AB in the first release.

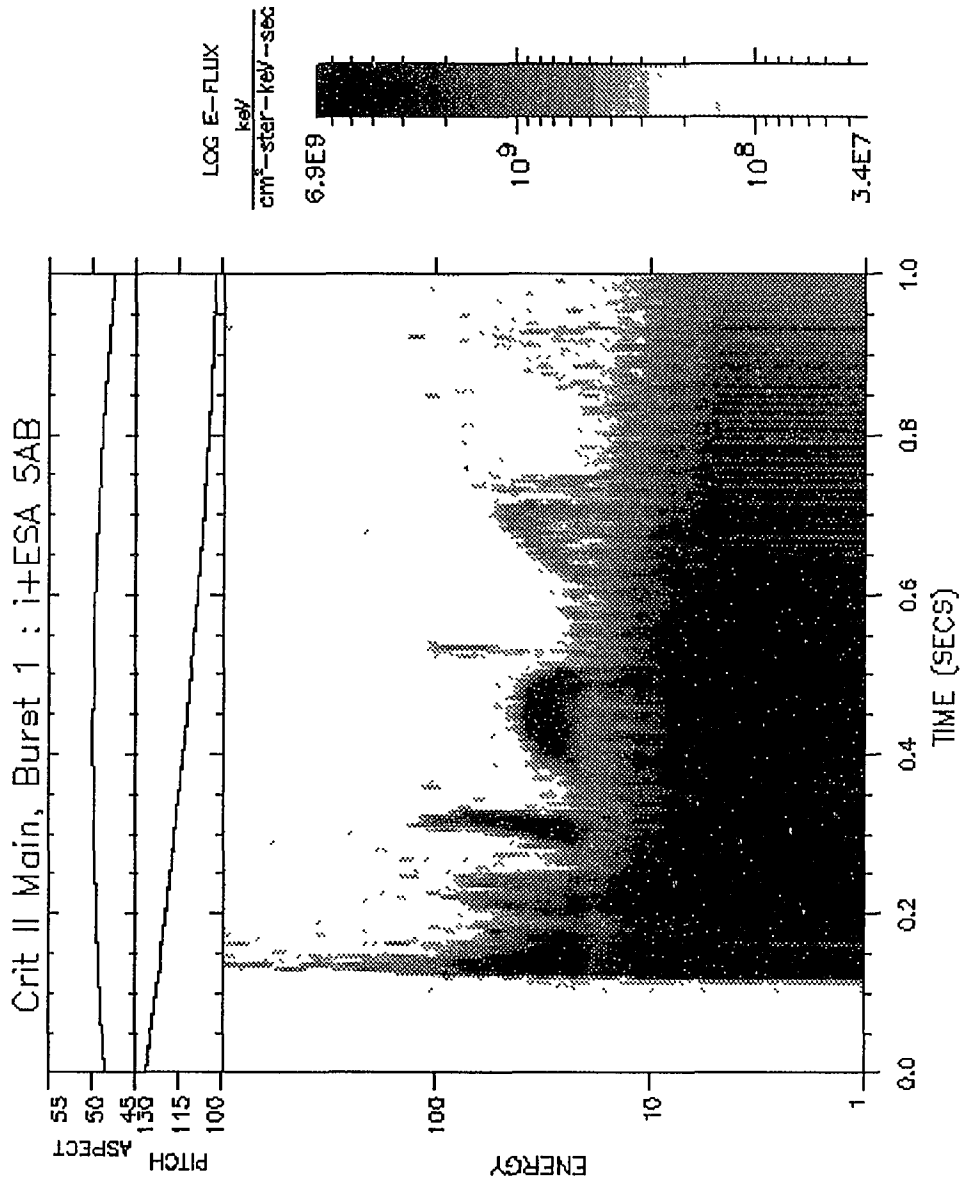

Figure 3.10: Ion differential energy flux spectrogram of channel 5AB in the first release.

frequency in figure 3.10 from 0.24 (at 20 eV) all the way to 1.0 seconds (down to 7 eV). These oscillations could result from a convecting spatial gradient in a heated background oxygen population [Torbert et al., 1992]. However, It's not clear yet how the background oxygen ions were heated.

3.2.2 Electron ESA

The electron ESA detector was designed to measure the energetic electrons ranging from 5 eV up to 1000 eV. Unfortunately, this detector suffered saturation due to over current of the sensors HV supply and completely shut down during the passage of the neutral beam. This period corresponds exactly to the time of the "flash" seen in figure 3.1. Also, this detector could have been damaged because it never recovered after saturation.

3.2.3 Electron CPA

The electron CPA detector was designed to measure the heated electrons in energy ranges from 1 eV to 170 eV. There are 12 channels on this detector to look at 12 different pitch angles. The data of one channel of near 0° pitch angle, CPA04, is presented in figure 3.11. Apparently, the electron heating, resulting in a superthermal electron tail, was observed. One can see that the low energy ($\ll$ 10 eV) electrons appear as early as 70 ms of burst time and a significant amount of heated electron ($\sim$ 10 eV) occurs at $\sim$ 0.1 seconds with differential energy fluxes exceeding 10^{10} $keV/cm^2 sec\ str\ keV$. This is definitively consistent with the photometer result. However, according to the neutral barium model, the fastest collisional oxygen can not reach the payload until $\sim$ 80 ms. This implies that these electrons were not locally created. On the other hand, they could have been created somewhere

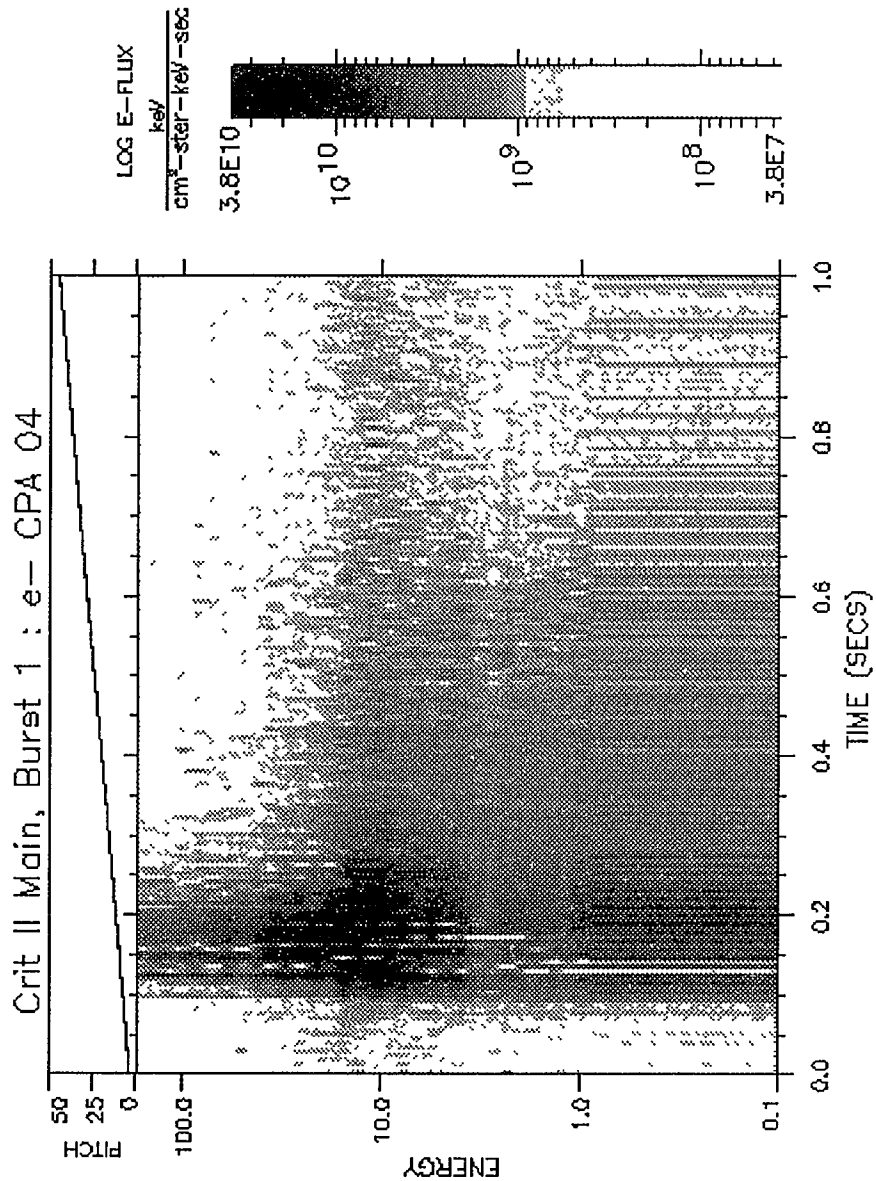

Figure 3.11: Electron differential energy flux spectrogram of channel CPA04 in the first release.

near the release point and then convected to the payload at a faster speed than the neutral beam. A possible explanation is: since the barium cloud was released at 57° to the magnetic field, it took only ~ 71 ms for the fastest oxygen beam to arrive at the place where it was connected with the main payload by the same geomagnetic field line. The electron heating could have taken place there and hot electrons could easily have been propagated up along the magnetic field line to the payload in a fraction of a millisecond. The preheated electrons (seen before the time at which the fastest barium arrived) therefore could be due to the collisional oxygen beam related plasma heating. Actually, before 0.11 seconds the wave structure is near the ambient oxygen lower hybrid frequency. A model based on the lower hybrid heating theory has been developed to explain the electron heating during this period and will be presented in chapter 4.

A second band of heated electrons can be seen upon the arrival of the main barium beam, producing electrons with energy above 100 eV and differential energy fluxes exceeding 10^{10} $keV/cm^2 sec\ str\ keV$. At that time, the electron fluxes became so large that the CPA detector began saturating (blue streaks in the intensive region). In figure 3.11, the electron heating ceased at $\sim$0.55 seconds. If the energetic ions were locally produced by these hot electrons by impact ionization, one would expect that the barium ionization would have ceased at this time. However, this is not exactly the case as observed by the ion detector. The barium ionization actually stopped earlier, at $\sim$ 0.45 seconds as shown in figure 3.7. We believe that after this time, the density of neutral barium is too low (at least one order of magnitude less than its local maximum) to produce substantial ionization yields.

The electron distribution seems isotropic during the first two-tenth seconds

(0.1~0.3 seconds). This period corresponds to the active phase at which the ion-wave interaction or the CIV effect was most operative. This electron isotropy was also seen by Star of Lima [Newell, 1985a]. Presumably, if the electron heating occurred preferentially along the field line as a result of the lower hybrid instability [McBride et al., 1972], a balance among the rate of electron heating, electron escaping, and electron isotropizing (due to collisions with neutral atoms) could have taken place and resulted in the electron isotropy. As the electron heating ceased, the parallel component hot electrons kept running away, which resulted in an anisotropic distribution at later time. It is believed that these escaping electrons will create a self-contained electric field to prevent other electrons from escaping [Torbert, 1987], since electrons cannot freely escape from the neutral cloud because of the electrostatic drags from the ions. The nominal escaping speed is about the ion acoustic speed [Singh, 1990]. If ambipolar diffusion occurred, the electric field is $\sim -(kT_e/q)(\delta n/n)$, with 10 eV electrons, $\delta n \sim n$, and the characteristic length scale of the inhomogeneity about 200 meters, this leads to a field aligned electric field of $\sim 50\ mV/m$, which is reasonably consistent with the z-component of the quasi-DC electric field measured by the Langmuir probes [Swenson et al., 1990].

One of the biggest controversies to the current CIV theory from the CRIT-II experiment is the electron heating mechanism. According to wave data shown in figure 3.12 [Swenson, 1992], the wave spectra observed during the passage of the barium beam were not associated with the lower hybrid instabilities. We believe that the observed heated electrons must be energized by the observed waves. Unfortunately,

the identity of waves observed in the active phase still remains unknown.

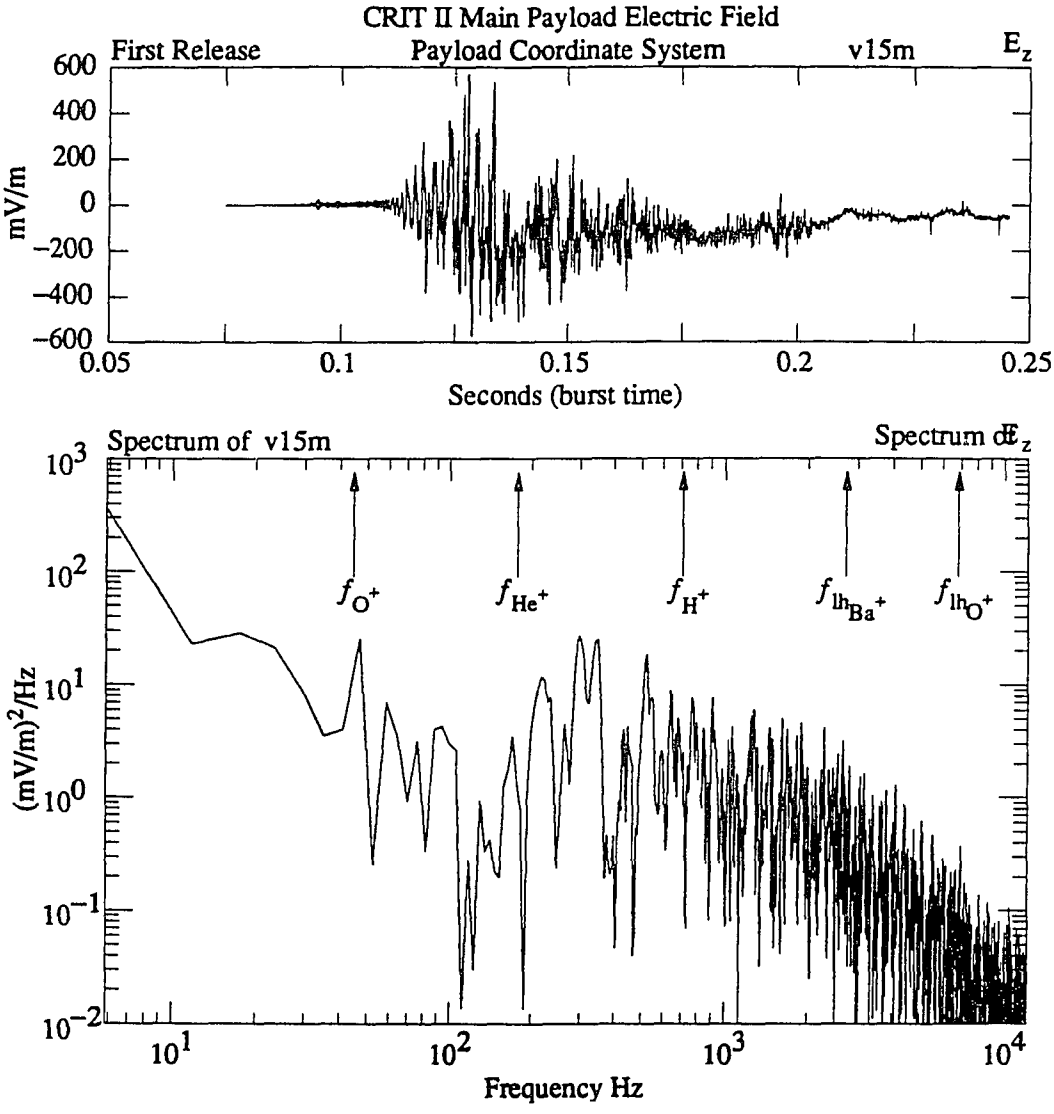

Figure 3.12: Electric field measurements in the first release (from Swenson, 1992).

3.3 CRIT-II Release Two

In the second release, the payload was configured nearly identical to the first release except for a longer release-payload distance (3.881 *km*), and a smaller injection angle

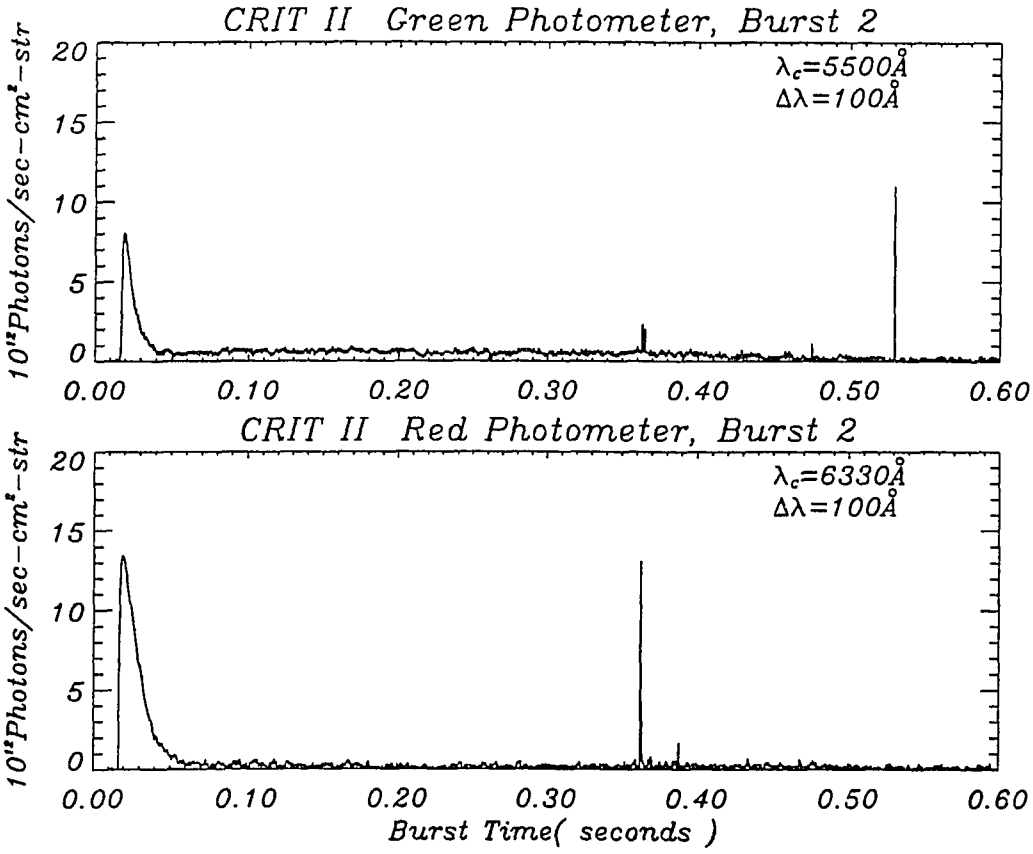

Figure 3.13: Brightness from the Green (top) and Red (bottom) Photometers during the second release of CRIT-II.

(45°) to the local magnetic field. Although ACS errors still existed, the direct view angle of the photometers to the release point was restricted to 8°. The output from both photometers is shown in figure 3.13 Again, a time delay due to the detonation of the chemical canister was observed at $\sim$ 17 *ms*. For some unknown reasons, it was 5 *ms* longer than that in burst one. This time delay sets the actual barium release time at 17 *ms* of the burst time or 404.826 seconds of the flight time. A big detonation flash seen by both photometers, as was expected, was over twice the magnitude as in burst one. On the contrary, after detonation, the brightness of the barium resonant line remained constant at a value of near 1×10^{11} $photons/cm^2 sec\ str$, but

it decreased gradually after the dense barium passed over the payload. This suggests that the "Green" barium line is created by electron collisions. There was a "flash", but of much smaller duration, seen by both photometers, roughly corresponding to the time when the dense barium beam arrived at the payload. The brightness of the "red" oxygen line was low but is consistent with the first release.

3.3.1 Ion ESA

The ion ESA output for the second release is shown in figure 3.14. The energetic ions were first seen at ~ 0.261 seconds of the burst time, with the separated distance of 3.881 km. This gives a velocity of $\sim 16 km/s$ or an energy of $\sim 180\ eV$ for the barium. This is in complete agreement with the measurements shown in figure 3.14. It further confirms that a super fast barium population did exist and the ground optical measurement [Wescott et al., 1990] could not detect this part of the barium ions. These early arrived barium ions showed 30° off the beam direction. It should be noted that there was no channel located at the beam direction to measure the direct beam ion. The nearest one, 4CD, was located at just about 30° to the right of the beam direction on the detector plane. The next channel 5AB was located at $\sim 30°$ to the left of the beam on the detector plane, and did not see any ion during that time because the Lorentz force tends to bend the ion trajectory to the right. Owing to a lower barium density and a larger scale length, fewer oxygen ions were seen by the ion detector as one would expect.

A series ion ESA data outputs are shown in figure 3.15 and figure 3.16 from 0.314 to 0.346 seconds of burst time. In the first plot, the main barium ions were first seen by the ion detector at the payload and the ions differential energy flux increased with time. Interestingly, the magnitude of ion flux was comparable to that in the first

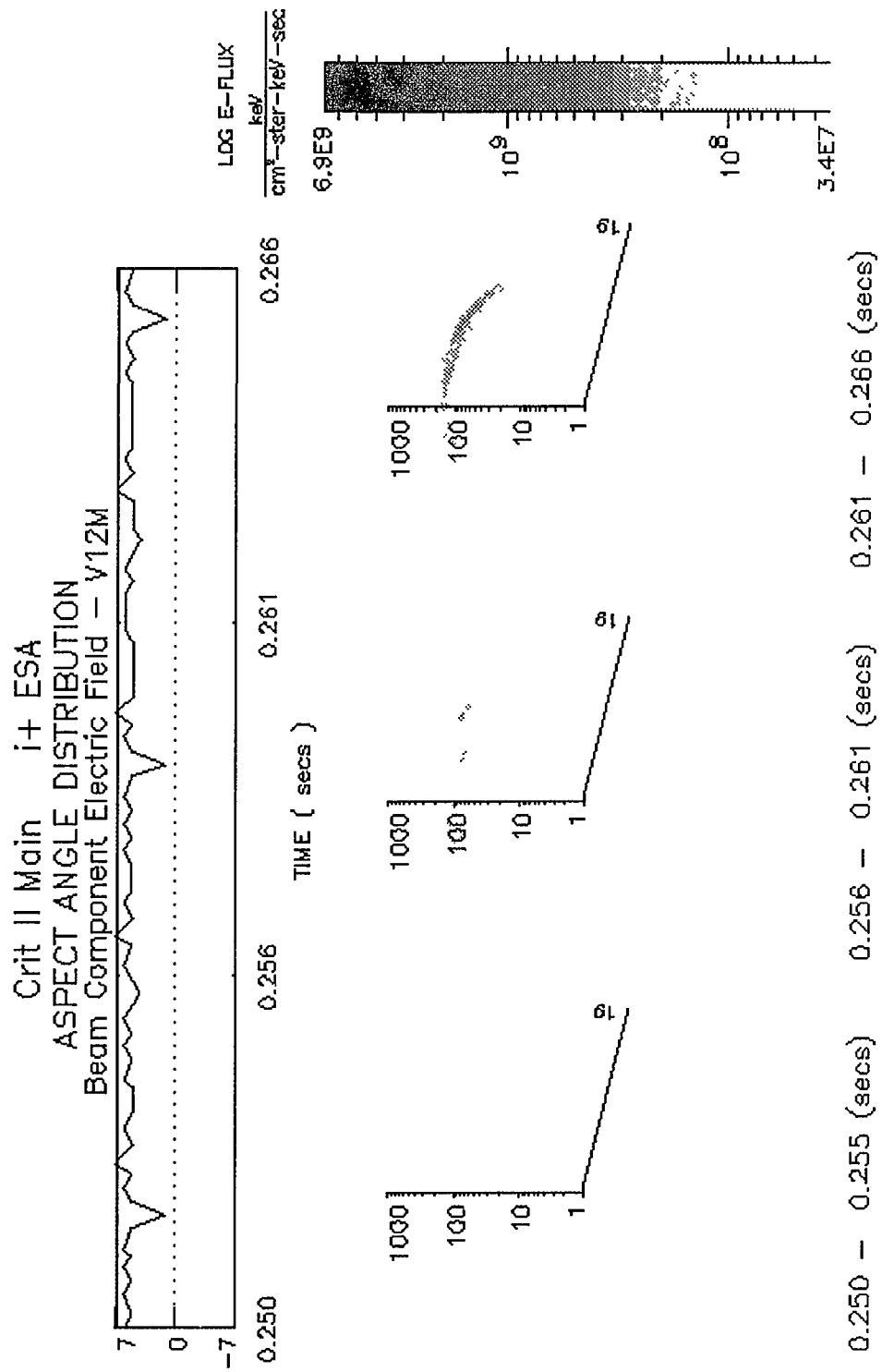

Figure 3.14: Ion differential energy flux in the second release. The ambient magnetic field is approximately pointing out from the paper.

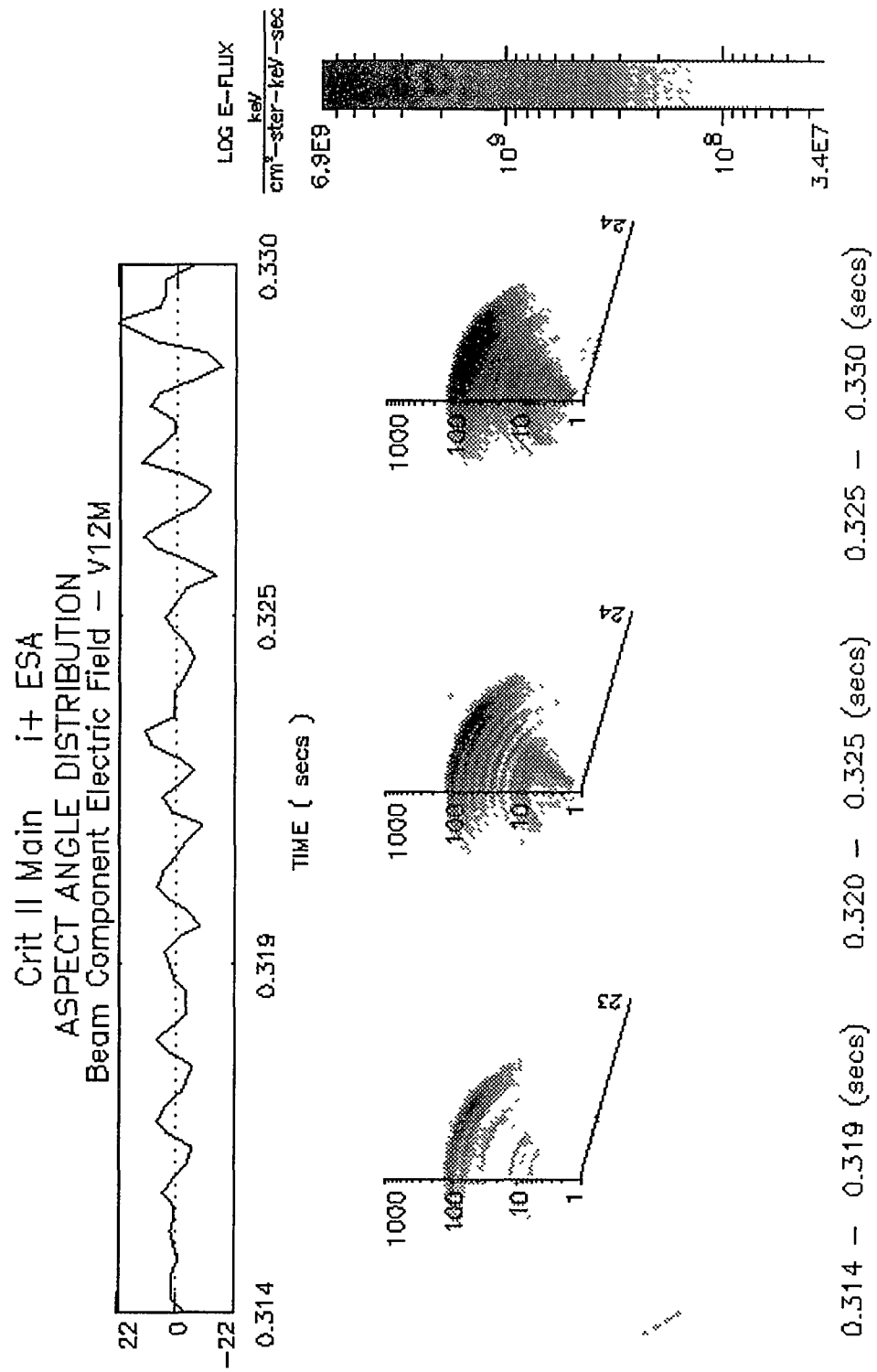

Figure 3.15: Ion differential energy flux in the second release. The ambient magnetic field is approximately pointing out from the paper.

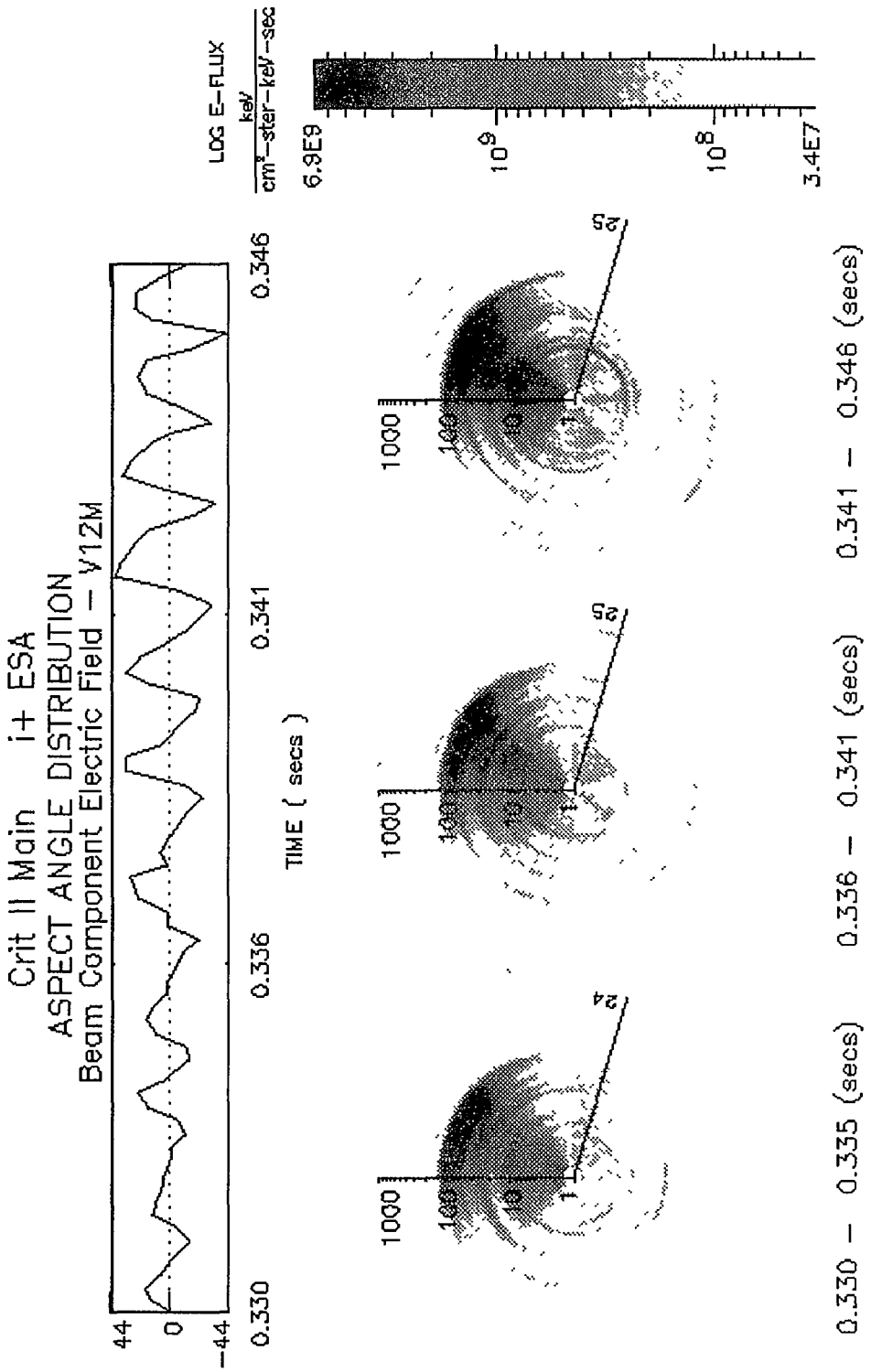

Figure 3.16: Ion differential energy flux in the second release. The ambient magnetic field is approximately pointing out from the paper.

release. Since the neutral barium density was lower in the second release than in the first release (approximately one order of magnitude, see figure 3.4), this implies that the ionization could have been more efficient at a larger distance from the release. From these series plots, one can also see that the energy of the energetic ion decays quickly from 120 eV all the way down to the lower limit of the ion detector in just 30 ms. It would be very interesting to see what kind of the beam-plasma interaction may have been involved during this time. Unfortunately, the wave data has not been fully analyzed by Cornell University at this time. From the electric field V12M raw data, which measures the electric field along the beam direction, on the top panel in figure 3.15 and figure 3.16, a clear, regular wave structure can be identified. This wave frequency is about 1000 Hz, again, not the oxygen lower hybrid waves predicted by the CIV theory. Coincidently, it is about the same wave frequency observed in the first release during the same corresponding period.

The time-energy spectrogram of channel 4CD, the closest one to the beam direction, is shown in figure 3.17. This channel had $\sim 30°$ aspect angle and $\sim 133°$ pitch angle. One can see that a band of slow energy decay followed the neutral barium time-energy dispersion curve shown in figure 3.2 and it stopped at 0.5 seconds of burst time. Although the barium energy was still relative high (above 30 eV) and the heated electrons lasted till 0.6 seconds of the burst time, no further ionization occurred after 0.5 seconds. We conclude that this is because the neutral barium density was too low (see figure 3.3) to produce observable ions. Similarly in burst one, a band of fast ion which decayed in a faster rate was also observed. We believe that this is an operative CIV effect.

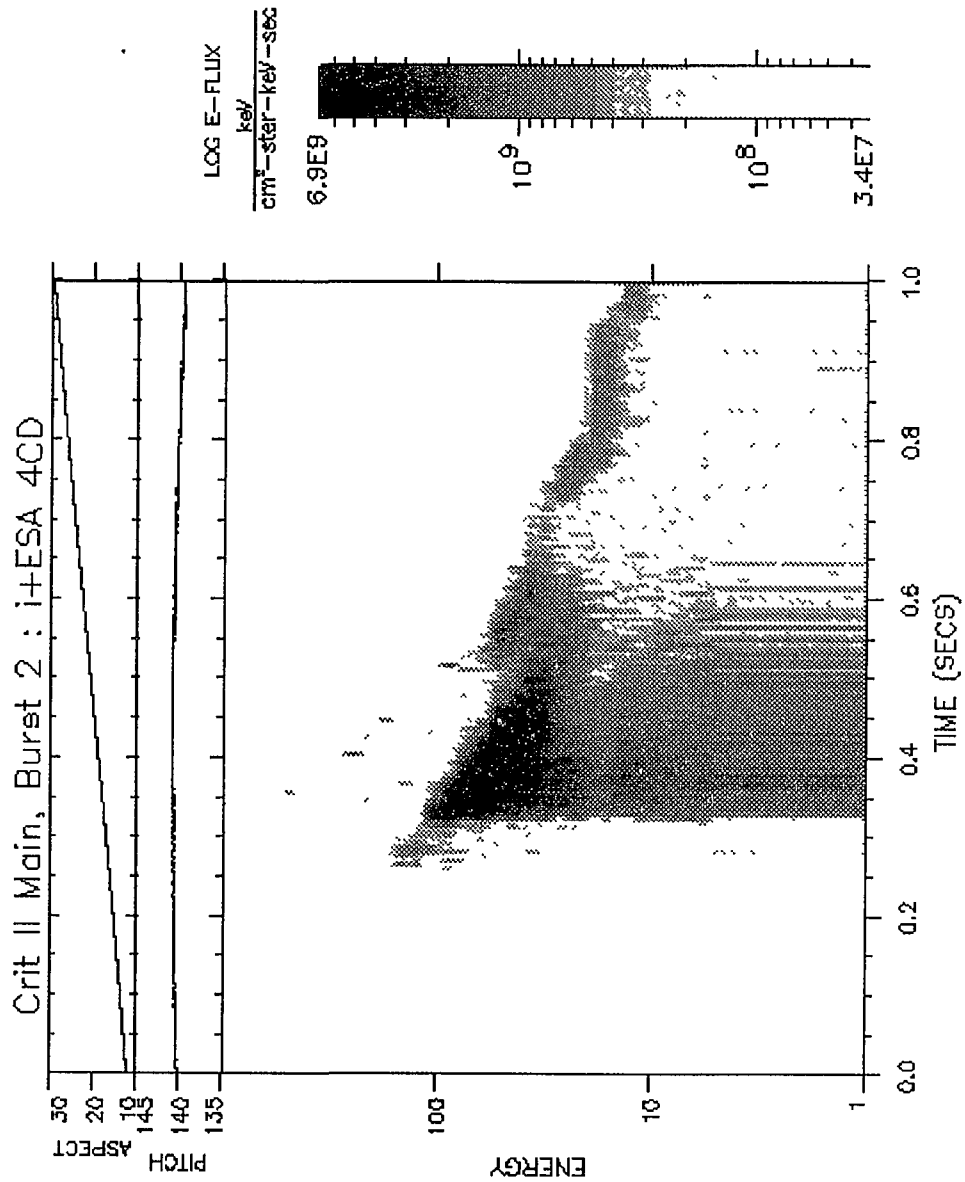

Figure 3.17: Ion differential energy flux of channel 4CD in the second release.

3.3.2 Electron CPA

The outputs from the electron CPA detector for the second release were surprisingly similar to the burst one. Two channels, CPA04 and CPA08, which represent the near 0° and 180° of pitch angles, respectively, are shown in figure 3.18 and figure 3.19. In both figures, the electron differential energy flux peaks at $\sim 6 \times 10^{10}$ $keV/cm^2 sec\ str\ keV$. A similar structure of the electron tail with energies centered at 10 eV was also observed. The preheated electrons were also observed as early as 0.2 seconds. However, the significant amount of hot electrons occurred starting at $\sim$ 0.26 seconds, the same time at which the fastest ions were observed by the ion ESA detector (see figure 3.14). The electron flux of near 0° pitch angle shows slightly more than that in 180° pitch angle. Interestingly, the electron anisotropy seen in the first release was not very obvious (both ended at 0.65s).

3.4 Data Analysis

3.4.1 Photometers

In Burst one, the "Green" surface brightness of 1×10^{12} $photons/cm^2 sec\ str$ was observed just before the big "flash". If the barium 5535 Å line was mainly produced by the electron impact excitation, then this surface brightness can be calculated from a line integral of the volume emissivity ϵ, assuming that the cloud is optically thin,

$$I = \frac{1}{4\pi} \int \epsilon dl = \frac{1}{4\pi} \int n_{ba} J_e \sigma_{res} d\Omega dE dl \tag{3.3}$$

where n_{ba} is the neutral barium density, J_e is the electron differential flux, and σ_{res} is the resonance cross section of barium 5535 Å line. A high limit for the hot electrons can be estimated by using the slow increase of surface brightness observed in the

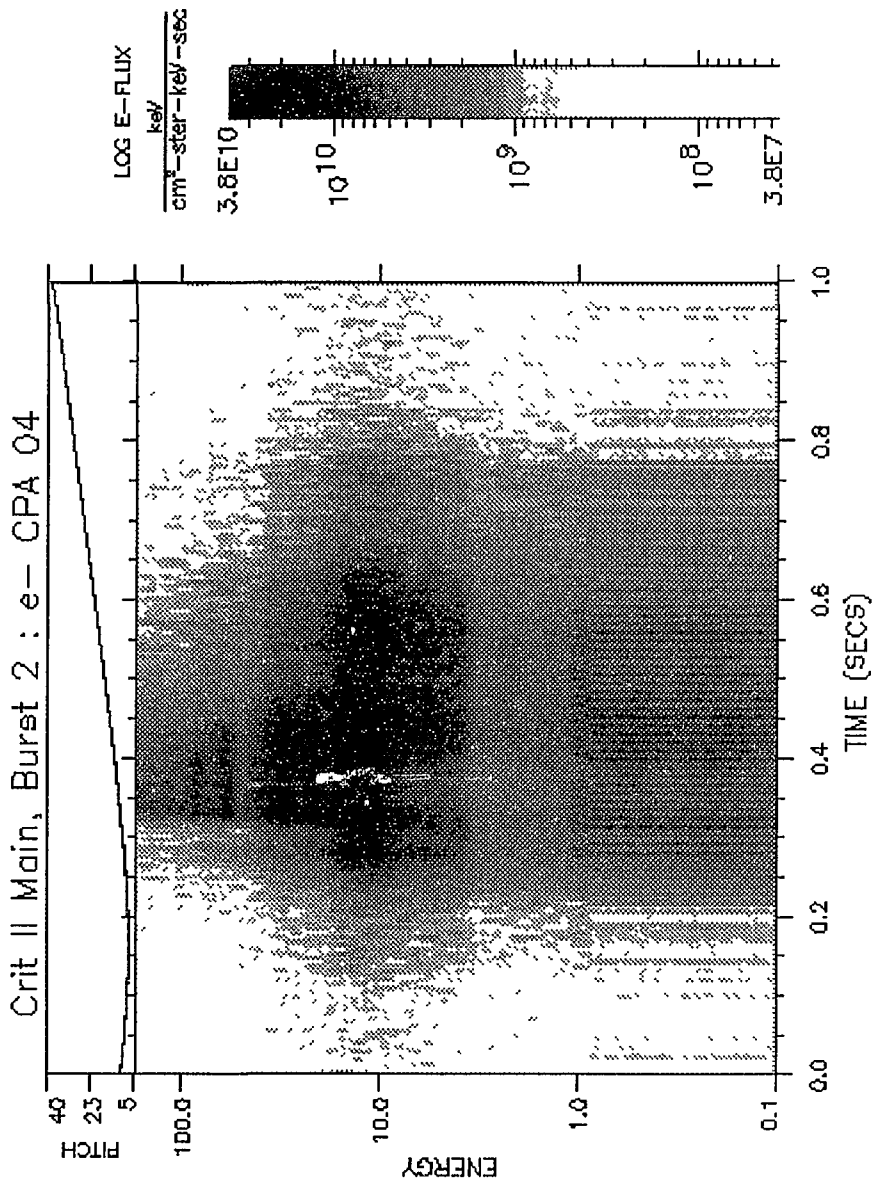

Figure 3.18: Electron differential energy flux of channel CPA04 in the second release.

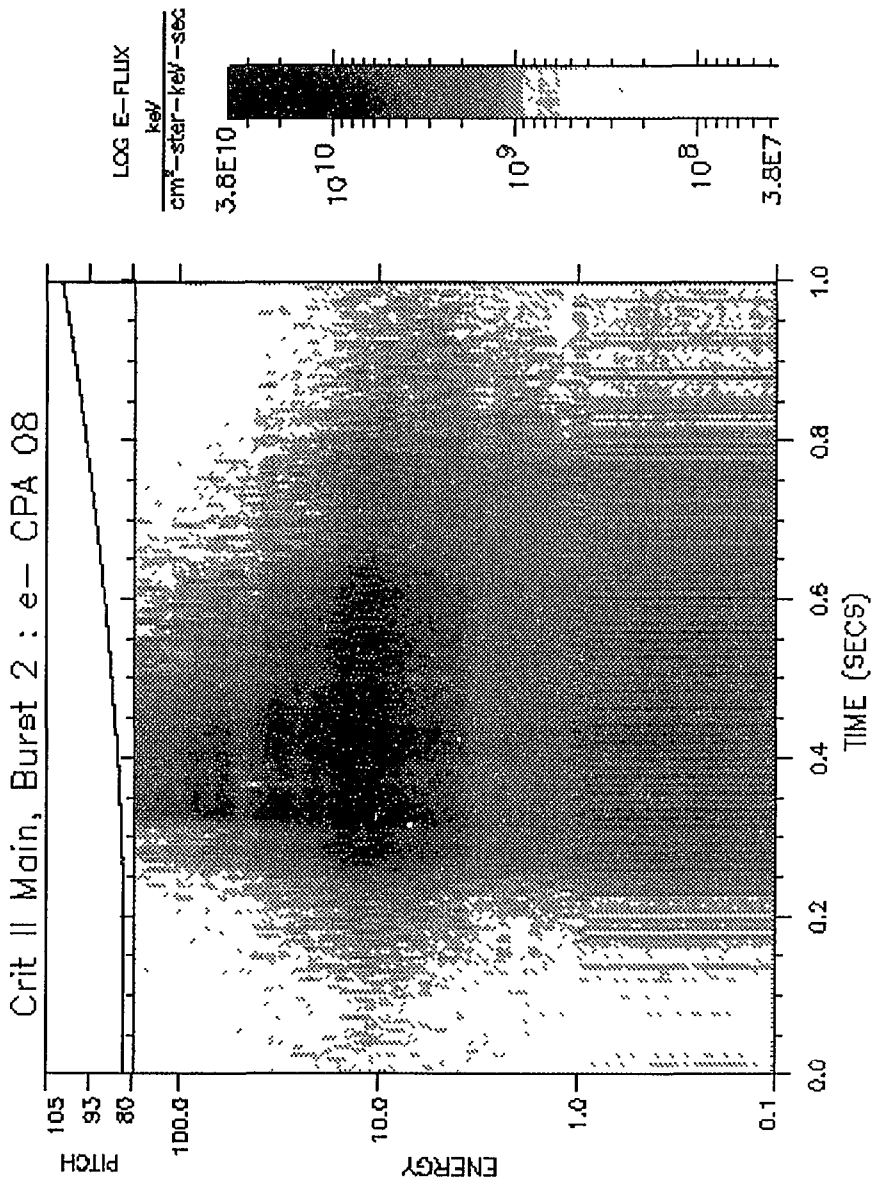

Figure 3.19: Electron differential energy flux of channel CPA08 in the second release.

first release. With a typical value of barium density $n_{ba} \sim 5 \times 10^9/cm^3$ (see figure 3.2) along the line and $\sigma_{res} \sim 5 \times 10^{-15}\ cm^2$ [Chen and Gallagher, 1976], we find that $J_e \leq 4 \times 10^{13}\ /cm^2 sec\ str\ keV$. This value is much larger than the observed electron flux by an order of magnitude. It suggests that the closer to the release point, the higher the electron flux.

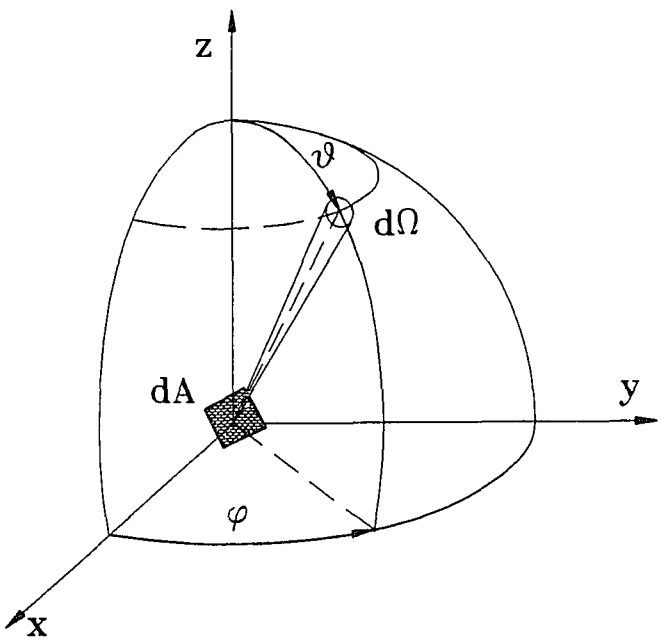

Figure 3.20: Definition of the differential directional intensity.

3.4.2 Particle Detectors

Usually, experiments are designed to measure the differential energy flux of the particles. This is defined as a function $J(x, y, z, E, \theta, \phi, t)$ such that $JdAd\Omega dEdt$ represents the number of particles with energy between E and dE which, during the time dt, traverse to the element of area dA in a direction within the element of solid angle $d\Omega$ around the normal to dA. The space coordinates (x, y, z) specify

the position of dA, and the angular coordinate θ and ϕ specify the direction of the normal to dA (see figure 3.20).

Before analyzing data, it is used to first convert the electron differential energy flux, J, to the conventional electron distribution function, f. The differential energy flux is related to the distribution by a simple equation. To obtain this equation, consider that the particles whose direction of motion lies within the solid angle $d\Omega$ and whose energy lies within the energy interval dE occupy in velocity space a volume equal to $v^2 dv d\Omega$, where v is the magnitude of the velocity corresponding to the energy E. Consider also that the particles, during the time dt, which traverse the area dA perpendicular to their direction of motion, at the time t, occupy a volume of configuration space $v dA dt$, where v is the speed of the particles. It follows from conservation of particles that

$$J dA d\Omega dE dt = f dA v^2 dv d\Omega v dt \tag{3.4}$$

The relation between J and f can be obtained by substituting $dE = mvdv$, for non-relativistic particle, this yields

$$f = \frac{m}{v^2} J = \frac{m^2}{2E} J \tag{3.5}$$

Thus, a measurement of the differential energy flux J is equivalent to a measurement of the distribution function f.

3.4.3 Density of the Energetic Ion Beam

The density of energetic ions can be obtained from equation (3.5) by integrating f over the velocity space, *i.e.*

$$n_i = \int_E \int_\Omega \frac{J_i}{v} d\Omega dE \tag{3.6}$$

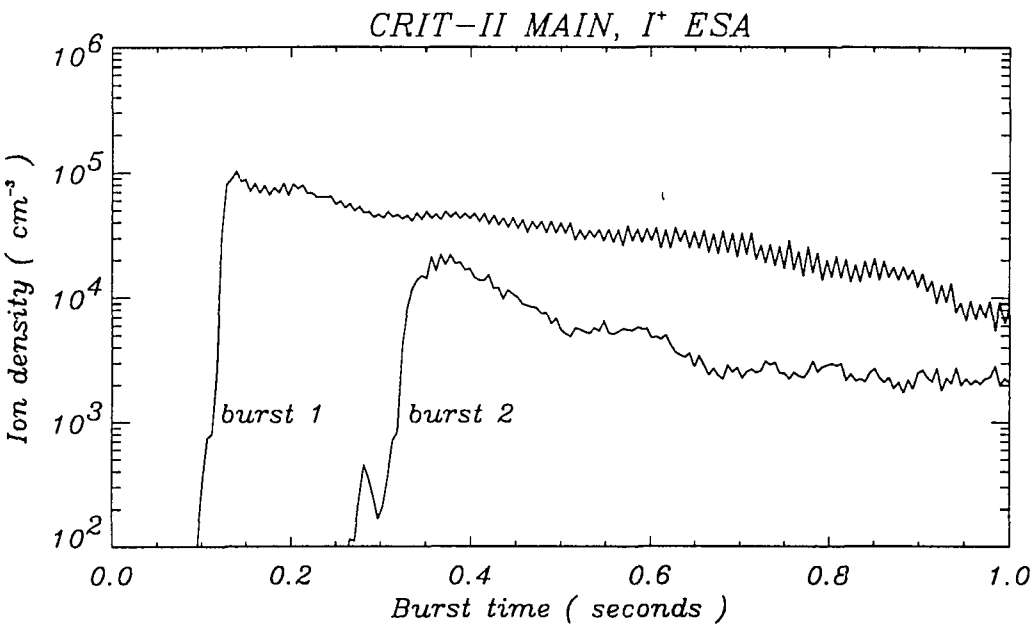

Figure 3.21: Non-thermal ion beam density measured by ESA in the first and second release.

To evaluate this integral, one needs all components of J_i. However, the ion ESA detector measures fluxes only in a plane. Since each channel had a 20° field of view angle, we use $\Delta\Omega = 0.38$ steradian to substitute for the solid angle integration in equation 3.6. After performing the energy integration, assuming isotropy, the ion beam density measured by the ion ESA in the two releases is shown in figure 3.21. It should be noted that since the ion ESA detector does not provide mass resolution, we have assumed barium for the mass of the ions in figure 3.21. This assumption is reasonable since data from several ion channels of the ESA show flux variations at the barium ion gyrofrequency in those energy ranges that contribute most to the density. We do know whether some of the lower energy ions are oxygen since oxygen gyrofrequencies are occasionally seen there. However, the density shown in figure 3.21, using barium, peaks at $10^5\ cm^{-3}$ for the first release and $2 \times 10^4\ cm^{-3}$

for the second release, and these numbers are relatively consistent with the RF plasma probe's measurements [Swenson et al., 1990] (see figure 3.22). On the other hand, if these ions were oxygen, the density would be multiplied by a factor of $\sqrt{M_o/M_{ba}} = 0.34$.

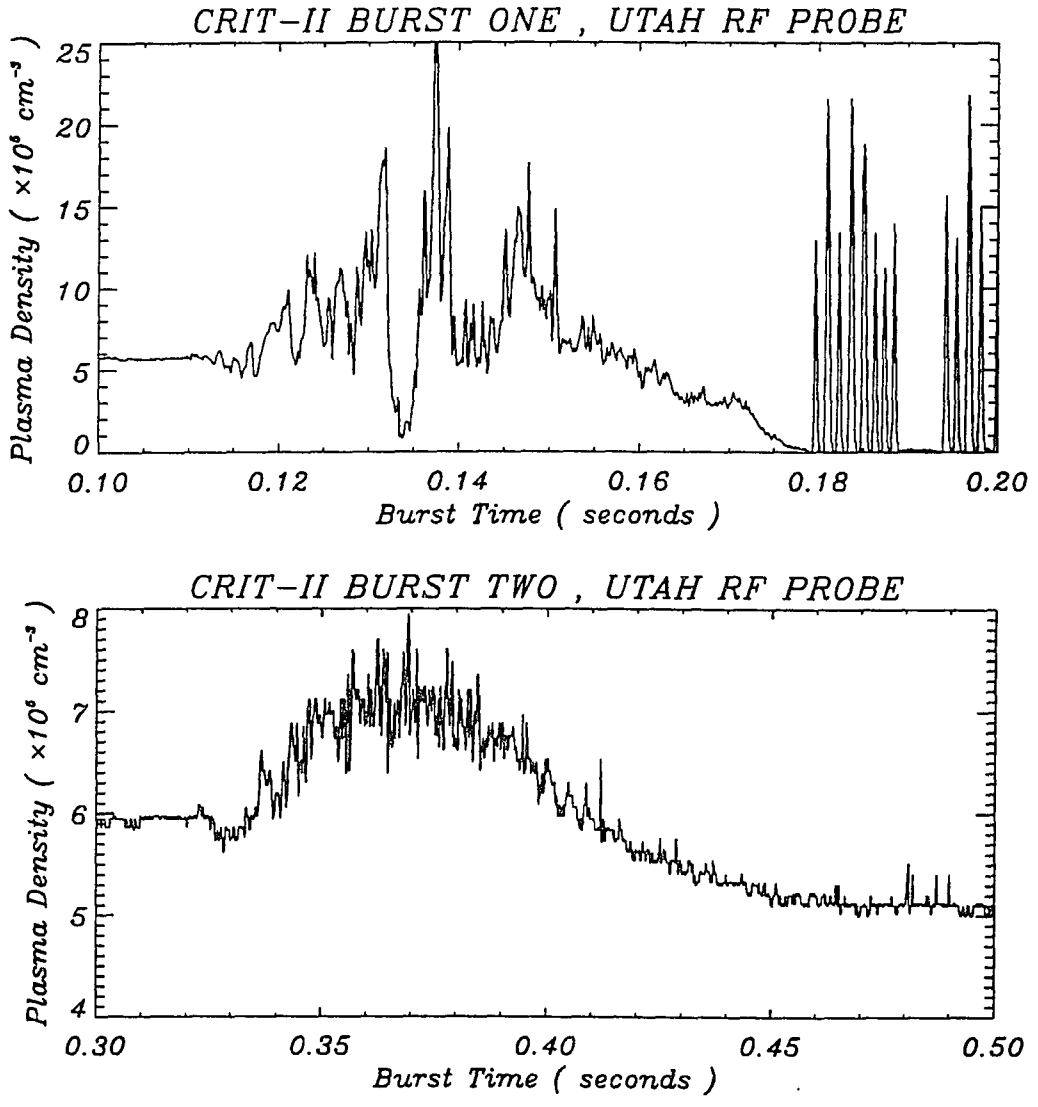

Figure 3.22: Plasma density measured by Plasma Frequency Probe in the first (top) and second (bottom) release.

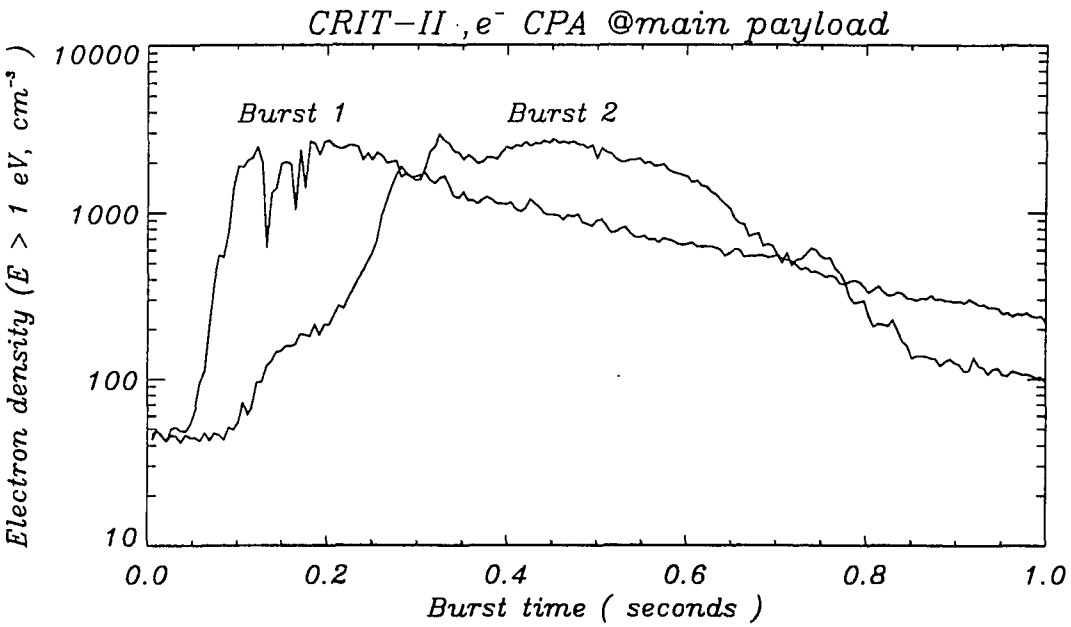

Figure 3.23: Hot electron density measured by CPA for the two releases.

3.4.4 Density of Hot Electrons

The calculation of the hot electron density, however, is straight forward by applying equation (3.5) to the six-dimensional phase space integration. It is reasonable to assume that the electrons are gyrotropic, thus the density can be obtained by integrating (3.5) over pitch angle and energy, *i.e.*

$$n_e = \sqrt{\frac{m}{2}} \int_E \int_\Omega \frac{J_e(\theta, E)}{\sqrt{E}} d\Omega dE \tag{3.7}$$

where θ is the pitch angle. The integration result from equation (3.7) is shown in figure 3.23. It's clear to see that the maximum density of hot electrons in both releases is eventually identical (at a value of 2×10^3 $cm{-}3$). However, we know that the electron CPA is saturated in the first release. Taking this into account, the maximum hot electron density could be as high as 10^4 cm^{-3}.

3.4.5 Barium Production Rate

It is interesting to see if the hot electrons observed by the CPA detector are responsible for the nonthermal ions observed by the ion ESA detector. If barium neutrals are mainly ionized by electron impact collision, then the local barium production rate can be calculated by

$$\dot{n}_{ba^+} = n_{ba}(r,t) \int f_e \sigma_{ion}(E) v d^3v \qquad (3.8)$$

where n_{ba} is the neutral barium density given by figure 3.3, and σ_{ion} is the barium electron impact ionization cross section. This cross-section has been measured by Vainshtein *et al.* [1972]. The calculation results for two releases are shown in figure 3.24 as solid lines. The peak barium production rate is about 5×10^5 $cm^{-3}sec^{-1}$ for the first release and 6×10^4 $cm^{-3}sec^{-1}$ for the second release. Actually, taking the saturation of the CPA detector into account, the peak barium production rate could be over 1×10^6 $cm^{-3}sec^{-1}$ for the first release. This, however, is not easy to compare with the ion density observed by the ion ESA detector. For a first order approximation, the convective ions can be ignored. We can multiply the ion production rate by a characteristic time to obtain the barium density. This characteristic time, Δt, is determined by the time over which the main barium cloud passes through the payload. Taking, say, 13.5 km/sec as the velocity of the leading edge cloud, and 6.1 km/sec, corresponding to $v_\perp = v_{crit} = 3.3 km/sec$), trailing edge for the first release one obtain $\Delta t = 0.145$ seconds. This gives an average ion density value of more than 7×10^4 cm^{-3} which is consistent with the ion density in figure 3.21. Likewise, a characteristic time of 0.54 seconds can be found for the second release. This gives an estimated ion density of 3.2×10^4 cm^{-3} which certainly

agrees with the ion density in figure 3.21.

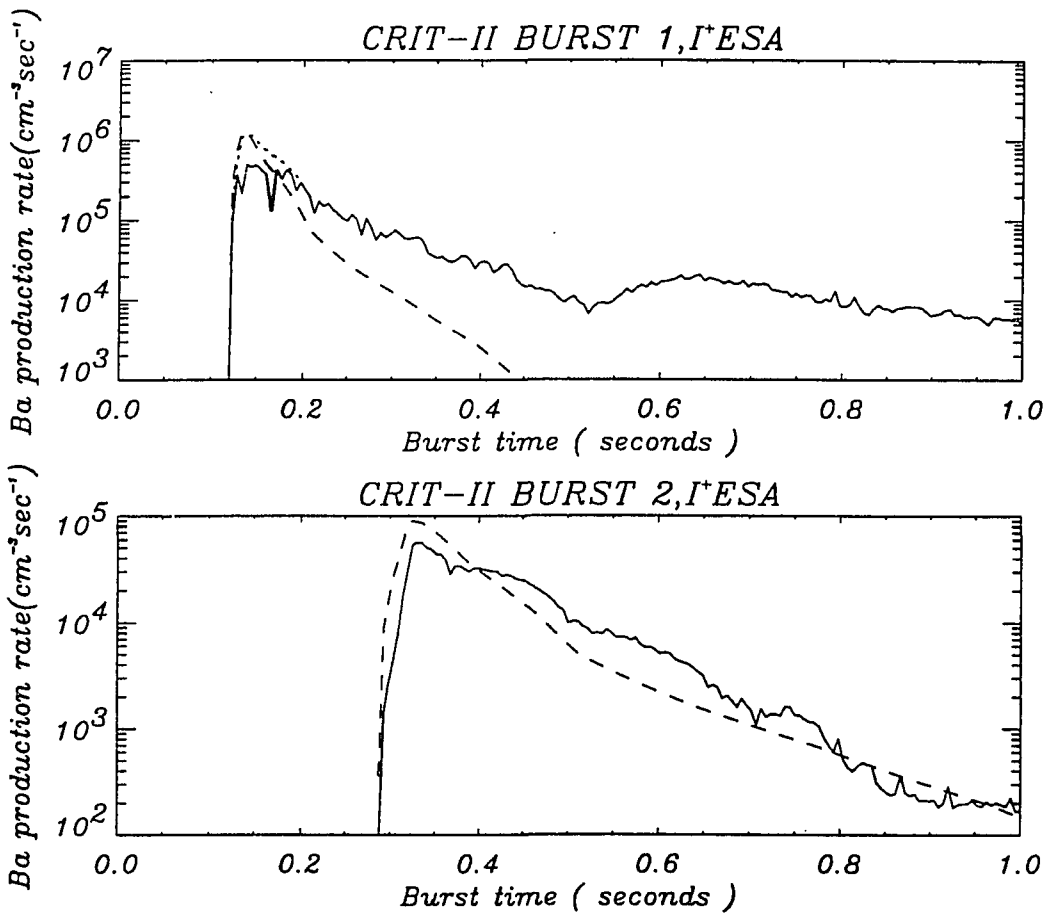

Figure 3.24: Barium ion production rate due to electron impact ionization (solid line) and charge exchange ionization (dashed line) for burst one (top) and burst two (bottom). The dotted line (top figure only) is the estimate electron impact production rate without saturation.

3.4.6 Hot Electron Temperature

The hot electron temperature is also calculated by integrating the normalized hot electron distribution function with $1/2mv_e^2$. The results are shown in figure 3.25.

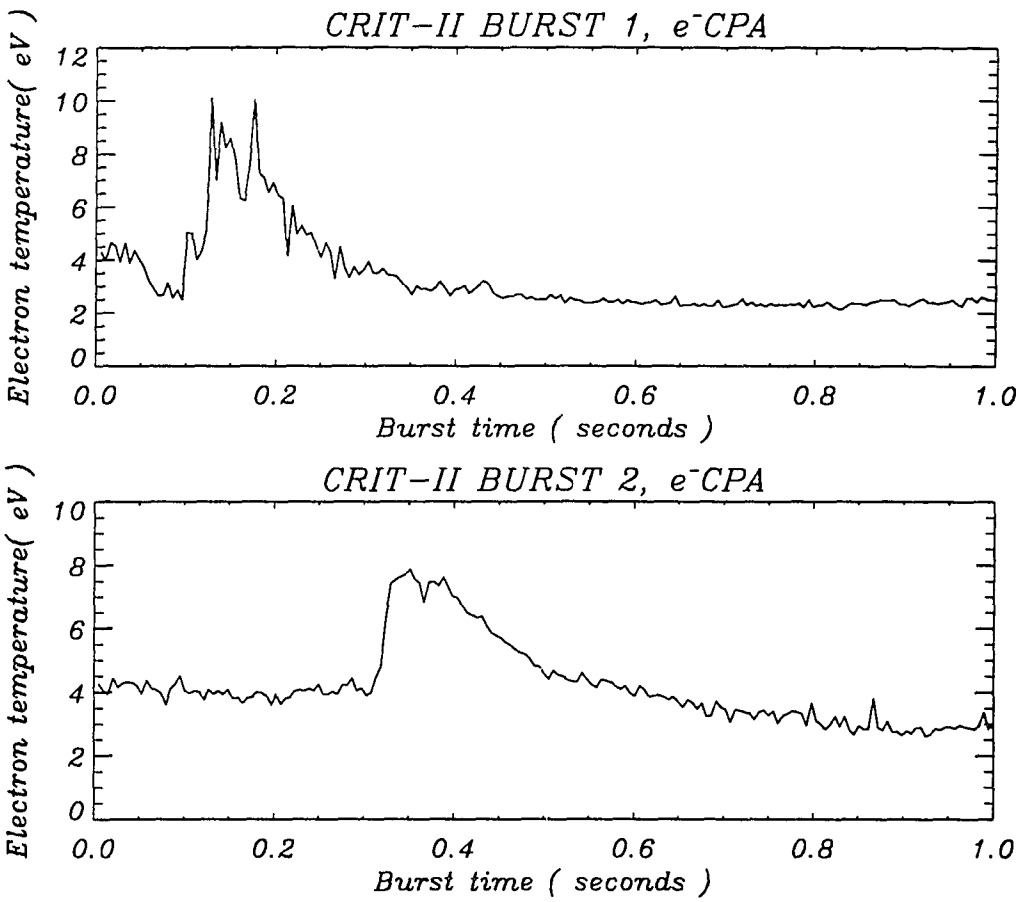

Figure 3.25: Hot electron temperature for two releases.

One might be aware that the background electron temperature seems too high and this could be because the density of the electrons is too small to have any statistical significance. In the active region, the electron temperature peaks at 10 eV for the release one and 8 eV for the release two. This hot electron population composes a high energy tail of the distribution as predicted by the quasilinear theory of lower hybrid instabilities. However, the lower hybrid waves were not observed during this period.

To briefly summarize this chapter, the essential features of critical ionization

velocity effect such as rapid ionization of neutral barium, wave-particle interactions, and the formation of the hot electron tail, are believed to be observed in the CRIT-II experiment. It seems that the CIV effect is more likely to happen in the region where the ambient plasma density is high. However, the ionization yield is not expected to be as high as that in Porcupine. Although the precursor ion accompanied by the lower hybrid waves were measured, the wave spectrum during the passage of the main streaming barium beam is not consistent with the current CIV theory and is probably the main reason that led to a lower level of ionization process.

CHAPTER 4

Barium Ion Production

4.1 Introduction

The CRIT-II was instrumented with ion and electron particle detectors. By using the electron data, one can quantitatively calculate the barium production rate due to electron impact ionization collisions, given the neutral barium distribution and electron impact cross section. By subtracting the density calculated above from the ion density measured by ion detector, that part of barium ions, which is created by non-CIV ionization processes, is obtained. This is the main subject of this chapter. Also, we will discuss the possible major non-CIV ionization mechanisms in CRIT-II such as charge exchange, charge stripping, and associated ionization.

4.2 Barium Ion Density Model

In order to better evaluate the observations a computer program has been developed to simulate the observed ion density by using available measurements. The observed ion density and barium electron impact production rate has been calculated in the previous chapter. Now, we must convert this production rate to a density seen at the payload. This barium ion density model is based on Liouville's theorem which states that the particle distribution function is conserved along its trajectory in

phase space. To trace the trajectory of the barium ions, the equation of motion of charged particles in the electric and the magnetic fields will be solved. The earth's magnetic field, $B_0 = 0.43$ gauss, is assumed to be constant. The electric fields are taken from the actual measured data [Swenson et al., 1990], but only the quasi-DC electric fields ($\omega < \Omega_{o+}$) will be considered in our model calculation.

The barium ions are created from the ionization of neutral barium. However, there can be several ionization mechanisms: for example electron impact ionization, charge exchange, charge stripping, and associated ionization. The stripping cross section of neutral barium against the ionospheric oxygen ions is estimated to range from 1×10^{-19} cm^2 [Swenson et al., 1991] to 9×10^{-18} cm^2 [Brenning et al., 1991a] and is much smaller than the charge exchange cross section by at least two orders of magnitude. Therefore, it is not very likely to compete against the real CIV ionization process over all except near the release point where the density of neutral barium is very high. The associated ionization cross section pointed out by Lai *et al.* [1992] could be very high. By our knowledge, however, it is important only when the velocity is far below the velocity range at which the space CIV is conducted. Therefore, we will also ignore the associated ionization to simplify our model. The first theoretical estimation for the cross-section of $Ba - O^+$ was, in order of magnitude, found to be 1×10^{-16} cm^2 [Axnäs and Brenning, 1990] which is too small to affect real CIV process, at least in the case of CRIT-II. However, a controversial argument suggested by Swenson *et al.* [1990] gave a high charge exchange cross section of $\sim 1 \times 10^{-14}$ cm^2. They suggested that this high cross-section is due to a particular reaction, namely

$$O^+(^4S_{3/2}) + Ba(6S_2,^1 S_0) \text{—>} O(^3P_2) + Ba^+(6g,^2 G_{7/2}) + 0.078 \text{ eV} \text{ —— (a)}$$

which is exothermic by 0.078 eV. This small energy defect can cause a near resonant charge exchange; thus, a high charge exchange rate could be expected. They also claimed this is probably overwhelming the CRIT-II CIV experiment [Stenbaek-Nielsen et al., 1990b].

However, they did not actually calculate the charge exchange cross section of $Ba - O^+$ but only analogously compared the reaction (a) to a similar experimental result of charge exchange collisions [Rutherford et al., 1972b]

$$O^+(^4S_{3/2}) + Ca(^1S_0) \text{—>} O(^3P_2) + Ca^+(5P,^2 P_{1/2}) + 0.001 \text{ eV} \text{ —— (b)}$$

This reaction has a large cross section about 1.4×10^{-14} cm^2 at velocity of oxygen about 10 km/sec (measurement was made in the neutral Calcium frame) . However, the energy defect for the reaction (a) is 0.078 eV, a value much higher than that in the reaction (b). In our opinion, there is no reason to consider both reactions (a) and (b) to be alike. For this reason, a more rigorous calculation is needed to give a better cross section estimate for the $Ba - O^+$ charge exchange collision.

4.2.1 Calculation of Charge Exchange Cross Section

The method used for the calculation of the cross section is based on the theoretical consideration for resonant and nonresonant charge exchange processes developed by Rapp and Francis [1962]. This model used empirical wave functions to represent two asymptotic states, *i.e.*, initial and final states, and ignored all the detail of fine structure of atoms. The cross section is calculated by solving the transition

probability between the two asymptotic states. This model is best applied to the velocity ranges in which that most space CIV experiments can apply.

For resonant charge exchange, their model gives the following cross section as a function of relative velocity, v:

$$\sigma_{res}(v) = \frac{1}{2}\pi b^2 \tag{4.1}$$

where b, the effective radius, is found by solving the equality

$$\left[\left(\frac{2\pi b}{\gamma a_0}\right)^{1/2}\left(\frac{I}{\hbar v}\right) b\left(1+\frac{a_0}{\gamma b}\right) exp\left(-\frac{\gamma b}{a_0}\right)\right] = \frac{\pi}{6} \tag{4.2}$$

and I is the ionization potential of atoms, a_0 is the Bohr radius, $\hbar$ is Plank's constant, and $\gamma = (I/13.6)^{1/2}$.

$$\sigma_{nrs}(v) = \frac{1}{2} f \int_0^b sech^2\left[\left(\frac{\omega}{v}\right)\left(\frac{a_0\pi b'}{2\gamma}\right)^{1/2}\right] 2\pi b' db' \tag{4.3}$$

where b is determined by the root of following equation

$$sech^2\left[\left(\frac{\omega}{v}\right)\left(\frac{a_0\pi b}{2\gamma}\right)^{1/2}\right] = 4sin^2\left\{\frac{2Ib^2}{a_0\hbar v}\left[K_0(\gamma b/a_0) + \frac{K_1(\gamma b/a_0)}{(\gamma b/a_0)}\right]\right\} \tag{4.4}$$

in which, $\omega = \Delta E/\hbar$, ΔE is the energy defect of reactions, f is a statistical weight factor, and K_0 and K_1 are the second kind Bessel functions of zero and first order, respectively. The statistical weight f is a pre-exponential factor of the equilibrium constant for the reactions. It can be determined by the principle of symmetry as follows. Since the charge exchange collisions in the "intermediate" velocity range involve relatively large impact parameters, the electron spin should be conserved. In the reaction (b), for example, the reactant compound has five possible states for total spin of 3/2 ($m_s = \pm 3/2, \pm 1/2, 0$). The product compound has five states for total spin of 3/2 and three states for total spin of 1/2 ($m_s = \pm 1/2, 0$). Therefore only

collision complexes having a net resultant spin 3/2 can produce O atoms. One can see all five possible spin states can make forward charge exchange collision, but only five out of eight states can make backward charge exchange collision. Therefore the statistical weight factor, f, in charge exchange collision (b) is 1 for forward reaction and 2/3 for backward reaction. If an equilibrium state is reached, the equilibrium constant for the reaction (b) is thus 3/2.

The cross-sections for the two-state approximations, equation 4.1 and 4.3 above, have been calculated for several charge exchange reactions and are illustrated in figure 4.1. The charge exchange cross section is calculated as a function of the neutral atom velocity in the range of most space CIV experiments. The solid and broken lines represent the resonant and nonresonant charge exchange cross sections for different atom species, respectively. Some experimental and estimated data are also provided in this graph for comparison. The resonant curves match the well-known form $\sqrt{\sigma(v)} = -k_1 \ln v + k_2$, where σ is the cross section, k_1 and k_2 are constants. This formula has been used widely for extrapolating charge transfer data over velocity ranges. In general, at high velocities the nonresonant curves overlap with their corresponding resonant curve and the cross section increases with decreasing velocity until reaching a peak from which it decreases quickly at lower energies. This feature of the nonresonant charge exchange can be fully explained by "near-adiabatic theory " [Massey et al., 1970 1974]. According to this theory, as the interaction time is much greater than the time scale of electronic transition, i.e. $a/v \gg \hbar/\triangle E$, or the relative velocity of two interaction particles v is much less than $a\triangle E/\hbar$, where a is the length scale of the interaction range between ion and atom, the reaction process is so slow that the electrons will have enough time

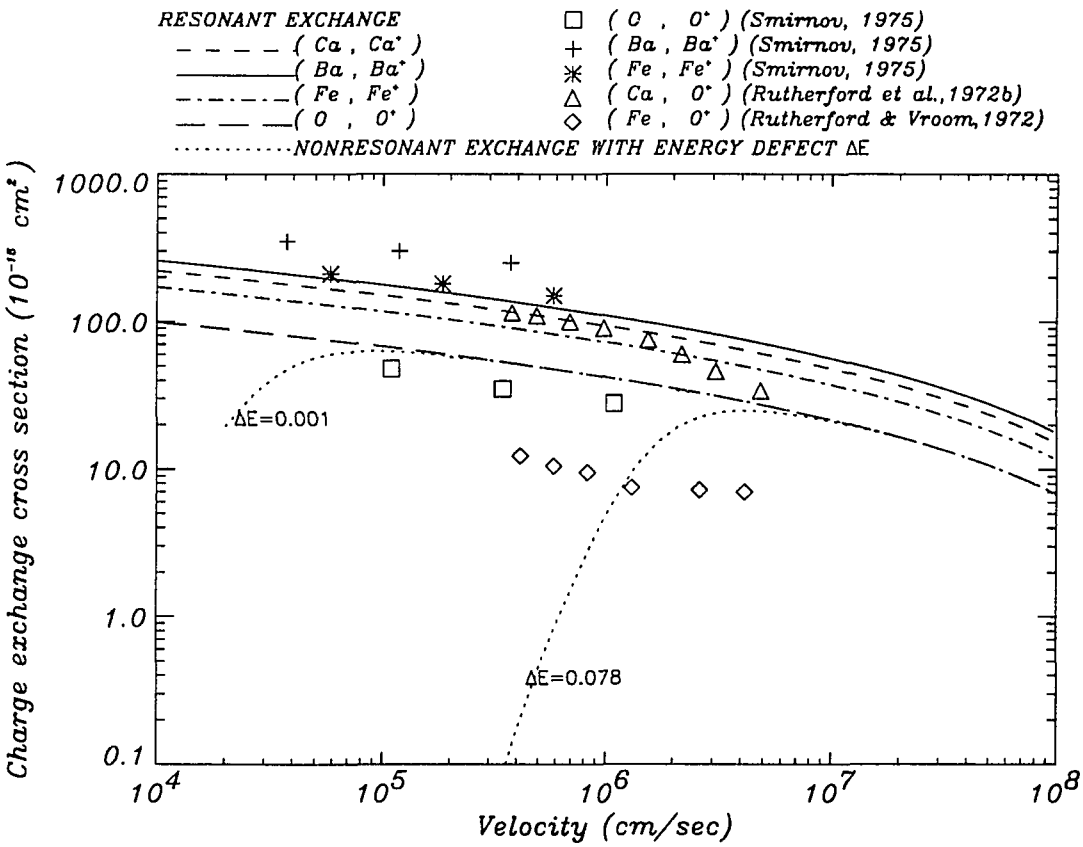

Figure 4.1: The charge exchange cross sections calculated based on the two state approximation. Some theoretical estimates adopted from Smirnov [1977] and experimental measurements from Rutherford *et al.* [1972] are also appended in this figure for comparison.

to readjust themselves to the perturbation induced by the interaction without an electronic transition occurring. In this case the collision will be nearly adiabatic and charge transfer cross section will be small. If the velocity is increased to an order of $a\triangle E/\hbar$, the collision is no longer adiabatic since the collision time scale has become comparable with the transition time scale, $\hbar/\triangle E$. At this point the cross section for charge transfer will reach its peak value. At higher velocities, the interaction time finally becomes too short for the transition to occur, and the cross section decreases

with increasing velocity.

Note that, in figure 4.1, the calculated charge-exchange cross section for $Ca - O^+$ with energy defect $\triangle E = 0.001$ peaks at $v \sim 10^5$ cm/sec at value about 7.0×10^{-15} cm^2 which is smaller than the cross-section measured by Rutherford *et al.* by a factor of two. We think this is a good match and the reason which may cause the underestimation of charge-exchange cross section could be realized that the measurements is actually taking total cross sections into account, unlike the two-state approximation which considers only the smallest energy defect as the most important electronic transition causing charge transfer. In other words, if all the possible transitions are included in our calculations, the difference between model and measurement results will be recovered. This high charge-exchange cross section for $Ca - O^+$ is explained by Rutherford *et al.* mainly due to the special reaction (b) leading to very close energy resonance.

By using the same argument of the conservation of spin, it is found that the statistical weight factor, f, is 1 for the reaction (a). The calculated result is also plotted in figure 4.1. It is worthy to point out that this cross-section has a maximum around $v \sim 30$ km/sec. For velocity of the neutral atoms below 20 km/sec, the cross section decreases rapidly with decreasing velocity, and most of the space CIV experiments were conducted at this velocity range.

4.2.2 Density Model Calculation

According to above calculations and discussions, the barium ion production rate, Q, is thus given by summing of the electron impact ionization and the charge exchange

ionization processes, *i.e.*

$$Q(x,t) = n_{ba}(x,t) < n_e v \sigma_{ion}(v) > + n_{ba}(x,t) n_{o^+} v_{ba} \sigma_{exc}(v) \qquad (4.5)$$

where the subscripts "ba","e", and "o^+" stand for their usual means. The background oxygen ion density, $n_{o^+} = 5.41 \times 10^5\ cm^{-3}$, is taken from the plasma density measured by the on board RF plasma probe [Swenson et al., 1990] and the charge exchange cross section, σ_{exc}, is given by theoretical calculation result obtained in previous section with a multiplicative factor, α. This α factor is used as a scaling factor to adjust the value of charge exchange cross section in order to match our model results with observed data. Barium ion production rates due to $Ba - O^+$ charge exchange for $\alpha = 1$ are plotted as broken lines in figure 3.24, one can see that two ionization mechanisms could be comparable if $\alpha = 1$.

The barium production rate needs to be given at any location inside the beam at any specified time in our model calculation. Owing to the CRIT-II measurements were made at a fixed point only during each release, we assume that two releases can be considered as one experiment but with two point measurements. Therefore, electron flux at place other than the measurement points will be obtained by interpolation and extrapolation methods from two release data. Likewise, the DC-electric fields will be treated by the same way as well. Also, an estimate electron flux assuming no saturation will be used in our calculation (see the dotted line in figure 3.24).

The model computation is carried out by following procedures: we first divide a conical shape of computational domain into several pieces of small volume elements. The number of newly created barium ions in each volume element at time, say, $t = t_0$, then is calculated, with an assumption of step-wise ionization, by multiplying

equation 4.5 by the time step, Δt, and the corresponding element volume. We further assume all the particles in the same volume element are characterized by a single particle element which marches out from the center point of volume element as soon as they are created. This single particle trajectory is numerically calculated by Newton's second law, given the observed electric field and the Earth's magnetic field as well as the proper initial conditions, *i.e.* the coordinate of the center of the volume element and the neutral barium velocity at that point. Once a particle element reaches and enters a box which is centered at the location of payload, it will be counted and its coordinate and time will also be recorded. This particle tracing technique will be proceeded for each of every volume element at each time step until a preset maximum time (one second) is reached. This whole procedure then is repeated for the next time sequence, $t = t_0 + \Delta t$, until one full second. In our calculation, the time step, Δt, is taken to be 5 ms to match a complete energy sweeping time of the detector. A smaller time step of 1 ms is used to compute the particle's trajectories. Finally, the density of the barium ions which may represent the density at payload location is obtained by averaging the number of particles over the whole box and over the time interval of 5 ms.

Before making comparison of the model densities to the observed densities, one needs to point out that a fraction of ions, at energy range below 10 or 20 eV, observed by the ESA detector is oxygen [Torbert et al., 1992]. Also, note that the neutral barium energy falls below 20 eV at 0.3 seconds in the first release and 0.7 second in the second release. Therefore, only comparisons within these time period would be reasonable. However, the choice of the cut-off energy for barium ion density is not obvious, we will show two ion density curves, one for 10 eV and one for 20 eV,

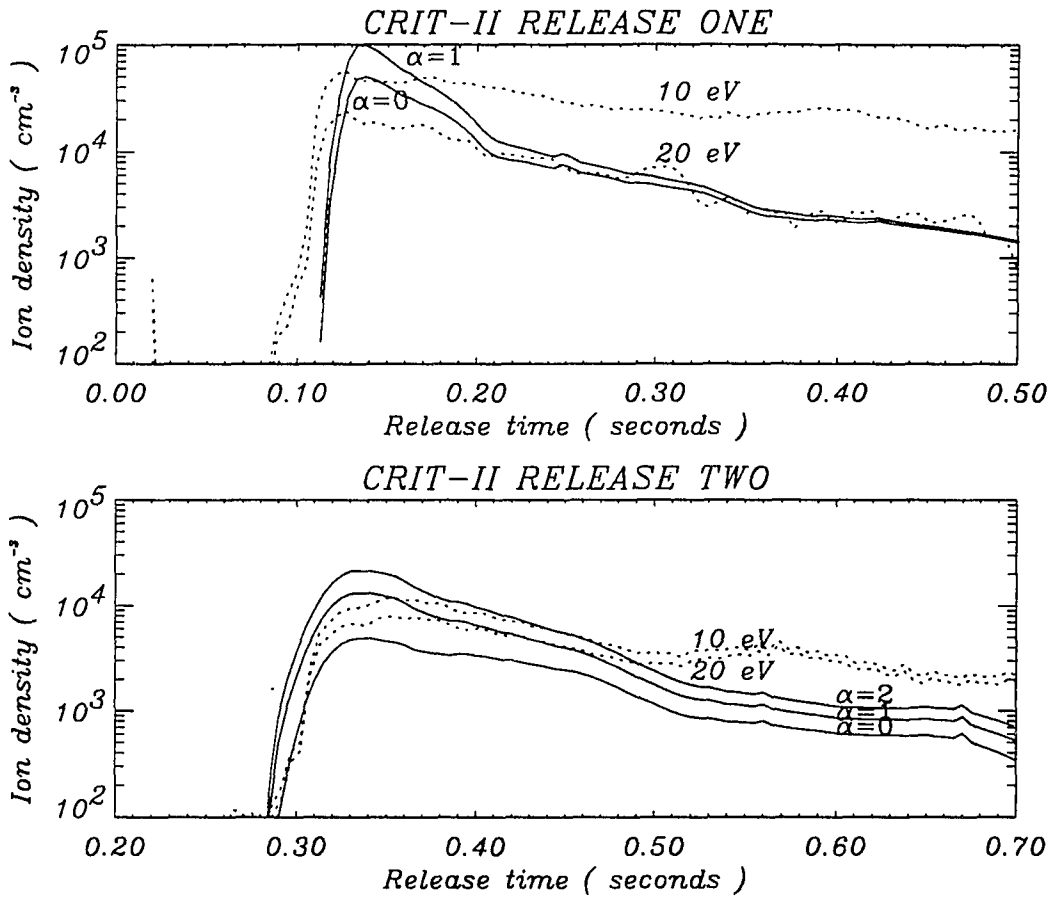

Figure 4.2: Comparison of ion densities between the observed data (dotted line) and the model results (solid lines): (a) for the first release (top) and (b) for the second (bottom) release.

in figure 4.2. There are several cases for different α values shown in figure 4.2. The observed ion densities are indicated by dotted lines and the model results by solid lines. Note that the time is referenced to the actual barium release time.

For the first release (figure 4.2(a)), one can see that two densities curves are well matched for $\alpha = 0$ during the first two-tenth of seconds, the model density shows a very sharp rising edge at onset before reaching its peak, which is about the same as the observed density, except about 10 ms of time delay. However this time

delay could be due to the errors in determination of the payload-release separation and thus has nothing to do with our model. Also, one should be noted that a small group of ions comes into the field of view at earlier time in both releases are probably the collisional accelerated high energy oxygen ions [Torbert et al., 1992]. In figure 4.2(a), one can clearly to see that when $\alpha = 0$, *i.e.* without charge exchange, the barium ion density yield due to electron impact ionization accounts for about 90 % of the total barium ion yields at the peak region compared to the 10 eV cut-off line. After 0.2 seconds, the modeled density decreases with time and almost follow the observed ion density with 20 eV cut-off. It can be understood by the follows. During the first tenth of seconds the CIV interaction was most active, barium ions lost their energy quickly to the waves which consequently heat the ambient plasma. Therefore, substantial amount of barium ions were seen at lower energy range. After this time, the CIV effect ceased, and most of the observed barium ions just followed the neutral barium energy dispersion line, and their energy will drop below 20 eV at 0.3 seconds. However, the heated ambient ions still remains and be seen by the detector, which made the 10 eV cut-off ion curve flat. From the comparison, it shows that only up to 10 % of ions were created by other ionization processes combined in the first release. In words, the calculated $Ba - O^+$ charge-exchange cross section could be too high by a factor of 10.

The model result for the second release is illustrated in figure 4.2(b). The comparison is reasonable good in the rising and trailing part of densities except the time after 0.5 seconds. By using the same argument mentioned above, the peak barium ion density resulting from the electron impact process, *i.e.* $\alpha = 0$, can only account for about 45 % of the observed ions during the active phase. To fit the first two-

tenth of seconds of the ion data after the arrival of the barium beam, one needs the multiplicative factor, α, to be a value about 1 as shown in figure 4.2(b). However, this is not consistent with the conclusion for the first release.

4.3 Discussions and Conclusions

The ionization mechanism for barium ion yield in the CRIT-II experiment is investigated. Data analysis shows that the ion density observed by the ESA detector is in agreement with the plasma density observed by RF plasma probe [Swenson et al., 1990]. The charge exchange cross section for $Ba - O^+$ is also calculated based on the "two-state approximation". It is found that electron impact ionization collision (a favored CIV ionization mechanism) and the $Ba - O^+$ charge exchange (non-CIV ionization mechanism) are two most important processes which could have been involved for the major part of barium ionization in the CRIT-II experiment. By using Liouville's theorem, we are able to model the barium density at the location of payload, which is used to compare the observed data. It is found that about 90 % of the non-thermal ions (assuming barium) were produced by electron impact ionization. On the other hand, the barium ions produced by charge exchange ionization (probably responsible for most of the non-CIV ionization yields) and other non-CIV ionizations combined are negligible in the CRIT-II experiment. However, Newell and Torbert [1985] pointed out that only one half of total hot electrons can ionize the neutral barium from ground state and another half will be used to excite the barium to meta-stable states. If we take this into account, the electron impact ionization is responsible for about 45 % of the barium ion yield in the first release observed by CRIT-II. This gives $\alpha \sim 0.6$ and the $Ba - O^+$ cross section will range

from 10^{-17} cm^2 at velocity of 4 km/sec to 1. $\times$ 10^{-15} cm^2 at velocity of 20 km/sec (see figure 4.1), but this cross section should be considered as an upper bound only.

On the contrary, the ion density observed in the second release seems to be much higher than we expected. Simulation results show that less than 25 % of barium ions were produced by the observed electrons, however our model can not reproduce this high yield of ions unless a higher charge cross section, $\alpha \sim 1.5$, is introduced. This inconsistency between the two releases could be due to the error in the determination of payload-release separation. We have a strong evidence that the barium ions were seen about 0.01 seconds earlier than that we expected. Consequently, this will reduce the barium ion production by electron impact ionization in our model result. Therefore, we think the 25 % of barium ion inventories calculated from our model should be higher.

Although we do not fully understand the conflict between the two releases, we believe that both $Ba - O^+$ charge exchange process and electron impact ionization played a comparable role in the CRIT-II experiment. According to the comparison between our density model results and observed data from two releases, the charge exchange cross section for $Ba - O^+$, shown in figure 4.1, could be very close to the exact total charge exchange cross section but with an uncertainty by a factor of 3.

A recent CRESS barium release reported by Stenbaek-Nielsen *et al.* [1993] who have analyzed the CRESS satellite optical data. Accordingly, if the charge exchange collision (a) happens, it should be followed by photo emissions at 4957 Å and 5013 Å. With the charge exchange cross section of $Ba - O^+$ at 1.0×10^{-14} cm^2 proposed by Swenson *et al.* [1990], their theoretical calculation indicated that the emission lines should be 20 times of observed data. Taking the typical neutral barium velocity

between 7 and 12 km/sec [Wescott et al., 1993], the $Ba - O^+$ charge exchange cross section is about 5.0×10^{-16} cm^2 which is very close to our calculated result.

A laboratory report of experimental results for the $Ba - O^+$ charge exchange cross section was presented as a poster by Swenson *et al.* at the 1992 AGU fall meeting. According to their preliminary results, this cross section is about 1.2×10^{-15} cm^2 at velocity of 60 km/s. Our model result shows high agreement with this value at the same velocity range. It will be interesting to see how well the two state approximation model agrees with their experimental results. However, the cross sections for a wide range of velocity has not been measured at this point in time.

CHAPTER 5

Oxygen Precursor

5.1 Introduction

CRIT-II was a shaped-charge barium release experiment conducted in the ionospheric F-region. The densities of the ambient plasma and the neutrals were though to be low, therefore, the collisional effect between the release barium beam and the background particles is negligible. However, it was found, as illustrated in Chapter 3, that the arrival time for the fastest barium beam was much earlier than that we expected. According to the neutral barium velocity distribution model [Wescott et al., 1990], the barium atoms can not reach the main payload until 0.12 seconds of release time in the first release and 0.29 seconds in the second release. One would first suspect that the separation of the barium release point from the main payload could have been measured wrong, since this will affect the fitting barium model to the data. It is possible but not likely to happen, especially, when the ion precursor was seen not only in the CRIT-II experiment but also on the CRIT-I experiment. It has been suggested by Brenning [1990] that the ion precursor observed by CRIT-I was due to the oxygen ions created by charge exchange between the ambient ionic oxygen and the super-fast neutral oxygen which originated from collisions with the fast barium. He also pointed out that this super-fast oxygen ion

then could excite the lower hybrid waves and instabilities seen by the electric field detector. Unfortunately, there was no direct evidence to support his idea because of the failure of the particle detectors on CRIT-I. However, this is not the case on CRIT-II. We have shown in Chapter 3 that a strong evidence of the ion precursor which was seen in the energy ranges from 30 to 40 eV. Since an oxygen atom is much lighter than a barium atom, after collision it can gain speed up to 1.79 times as much as that of the barium or 37% of the barium's kinetic energy. This gives an estimated energy of 37 eV for the oxygen ion. Also, the arrival time could be as early as 0.07 seconds for the first release and 0.16 seconds for the second release. This is well consistent with the observations.

The original motive of this chapter is to develop a simple model based on the binary collision theory proposed by Brenning to interpret the observed data from the CRIT-II experiment.

5.2 Binary Collision Model

In this model, only binary collision will be considered. Although the collision process between the neutral bariums and the ambient neutral oxygens could involve both elastic and inelastic, only the elastic collision will be considered. We will also assume that the neutral barium density is high enough, thus the loss of the barium neutrals due to collisions can be ignored. Likewise, the depletion of the ambient oxygen atoms due to collision will be neglected. Since the thermal velocity of the neutral oxygen is much smaller than the barium beam velocity, the cross section of barium-oxygen collision can be evaluated by classical binary collision with a stationary target. Figure 5.1 shows the configuration of the model with assuming that the

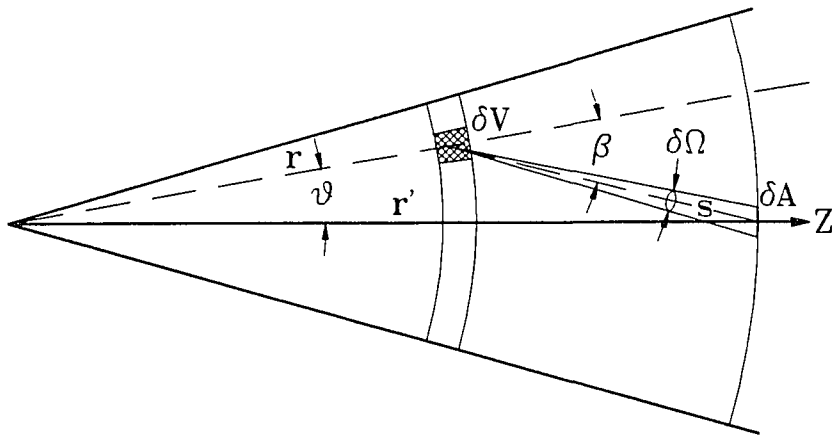

Figure 5.1: Schematic diagram of elastic collisions between the ionospheric neutral oxygen atoms and a conical barium beam.

detector is located on the symmetric axis (this assumption is true in the CRIT-II experiment).

If I_{ba} is the number of barium atoms passing through a unit area normal to the beam per unit time, there will be $d\dot{N}_{oxy}$ oxygen atoms recoiling from a scattering volume, $\delta V(\mathbf{x})$, into a solid angle, $\delta\Omega$, per second. This defines the scattering cross section as

$$d\sigma = \frac{d\dot{N}_{oxy}}{I_{ba}} \tag{5.1}$$

Experimentally, the number of particles counted per second per unit solid angle at the detector is

$$\frac{d\dot{N}_{oxy}}{d\Omega} = C_{oxy} I_{ba} \left(\frac{d\sigma}{d\Omega}\right)_{oxy} \tag{5.2}$$

where C_{oxy} is the number of scattering centers. The elastic differential cross section

for scattering target particles is given by

$$\left(\frac{d\sigma}{d\Omega}\right)_{oxy} = \frac{\sigma_{els}}{\pi} cos\beta \tag{5.3}$$

where β is the scattering angle and σ_{els} is the elastic cross section which is independent on the scattering angle. By using the neutral barium differential velocity distribution, the density of the neutral barium beam at scattering center (r, θ) is given by equation 3.1; likewise, the barium flux can be obtained immediately by

$$I_{ba} = n_{ba} v_{ba} = A \left(v^2 \frac{dN_{ba}}{dv}\right)_{v=r/t} \frac{f(\theta)}{r^3} \tag{5.4}$$

where n_{ba} and v_{ba} are the density and velocity of barium, $f(\theta)$ is a Gaussian-like angular distribution with an e-folding decrease at $\theta = \theta_w$ (the beam angular width), and A is a normalized constant of $f(\theta)$ over the solid angle.

The solid angle subtended by an area of element, $\delta A(\mathbf{x}')$, at the observation point of distance s from the scatter center is

$$\begin{aligned} \delta\Omega &= \frac{\delta A(\mathbf{x}) \cdot \mathbf{s}}{s^3} \\ &= \frac{\delta A cos(\beta - \theta)}{s^2} \end{aligned} \tag{5.5}$$

Since the observational point is located on the beam axis, this problem can be considered as axial-symmetric with respect to the beam axis. The distance between the scattering center and observation point, s, and the scattering angle, β, can be expressed by

$$s = \left(R^2 - 2Rrcos\theta + r^2\right)^{1/2} \tag{5.6}$$

and

$$cos\beta = \frac{Rcos\theta - r}{s} \tag{5.7}$$

Substituting equations (5.3) - (5.7) into equation (5.2), we obtain the number of atomic oxygens scattered into an area, δA, per unit time,

$$\delta \dot{N}_{oxy} = C_{oxy} \frac{\sigma_{els}}{\pi} cos\beta \left(v^2 \frac{dN_{ba}}{dv} \right) \frac{f(\theta)}{r^3} \frac{cos(\beta - \theta)}{R^2 - 2Rrcos\theta + r^2} \frac{\delta A cos(\beta - \theta)}{s^2} \tag{5.8}$$

in which $C_{oxy} = n_{oxy} 2r^2 sin\theta d\theta dr$ is the number of target oxygen atoms in a scattering volume of δV (a circular ring in this case). Dividing equation (5.8) by an area $\delta A cos(\beta - \theta)$, we obtain the flux and density for the oxygen beam, i.e.

$$\delta n_{oxy} = \frac{\delta I_{oxy}}{v_{oxy}} = \frac{\delta \dot{N}_{oxy}}{v_{oxy} \delta A cos(\beta - \theta)} \tag{5.9}$$

where the velocity of the oxygen atom, v_{oxy}, is given by, after collision,

$$v_{oxy} = \frac{2m_{ba}}{m_{ba} + m_{oxy}} v_{ba} cos\beta \tag{5.10}$$

The total oxygen beam density is obtained by integrating the scattering volume over the region occupied by the of barium beam. This gives

$$n_{oxy}(R,t) = \frac{2A\sigma_{els} n_{oxy}}{\gamma} \int_{\theta=0}^{\theta_w} \int_{r=0}^{R} \left(v^2 \frac{dN_{ba}}{dv} \right)_{v=r/t} \frac{f(\theta)}{r} \frac{cos(\beta - \theta)}{R^2 - 2Rrcos\theta + r^2} sin\theta d\theta dr \tag{5.11}$$

The velocity $v(= r/t)$ in equation (5.11) has, however, a different meaning now and can be determined by the total time of flight for the barium and oxygen atoms from the release point undergoing one collision to the detector, *i.e.*

$$t = t_{ba} + t_{oxy} = \frac{r}{v_{ba}} + \frac{s}{v_{oxy}} = \frac{1}{v_{ba}} \left(r + \frac{s}{\gamma cos\beta} \right) \tag{5.12}$$

which leads to the barium velocity for the integral in equation (5.11) at time t

$$v_{ba} = \frac{1}{t} \left(r + \frac{s}{\gamma cos\beta} \right) \tag{5.13}$$

By using equations (5.11), (5.12) and (5.13), a time dependent velocity distribution for the collisional neutral oxygen beam at the locations on the barium beam axis can be determined.

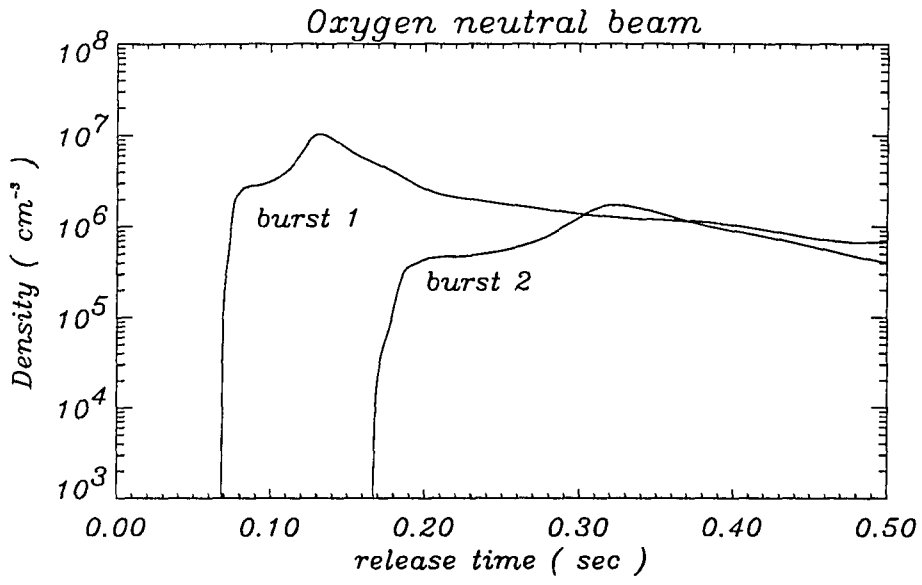

Figure 5.2: Model calculation of neutral oxygen density for CRIT-II experiment at the location of two releases.

5.3 Numerical Calculation and Discussion

To apply our model result, equations (5.8) - (5.13), to the CRIT-II experiment, the actual neutral barium differential velocity distribution [Wescott et al., 1990] will be used as well as the release parameters. The density of the atomic oxygen beam produced by collisions with a heavier barium beam for the two releases has been calculated numerically and shown in figure 5.2.

The parameters used for model calculation are $\sigma_{els} = 3.4 \times 10^{-15}\ cm^{12}$, $n_{oxy} = 1 \times 10^{8}\ cm^{-3}$, $R = 1.585\ km$ for the first release, and $R = 3.881\ km$ for the second release. In figure 5.2, one can see that the atomic oxygen beam can reach the main payload as early as 0.07 and 0.17 seconds of the release time in the first and second release, respectively. This is consistent with the observation in regard to the timing

problem and the energy requirement.

This atomic oxygen beam, as mentioned previously, will undertake charge-exchange with the ionospheric oxygen ions and create an ionic oxygen beam observed by the ion detector. Note that charge exchange collision acts like a head-on collision between particles of equal mass. The oxygen ion beam density production rate is thus proportional to the density flux of the incident beam and the charge exchange cross section.

$$\dot{n}_{o+}^{str} = n_{oxy} n_{o+} \sigma_{ex} v_{oxy} \tag{5.14}$$

where 'str' denotes the streaming particles. In (5.14), we have assumed that σ_{ex} is independent of the beam velocity. Assuming the polarization electric field is very weak during this early time, once a charge exchange collision occurred, this new born ion will gyrate around the same magnetic field line where it is ionized. Owing to its small gyroradius, only the oxygen ions created nearby the main payload will be observed by the ion detector. Since there will be no convecting ions due to the $E \times B$ drift ($E = 0$ during the precursor time), the oxygen ion beam density can be simply calculated by integrating equation (5.14) over the time. Figure 5.3 shows the oxygen ion beam density with $\sigma_{ex} = 4. \times 10^{-15}\ cm^2$ and $n_{o+} = 5.41 \times 10^5\ cm^{-3}$ for both releases.

In figure 5.3, the observed ion density has been converted to oxygen by multiplying a factor of square root of mass ratio, $\sqrt{m_o/m_{ba}} = 0.34$. The comparison for the first release is quite good up to about 0.1 seconds except a small ion tail at the leading edge. However the comparison for the second release is not as good as that in burst one. The timing for the first incoming ions is in good agreement with the model result but the magnitude of ion density is not very consistent before 0.25 sec-

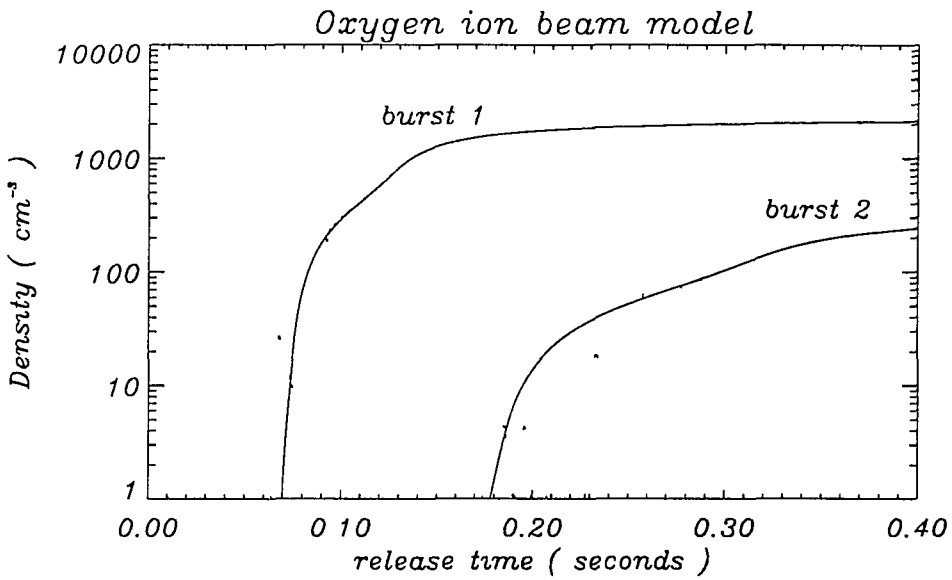

Figure 5.3: Model calculation of oxygen ion beam densities (solid lines) and observed ion densities (dashed line) for CRIT-II at locations of two releases.

onds (the fastest barium arrival time is 0.29 s). This could be due to the density of the ion beam being too low and too diffusive in space to be observed. Interestingly, ions were always observed earlier than that predicted by our model. It may suggest that a small errors in the determination of release-payload distance could exist. On the other hand, this might be due to a sharp density drop-off in the high energy tail in the neutral barium model.

5.4 Conclusion

The question of the precursor ions observed by the ion ESA detector on CRIT-II has been addressed. Based on a simple binary collision theory proposed by Brenning [1990], a general time-dependent neutral oxygen beam velocity distribution was derived. The density of the neutral oxygen beam obtained from this model was also

used to calculate the density of energetic oxygen ions based on the charge exchange collision. Our model results represent reasonable consistent with the observations in regard to the timing and the magnitude of density issues. Although ions were observed always slightly earlier than that predicted by our model, we believe that the ion precursor is most likely to be the oxygen created as a result of the snow-plow effect.

CHAPTER 6

Electron Preheating

6.1 Introduction

According to the current theories, the CIV effect involves energy transfer from energetic ion beams to electrons by collective wave-particle interactions. This energy transfer enables electrons to gain energy to ionize neutral beams by impact collision. The new-born ion beams will subsequently enhance more plasma waves and produce more hot electrons to achieve an anomalous ionization. The electron heating essentially plays one of the major roles in the CIV effect, and understanding the mechanism of electron heating is the key to the construction of CIV theory.

Broad band electrostatic fluctuations were observed by the CRIT-II field measurements [Swenson et al., 1990]. The dominant wave spectra changed in frequencies initially, right before the main barium beam arrived, from the ambient lower hybrid waves to the ion cyclotron and ion acoustic waves during the active phase. It is suggested by Torbert *et al.* [1992] that the heated electron fluxes seen by the CPA detector were generated as a result of electron heating which took place during the passage of a barium beam by wave-plasma interactions. This could be true for the main part of observed data but not for the early growth phase. The observed particle densities and waves are plotted in figure 6.1 in order to understand this question.

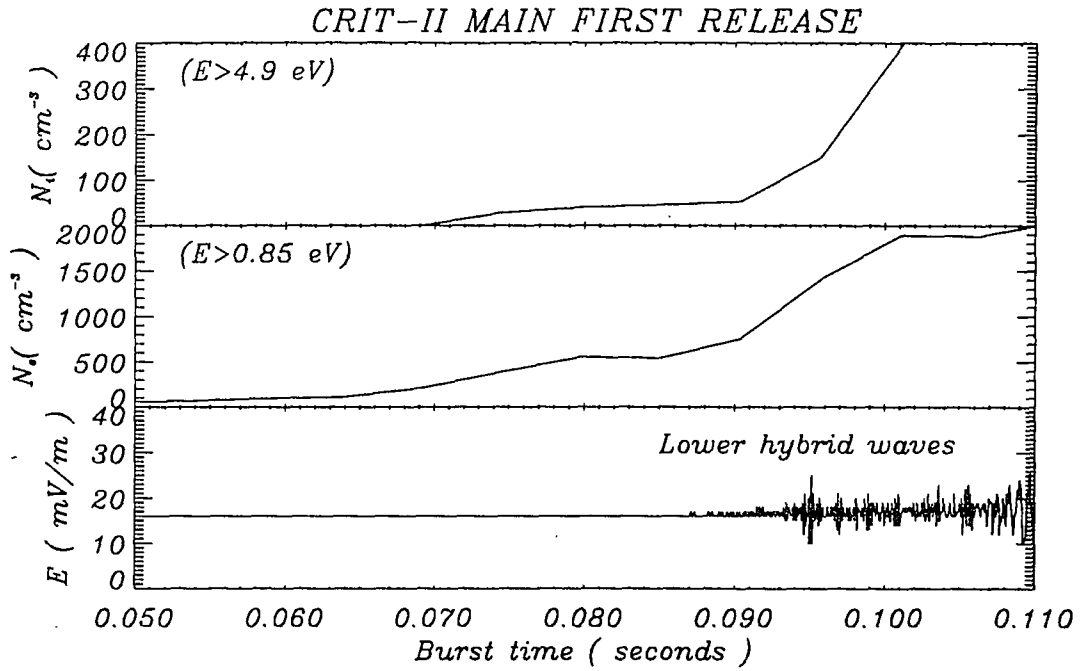

Figure 6.1: left: Ion Beam density (top panel), hot electron ($E > 0.85\ eV$) density (middle), and electric field fluctuations (bottom) along the beam direction observed by CRIT-II main payload, where the time is referenced to the barium release time.

The nonthermal ion density observed by the ion ESA detector (top panel) shows that a thin ion beam (ion precursor) reached the detector as early as 0.07 seconds of burst time. However, the electron density curve illustrated in the middle panel shows that the heated electrons were created even earlier than 0.07 seconds while the disturbance of the wave (bottom panel) was not observed until 0.085 seconds.

There are many questions still remaining in above data set: why were the heated electrons and the nonthermal ions observed earlier without generating any measurable waves? where did the heated electrons come from? and are the precursor ions responsible for the early stage of electron heating?

The time inconsistency between charged particles and waves could be due to

the density of the ion beam being too low to excite any disturbance of observable level. If this is the case, then the heated electrons observed earlier than 0.085 seconds can not be considered as locally created. It is still not clear how those early observed electrons were created. because they could be heated locally or they could be convecting electrons energized somewhere upstream to the payload.

It was reported by Swenson *et. al.* [1990] that the lower hybrid waves of ambient oxygen ions are the dominant wave modes in the precursor region. The amplitude of waves is small and remains constant at maximum value of about 20 mV/m (see the bottom panel in figure 6.1). According to the classic electromagnetic theory, the kinetic energy density of electrons in wave electric fields is given by

$$W_e = W_{es}\frac{\partial}{\partial\omega}\omega\chi_e(\omega)\mid_{\omega_r} \tag{6.1}$$

where W_{es} ($=\mid E \mid^2 /8\pi$) is the electric field energy density and χ_e is the electron susceptibility. If we take the average amplitude $E = 15\ mV/m$ for electric fields and $\chi_e \simeq \omega_e^2/\Omega_e^2 - \omega_e^2/\omega^2(k_\parallel^2/k^2)$ for the lower hybrid wave, where ω_e is the electron plasma frequency and Ω_e is the electron gyro-frequency, then equation (6.1) leads to $W_e \simeq 0.5\ eV/cm^3$ which is much smaller than the observed data by three orders of magnitude. Therefore, the amplitude of these lower hybrid waves is too small for electrons to attain substantial energy density measured by the electron detector. On the other hand, an anomalous heating mechanism probably by wave instability is needed in order to explain the observed hot electrons.

It was first suggested by Sherman [1972] that the lower hybrid instabilities induced by an ion beam in a magnetized plasma could be the candidate for the electron heating mechanism in the CIV effect. Although it has not been identified experimentally, theoretical studies and computer simulations have reached

the same conclusion that the lower hybrid instabilities can very efficiently convert ion beam energy to electron energy [McBride et al., 1972; Formisano et al., 1982; Machida and Goertz, 1986]. It has also been widely used as the main mechanism to the electron heating on many CIV related works [Galeev and Chabibrachmanov, 1983, Formisano *et al.*, 1982, Papadopoulos, 1982, Goertz *et al.*, 1985, Machida and Goertz, 1988, Mobius *et al.*, 1987] .

According to the beam plasma theories, an ion beam across a magnetized plasma induces plasma waves, which are unstable at the frequencies of lower hybrid waves and hence the transferring of the kinetic energy from a fast ion beam to the ambient plasma can be achieved by Landau resonance. In CRIT-II, the wave structure has not been understood except for the precursor region (from 0.085 to 0.1 seconds). Therefore, only electron heating associated with the precursor waves will be investigated in this chapter. To calculate the electron heating, the quasi-linear theory will be employed.

6.2 Lower Hybrid Quasi-linear Diffusion Model

In this section, a one dimensional quasi-linear model associated with the lower hybrid waves will be established based on a three dimensional quasi-linear theory developed by Ishihara and Hirose [1984] . The equations which describe a resonant wave-particle interaction resulting in slow changes of a particle distribution function in velocity space may be given by

$$\frac{\partial f(\mathbf{v})}{\partial t} = \frac{\partial}{\partial \mathbf{v}} \cdot \mathbf{D} \cdot \frac{\partial f(\mathbf{v})}{\partial \mathbf{v}} \tag{6.2}$$

$$\frac{\partial \mathcal{E}_{\mathbf{k}}(t)}{\partial t} = 2\gamma_{\mathbf{k}} \mathcal{E}_{\mathbf{k}}(t) \tag{6.3}$$

where $\mathbf{D}$ is the diffusion tensor and is defined by

$$\mathbf{D} = -\imath \left(\frac{q}{m}\right)^2 8\pi \int \frac{\mathcal{E}_{\mathbf{k}}}{(\mathbf{k}\cdot\mathbf{v} - \omega(\mathbf{k}))} \frac{\mathbf{kk}}{\mid k^2 \mid} d\mathbf{k} \tag{6.4}$$

$\mathcal{E}_{\mathbf{k}}$ ($=\mid E_{\mathbf{k}} \mid^2 /8\pi$) is the electric field energy density, and $\omega(\mathbf{k})$ ($= \omega_{\mathbf{k}} + \imath\gamma_{\mathbf{k}}$) is the complex wave frequency of mode $\mathbf{k}$. In quasilinear theory, the diffusion tensor is a function of the particle distribution. Therefore, the particle distribution is allowed to evolve in time nonlinearly while the amplitude of waves is considered to be so small that the linear wave theory is still applicable.

To calculate the wave dispersion relation, linear perturbation theory will be employed. For a low β ionospheric plasma, the electrostatic approximation will be assumed. Therefore the wave dielectric function excited by a beam in a plasma is just the linear combination of the susceptibilities of plasma and beam plus 1 (response of free space). Despite the fact that there exists a small concentration of H^+ and He^+ ions, we will assume that the ionospheric plasma consists of oxygen ions, O^+, and an equal amount of electrons only. Since we are interested in the lower hybrid waves, in this frequency range, $\Omega_o \ll \omega_{lho} \ll \Omega_e$, where ω_{lho} is the lower hybrid wave frequency of oxygen, Ω_o and Ω_e are the gyrofrequencies of oxygen and electron, respectively, electrons can be considered as highly magnetized while ions are effectively unmagnetized. Futhermore, both ion and electron distributions can be anisotropic with respect to the ambient magnetic field, $\mathbf{B}_0$, pointing in z direction. The ion beam is assumed to be isotropic and unmagnetized with finite temperature, but it will not involve the diffusion nonlinearly in time. This assumption poses some limitations on this model result. We will come back to discuss it later.

A general kinetic dispersion relation for the system of this type can be obtained from, for example, Swanson [1989]. Under the assumptions that we made above, the

real part of dielectric response function is immediately given by

$$\epsilon_R = 1 - \frac{\omega_o^2}{\omega_{\mathbf{k}}^2} + \frac{2\omega_e^2}{k^2 v_{\|e}^2}[\delta - \Lambda_0(\lambda_e)] - \frac{k_\|^2}{k^2}\frac{\omega_e^2}{\omega_{\mathbf{k}}^2}\Lambda_0(\lambda_e) \tag{6.5}$$

where ω_o and ω_e are the ion and electron plasma frequencies, $\delta = T_{\|e}/T_{\perp e}$, $\lambda_e = k^2 v_{\perp e}^2/2\Omega_e^2$, $v_{\perp e}$ $(= \sqrt{2T_{\perp e}/m_e})$ is the electron perpendicular thermal speed, $\Lambda_n(x) = I_n(x)\exp(-x)$, and I_n is the modified bessel function of nth order. Note that in equation (6.5) we have ignored the principle part of ion beam dielectric function since the density ratio of ion beam to the ambient oxygen ion is very small $(n_b/n_o \sim 10^{-3})$.

The wave modes are obtained by solving the zeros of (6.5) , this leads to

$$\omega_{\mathbf{k}}^2 = \omega_{lho}^2[1 + \frac{k_\|^2}{k^2}\frac{m_o}{m_e}\Lambda_0(\lambda_e)] \tag{6.6}$$

where

$$\omega_{lho} = \frac{\omega_o}{\sqrt{1 + \frac{2\omega_e^2}{k^2 v_{\|e}^2}(\delta - \Lambda_0)}} \tag{6.7}$$

is the lower hybrid frequency of oxygen. Since the growth (or damping) rate, $\gamma_{\mathbf{k}}$, is assumed to be small in quasilinear approximation, thus it can be expressed by

$$\begin{aligned} \gamma_{\mathbf{k}} &= -\epsilon_I(\mathbf{k}, \omega_{\mathbf{k}})/\frac{\partial \epsilon_R}{\partial \omega_{\mathbf{k}}} \\ &= \frac{\omega_{\mathbf{k}}}{1 + \frac{2\omega_e^2}{k^2 v_{\|e}^2}(\delta - \Lambda_0)}(\gamma_I^b + \gamma_I^o + \gamma_I^e) \end{aligned} \tag{6.8}$$

in which

$$\gamma_I^b = \sqrt{\pi}\frac{\omega_b^2}{k^2 v_b^2}(\frac{\omega_{\mathbf{k}} - \mathbf{k}\cdot\mathbf{v}_0}{k v_b})\exp\left[-(\frac{\omega_{\mathbf{k}} - \mathbf{k}\cdot\mathbf{v}_0}{k v_b})^2\right] \tag{6.9}$$

$$\gamma_I^e = \pi\frac{\omega_e^2}{k^2}\int d^3\mathbf{v} k_\| \frac{\partial f_e}{\partial v_\|} J_0(\frac{k_\perp v_\perp}{\Omega_e})\delta(\omega_{\mathbf{k}} - k_\| v_\|) \tag{6.10}$$

$$\gamma_I^o = \pi\frac{\omega_o^2}{k^2}\int d^3\mathbf{v}\mathbf{k}\cdot\frac{\partial f_o}{\partial \mathbf{v}}\delta(\omega_{\mathbf{k}} - \mathbf{k}\cdot\mathbf{v}) \tag{6.11}$$

A general form of the diffusion tensor appearing in equation (6.2) has been given

by, for example, Davidson [1972] and it can be separated into resonant and non-resonant parts, *i.e.*

$$\begin{aligned}\mathbf{D} &= \frac{8\pi e^2}{M^2}\sum_{\mathbf{k}}\frac{\mathbf{kk}}{k^2}\mathcal{E}_{\mathbf{k}}(t)[P\frac{\gamma_{\mathbf{k}}}{(\omega_{\mathbf{k}}-\mathbf{k}\cdot\mathbf{v})}+\pi\delta(\omega_{\mathbf{k}}-\mathbf{k}\cdot\mathbf{v})] \\ &= \mathbf{D}^{nr}+\mathbf{D}^{r} \qquad (6.12)\end{aligned}$$

where "P" denotes the principle value, δ is the Dirac Delta function, and $\mathbf{D}^{nr}$ and $\mathbf{D}^{r}$ are the nonresonant and resonant parts of the diffusion tensor, respectively. This problem is symmetric with respect to the direction of the ambient magnetic field, the vector product $\mathbf{k}\cdot\mathbf{v}$ appearing in the above equation can be written as its components in the cylindrical coordinate system, $\mathbf{k}\cdot\mathbf{v} = k_\perp v_\perp\cos\alpha + k_{||}v_{||}$, where α is the angle between $k_\perp$ and $v_\perp$. Thus this problem can be simplified by taking the average over the angle α. After carrying out the integration $\int_0^{2\pi} d\alpha/2\pi$ in equation (6.2), one gets

$$\frac{\partial f(v_\perp,v_{||},t)}{\partial t} = \left(\frac{1}{v_\perp}\frac{\partial}{\partial v_\perp}v_\perp, \frac{\partial}{\partial v_{||}}\right)\begin{pmatrix} D_{\perp\perp} & D_{\perp||} \\ D_{||\perp} & D_{||||}\end{pmatrix}\begin{pmatrix}\partial/\partial v_\perp \\ \partial/\partial v_{||}\end{pmatrix} f(v_\perp,v_{||},t) \qquad (6.13)$$

Equation (6.13) can be solved for $f(v_\perp,v_{||},t)$ with given diffusion tensors. For unmagnetized oxygen ions ($\omega \gg \Omega_o$) the resonant and nonresonant diffusion tensors are given in (6.14) and (6.15) [Ishihara and Hirose, 1983]

$$\begin{pmatrix} D_{\perp\perp} \\ D_{\perp||,||\perp} \\ D_{||||}\end{pmatrix}^{r}_{o} = \frac{8\pi e^2}{M_o^2}\sum_{\mathbf{k}}\mathcal{E}_{\mathbf{k}}(t)\tau^r_{\mathbf{k}}(v_\perp,v_{||}) \qquad (6.14)$$

$$\begin{pmatrix} D_{\perp\perp} \\ D_{\perp||,||\perp} \\ D_{||||}\end{pmatrix}^{nr}_{o} = \frac{8\pi e^2}{M_o^2}\sum_{\mathbf{k}}\mathcal{E}_{\mathbf{k}}(t)\tau^{nr}_{\mathbf{k}}(v_\perp,v_{||}) \qquad (6.15)$$

where $\tau^{nr}_{\mathbf{k}}(v_\perp,v_{||})$ and $\tau^{r}_{\mathbf{k}}(v_\perp,v_{||})$ have dimension of time and are defined by

$$\tau^{nr}_{\mathbf{k}} = \frac{\gamma_{\mathbf{k}}|\,\omega-k_{||}v_{||}\,|/k^2}{\left((\omega-k_{||}v_{||})^2-k_\perp^2v_\perp^2\right)^{3/2}}\begin{pmatrix} 2k_\perp^2-\left(\frac{\omega-k_{||}v_{||}}{v_\perp}\right)^2 \\ k_{||}\left(\frac{\omega-k_{||}v_{||}}{v_\perp}\right) \\ k_{||}^2\end{pmatrix} \qquad (6.16)$$

$$\tau^{r}_{\mathbf{k}} = \frac{1/k^2}{\sqrt{(\omega-k_{||}v_{||})^2-k_\perp^2v_\perp^2}}\begin{pmatrix} \left(\frac{\omega-k_{||}v_{||}}{v_\perp}\right)^2 \\ k_{||}\left(\frac{\omega-k_{||}v_{||}}{v_\perp}\right) \\ k_{||}^2\end{pmatrix} \qquad (6.17)$$

The diffusion tensor for plasmas in a magnetic field has been derived by Kennel and Englemann [1966]. If $\omega_{\mathbf{k}} \ll \Omega_e$, keeping the lowest order term, *i.e.* $n = 0$ term, and omitting other high order terms, we obtain

$$\begin{pmatrix} D^r_{\parallel\parallel} \\ D^{nr}_{\parallel\parallel} \end{pmatrix}_e = \frac{8\pi e^2}{m_e^2} \sum_{\mathbf{k}} \mathcal{E}_{\mathbf{k}}(t) \frac{k_\parallel^2}{k^2} J_0^2\left(\frac{k_\perp v_\perp}{\Omega_e}\right) \begin{pmatrix} \pi\delta(\omega_{\mathbf{k}} - k_\parallel v_\parallel) \\ \frac{\gamma_{\mathbf{k}}}{(\omega_{\mathbf{k}} - k_\parallel v_\parallel)^2} \end{pmatrix} \tag{6.18}$$

where J_0 is the first kind Bessel function of zero order.

Since the growth rate for the lower hybrid instabilities exists only in a very narrow region of wave number space centered around the condition of maximum growth rate $k_\parallel/k_\perp \simeq \sqrt{m_e/M_o}$ [McBride et al., 1972], we can further simplify this problem from a two dimensional to a one dimensional problem. Ions are expected to diffuse in the perpendicular direction while electrons will mainly diffuse in the parallel direction with respect to the ambient magnetic field. Therefore (6.10) and (6.11) become

$$\gamma_I^e = \frac{k_\parallel}{|\, k_\parallel \,|} \frac{\omega_e^2}{k^2} \Lambda_0\left(\frac{k_\perp^2 v_{\perp e}^2}{2\Omega_e^2}\right) \frac{\partial f_e(v_\parallel)}{\partial v_\parallel} \Big|_{v_\parallel = \frac{\omega}{k_\parallel}} \tag{6.19}$$

$$\gamma_I^o = 2\pi \frac{\omega_o^2}{k^2} \int_{\frac{\omega}{k_\perp}}^{\infty} \frac{\omega_{\mathbf{k}} \frac{\partial f_o}{\partial v_\perp}}{\sqrt{k_\perp^2 v_\perp^2 - \omega_{\mathbf{k}}^2}} dv_\perp \tag{6.20}$$

The diffusion equations and the diffusion tensors for oxygens, $D^o_{\perp\perp} \gg D^o_{\perp\parallel} \gg D^o_{\parallel\parallel}$, and electrons, $D^e_{\parallel\parallel} \gg D^e_{\perp\parallel} \gg D^e_{\perp\perp}$, become

$$\frac{\partial f_o(v_\perp, t)}{\partial v_\perp} = \frac{1}{v_\perp} \frac{\partial}{\partial v_\perp} v_\perp D^o_{\perp\perp} \frac{\partial f_o(v_\perp, t)}{\partial v_\perp} \tag{6.21}$$

where

$$D^o_{\perp\perp} = \frac{8\pi e^2}{M_o} \sum_{\mathbf{k}} \mathcal{E}_{\mathbf{k}}(t) \frac{k_\perp^2}{k^2} \left\{ \frac{\omega_{\mathbf{k}}^2/k_\perp^2 v_\perp^2}{\sqrt{\omega_{\mathbf{k}}^2 - k_\perp^2 v_\perp^2}} + \frac{\gamma_{\mathbf{k}} \omega_{\mathbf{k}}}{(\omega_{\mathbf{k}} - k_\parallel v_\parallel)^{3/2}} \left[2 - \left(\frac{\omega_{\mathbf{k}}}{k_\perp v_\perp} \right)^2 \right] \right\} \tag{6.22}$$

and

$$\frac{\partial f_e(v_\parallel, t)}{\partial v_\parallel} = \frac{\partial}{\partial v_\parallel} D^e_{\parallel\parallel} \frac{\partial f_e(v_\parallel, t)}{\partial v_\parallel} \tag{6.23}$$

where $D^e_{||||}$ is given by equation (6.18) with $J_0^2(\frac{k_\perp v_\perp}{\Omega_e})$ replacing by 1.

Equations (6.3), (6.6) - (6.9), and (6.18) - (6.23) compose a system of equations which describes the dynamic evolution of the ion and electron velocity distributions due to the effective diffusion by lower hybrid waves. The procedure to solve this system equation set can be performed as follows. Assuming the oxygen and electron distribution functions, f_o and f_e, are known at certain time t, the instantaneous temperatures $T_{||e}$ and $T_{\perp o}$ can be evaluated by integrating energy over the velocity space. Subsequently, the frequencies of the waves can be determined from the dispersion relation (6.8). The growth rates $\gamma_{\mathbf{k}}$ are then evaluated from equation (6.8), (6.9), (6.19), and (6.20) which in turn yields the spectral energy density, $\mathcal{E}_{\mathbf{k}}$, through equation (6.3). The diffusion tensors are next to be determined from equations (6.18) and (6.22). Equations (6.21) and (6.23) are then solved by means of numerical integration which will be described detailed in the next section.

6.3 Numerical Scheme

In solving the system equations, both ion and electron distribution functions are assumed to be Maxwellian initially, *i.e.*

$$f_o(v_\perp, t=0) = \left(\frac{M_o}{\pi T_{\perp o0}}\right) \exp\left(-\frac{M_o}{T_{\perp o0}} v_\perp^2\right) \tag{6.24}$$

$$f_e(v_{||}, t=0) = \left(\frac{m}{\pi T_{||e0}}\right)^{1/2} \exp\left(-\frac{m}{T_{||e0}} v_{||}^2\right) \tag{6.25}$$

Where T_{o0} and T_{e0} are the initial temperature of oxygens and electrons. The boundary conditions imposed for $f_o(v_\perp, t)$ and $f_e(v_{||}, t)$ are

$$f_o(v_{\perp max}, t) = 0 \tag{6.26}$$

$$\partial f_o(v_\perp = 0, t)/\partial v_\perp = 0 \tag{6.27}$$

$$f_e(v_{\|max}, t) = f_e(v_{\|min}, t) \;=\; 0 \tag{6.28}$$

The computational domain for the velocity space of oxygen is $v_{\perp max} = 15\ C_{s0}$, with increment $\Delta v_\perp = 0.3\ C_{s0}$, and for the velocity space of electron is $v_{\|max} = -v_{\|min} = 2000\ C_{s0}$, with increment $\Delta v_\| = 40\ C_{s0}$, where C_{s0} $(= \sqrt{T_{e0}/M_o})$ is the oxygen ion acoustic speed. The wave number space is divided into 40 mesh points for $k_\|$ with ranges of $k_\| \rho_{e0} = 0.05 - 1.0$, where ρ_e is the electron Debye length, and 30 mesh points for $k_\perp$ with ranges around the maximum growth rate region, *i.e.* $k_\perp \simeq \sqrt{M_o/m_e}\ k_\|$. Note that the wave number space is initially chosen the way such that the Landau damping effect is negligible.

An implicit finite difference scheme (for example, see [Ames, 1977]) is chosen for solving the partial differential equations (6.21) and (6.23). Let Δt be the time step and Δv be the cell size of velocity, then we can define the first and second difference approximations for nth time step and jth velocity grid point by central difference scheme

$$(\delta f)_j^n \;=\; (f_{j+1}^n - f_{j-1}^n)/2\Delta v \tag{6.29}$$

$$(\delta^2 f)_j^n \;=\; (f_{j+1}^n - 2f_j^n + f_{j-1}^n)/(\Delta v)^2 \tag{6.30}$$

Therefore equation (6.21) can be approximated by following the implicit difference equation

$$\frac{(f_j^{n+1} - f_j^n)}{\Delta t} = \frac{1}{v_j} \frac{\theta\,[\delta(vD\delta f)]_j^{n+1} + (1-\theta)\,[\delta(vD\delta f)]_j^n}{(\Delta v)^2} \tag{6.31}$$

where $1/2 \le \theta \le 1$. Generally, $\theta = 1/2$ is used for the best result. We wish to solve this equation for the unknown f_j^{n+1}, j=0,1,2,.....J. A common way is to rewrite the above difference equation as a set of simultaneous algebraic equations

$$\alpha_j^{n+1} f_{j+1}^{n+1} - (1 + \beta_j^{n+1}) f_j^{n+1} + \gamma_j^{n+1} f_{j-1}^{n+1} = \psi_j^n \tag{6.32}$$

where

$$\alpha_j^n = [\Delta t/(\Delta v)^2]\theta v_j^+ D_{j+1/2}^n \tag{6.33}$$

$$\gamma_j^n = [\Delta t/(\Delta v)^2]\theta v_j^- D_{j-1/2}^n \tag{6.34}$$

$$\beta_j^n = \alpha_j^n + \gamma_j^n \tag{6.35}$$

$$\begin{aligned}\psi_j^n &= (1-1/\theta)\alpha_j^n f_{j+1}^n - [1+(1-1/\theta)\beta_j^n] f_j^n \\ &+ (1-1/\theta)\gamma_j^n f_{j-1}^n\end{aligned} \tag{6.36}$$

$$v_j^{\pm} = 1 \pm \Delta v/2v_j \tag{6.37}$$

For the electron diffusion equation (6.23), we can use the same results formulated above with only one exception of substituting $v_j^{\pm}$ by 1.

In equation (6.32), we have the unknown $f_j^{n+1}, j = 1, 2, ...J-1$ on the left hand side of the equal sign and the known quantities on the right hand side. These equations are needed to be solved only for the grid points $j = 1, 2.....J-1$, since the boundary conditions determine the solutions for $j = 0$ and $j = J$. Consequently, the calculation for the singularity at $v = 0$ is avoided. The system given by equation (6.32) is nonlinear in the unknown f_j^{n+1}, *i.e.* the coefficients $\alpha_j^{n+1}, \beta_j^{n+1}, etc.$, are unknown. If we can extrapolate them from their values at previous time steps t^n and t^{n-1}, then equation (6.32) becomes a linear algebraic system in the unknown f_j^{n+1}. The procedure is to extrapolate the coefficients and solve the linear system, then compute the coefficients α_j^{n+1}, β_j^n, *etc.*, with the new value of f_j^{n+1}.

To solve a set of linearized equations (6.32), let

$$f_{j-1}^{n+1} = \zeta_{j-1}^{n+1} f_j^{n+1} + \xi_{j-1}^{n+1} \tag{6.38}$$

where coefficients ζ and ξ are to be determined. Then equation (6.32) becomes

$$f_j^{n+1} = \frac{\alpha_j^{n+1} f_{j+1}^{n+1} + \gamma_j^{n+1}\xi^{n+1} - j - 1 - \psi_j^n}{1 + \beta_j^{n+1} - \gamma_j^{n+1}\zeta_{j-1}^{n+1}} \tag{6.39}$$

From (6.39) we can define

$$\zeta_j^{n+1} = \frac{\alpha_j^{n+1}}{1 + \beta_j^{n+1} - \gamma_j^{n+1}\zeta_{j-1}^{n+1}} \tag{6.40}$$

$$\xi_j^{n+1} = \frac{\gamma_j^{n+1}\xi_{j-1}^{n+1} - \psi_j^n}{1 + \beta_j^{n+1} - \gamma_j^{n+1}\zeta_{j-1}^{n+1}} \tag{6.41}$$

$$j = 1, 2, \ldots\ldots\ldots\ldots J-1$$

From the boundary conditions $\partial f/\partial v = 0$ at $v = 0$, we take $f_0^{n+1} = f_1^{n+1}$, so we have $\zeta_0^{n+1} = 1$ and $\xi_0^{n+1} = 0$ for each of every time step n.

6.4 Results and Discussions

In the numerical computations, all the physical parameters used for the initial conditions are based on the experimental data measured by CRIT-II. The ambient electron and oxygen are initially isotropic with $T_e = T_o = 0.2\ eV$ and $n_e = n_o = 5.4 \times 10^5\ cm^{-3}$ [Swenson et al., 1990]. The energetic ion beam density and velocity used in our calculation are $2.0 \times 10^2\ cm^{-3}$ and $1.5 \times 10^6\ cm/sec$, respectively. The temperature of the beam, however, was not measured, an estimated temperature of $T_b = 0.2\ eV$ for ion beam will be used.

Figure 6.2(a) shows the time evolution of the electron distribution. The initial distribution of electrons is assumed to be Maxwellian. As time goes on, one can clearly see that the high energy part of electron distribution is stretched out to form high energy electron tails. The electron, the oxygen beam, and the wave energy densities are shown in figure 6.2(b) as functions of time, in which the electron energy density (solid line) is evaluated by the electrons which have energy exceeding 0.85

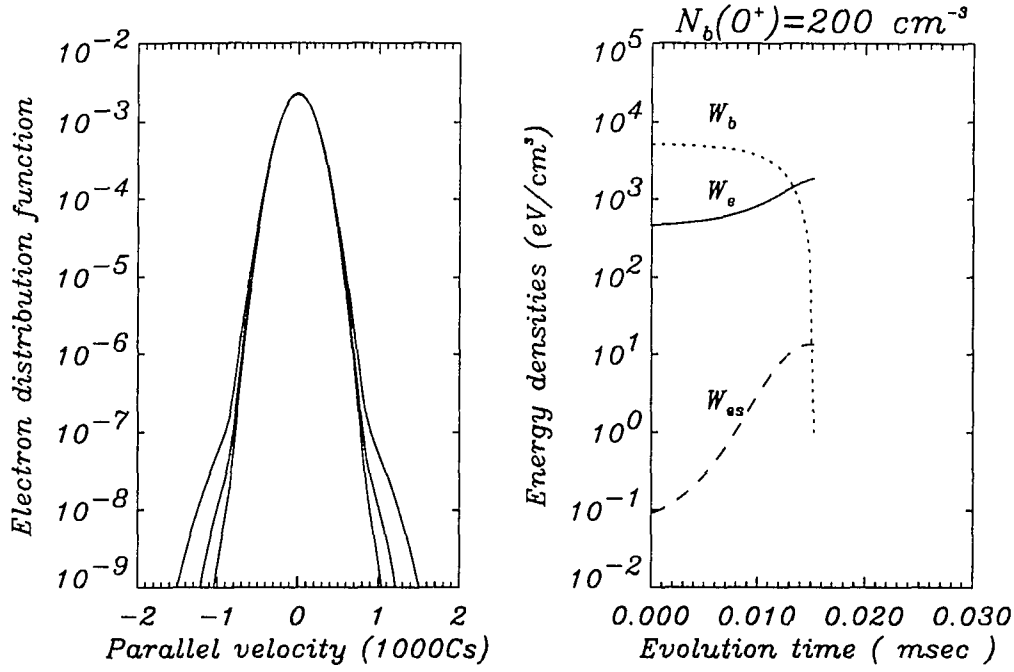

Figure 6.2: (a) Time evolution of electron distribution (left) and (b) energy density of hot electron (solid line), wave (broken lines) and ion beam (dotted line) for an oxygen ion beam with density $N(O^+) = 200\ cm^{-3}$. The velocity unit is the oxygen acoustic speed.

eV only. This corresponds to the electron CPA detector's low energy threshold. The wave energy density (broken line) indicates exponential like growth; it starts to saturate at 12 $msec$ (about 80 ω_{lho}) as soon as the available beam energy (dotted line) is used up. Another run for a barium beam with $n_b = 200\ cm^{-3}$ is shown in figure 6.3(a) and (b).

In this case the electron tail is significantly enhanced compared to the case of an oxygen beam. This is due to the fact that the kinetic energy is proportional to the mass, therefore more free energy will be available from the heavier barium than from the lighter oxygen for electron heating. For the same reason, the wave saturation

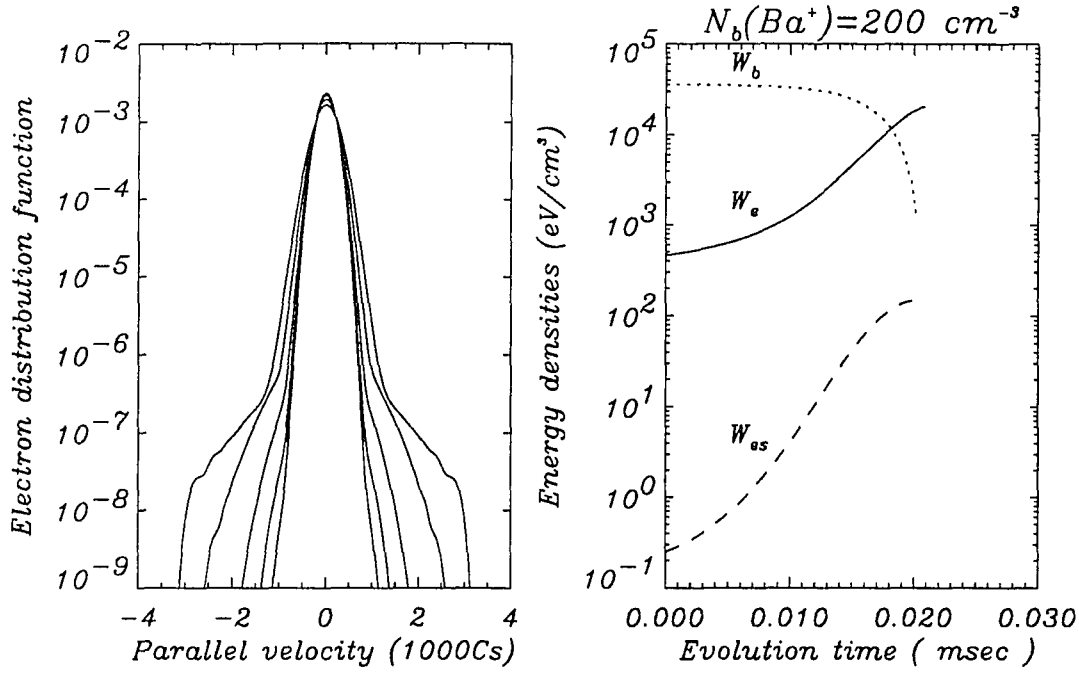

Figure 6.3: (a) Time evolution of electron distribution (left) and (b) energy density of hot electron (solid line), wave (broken lines) and ion beam (dotted line) for a barium ion beam with density $N(Ba^+) = 200\ cm^{-3}$. The velocity unit is the oxygen acoustic speed.

level is also higher. One thing that needs to be mentioned is that the oxygen distribution does not present any visible change in our calculation results. This could be due to the fact that the perpendicular beam velocity ($\sim 1.5 \times 10^6\ cm/sec$) is much greater than the thermal velocity of oxygens ($\sim 1.5 \times 10^5\ cm/sec$), thus resulting in a very weak Landau resonance effect on the oxygens.

A comparison between our model results and the observed data is shown in figure 6.4. The broken line denotes the electron energy density measured by the electron CPA detector and the two model results for oxygen and barium beam are expressed by solid lines but start from different times. In the case of the oxygen beam, it

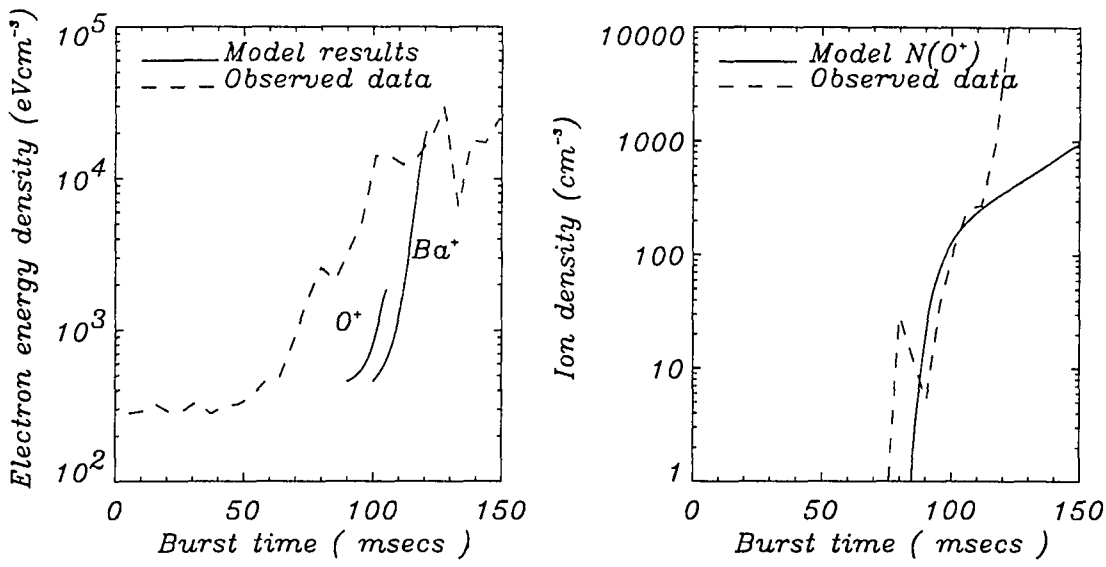

Figure 6.4: left: A comparison between model results and CRIT-II data. right: CRIT-II ion data (broken line) and neutral oxygen beam from model calculation. Ion density calculation is based on one species, barium, assumption.

starts at 0.09 seconds of release time (the time of $n_{o+} = 200\ cm^{-3}$ observed by the ion detector). Apparently, the electron energy density from our calculation is not enough to explain the measured electron data. On the other hand, the barium beam, with density $n_b = 200\ cm^{-3}$, which starts at 0.1 second of release time can produce a substantial amount of hot electron energy density comparable to the measured data at about 0.12 seconds or even earlier. It is believed that the barium beam average density could be as high as 500 cm^{-3} during the release time from 0.09 to 0.1 seconds, one can suggest that the barium beam could very likely be responsible for the electron heating during this time period.

In the lower hybrid instabilities electrons are energized preferentially along the magnetic field. However, this anisotropic feature of electron population was not observed by the electron CPA detector. It could have been that the isotropizing

process, probably due to electron collisions with neutral barium atoms, was more efficient than the lower hybrid heating in the ionosphere, or at least in the situation of CRIT-II.

It should be noted that the assumption of a nonrelaxed fast ion beam made in our model should introduce some unphysical results. Firstly, the relaxation time should be shorter and consequently the saturation level could be lower. Secondly, the ambient ions show no diffusion in our model result. However, if the ion beam is allowed to diffuse, then an ion beam tail will be formed towards the low velocity region where the ambient ion population is significant and consequently induce the Landau resonance. According to the above discussions, the results obtained from our model calculation such as hot electron tails density and energy should be considered as a high limit.

6.5 Conclusions

The electron heating due to the lower hybrid instabilities has been studied by utilizing the quasi-linear diffusion theory. It was found that electron heating and wave saturation is mainly due to the Landau resonant heating resulting in the formation of high electron energy tail, as soon as the available free energy from an ion beam is exhausted. The numerical results show that the energetic barium beam with density of 200 cm^{-3} can produce enough hot electrons to explain the observations. Also, the electron heating which took place earlier could be partially due to the precursor oxygen beam. However, both heatings by barium beam and oxygen beam cannot explain the very leading part of hot electrons starting from 0.05 seconds of release time observed by CRIT-II because no ion can arrive at the detector before 0.07 seconds.

This suggests that the electron heating has taken place earlier and then convected to the detector before any ion beam arrived. The lower hybrid heating has long been considered as the main heating mechanism in the CIV process. However it has never been confirmed by experiment either in laboratory or in space. Our investigation confirms that lower hybrid instability may be involved in the early stage of electron heating in the CRIT-II experiment.

This model can only be applied to the precursor wave region as a consequence of our basic assumption that waves are associated with lower hybrid instabilities. As shown by Swenson [1992], when the main, dense, barium beam arrived, the structure of waves changed dramatically. Therefore our lower hybrid heating model is not adequate and the electron heating should be involved in different kinds of wave instabilities. However, the same technique used in this report to study the quasi-linear diffusion can still be applicable as long as the dispersion relation of the waves is known.

CHAPTER 7

Low Frequency Plasma Waves

7.1 Introduction

The richness and variety of plasma waves observed by CRIT-II is probably one of the most striking outcomes since the first space CIV experiment was conducted. The success of this experiment enables scientists to study the possible dynamic processes associated with the ionospheric neutral beam-plasma interactions. As regards the main purpose of CRIT-II, it offers the evidence of the microscopic process for CIV.

The electric field measurements inside the barium beam cloud, according to Swenson *et al* [1990] , can be categorized into four distinct phases: the precursor waves, the growth phase, the saturated waves, and the turbulent (see figure 7.1).

The precursor waves were seen at the main payload before the arrival of the fastest barium neutrals. The frequency band of these waves is from 7 kHz, slightly above the ambient oxygen lower hybrid frequency, up to the detector's cutoff frequency at 16 kHz [Pfaff et al., 1992]. The precursor waves could be generated by a superfast oxygen ion beam as discussed in chapter 5. A similar feature of the precursor waves was also observed by Star of Condor [Kelley et al., 1986] and CRIT-I [Kelley et al., 1991]. The precursor waves have been studied in chapter 6 to explain the observed heated electrons in CRIT-II.

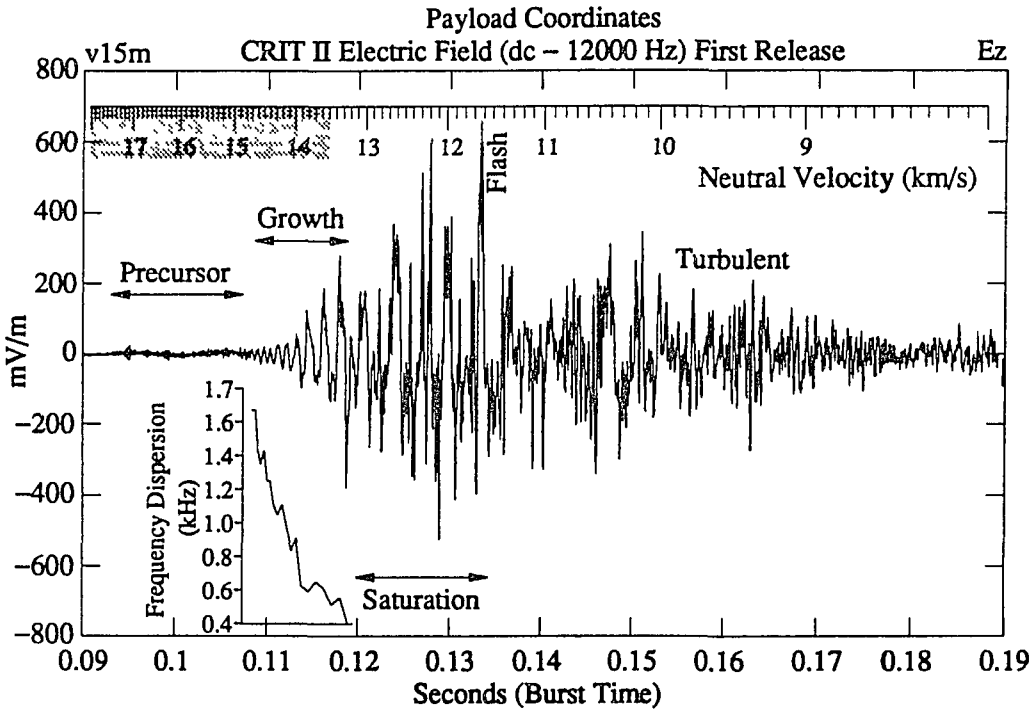

Figure 7.1: CRIT-II first release electric field data along the direction of the neutral stream. The velocity of the neutrals is noted at the top, and the frequency dispersion during the growth period is plotted and inset. (from Swenson, 1992).

The growth phase starts at about 0.108 seconds of burst time and continues to about 0.118 seconds. During this period, waves are growing significantly. The beginning of this period would correspond to the arrival of 14.7 km/sec particles from the release. It should be noted that according to the neutral barium velocity distribution model [Wescott et al., 1990], the fastest barium is expected to be produced at 13.5 km/sec and the density of barium with velocities greater than this would be very small. The ion detector, however, saw a moderately intensive ion beam with an energy band from about 25 eV to 100 eV at 0.105-0.110 seconds of burst time (see, for example, figure 3.6). It is believed that a fraction of these ions having energy below 40 eV could be the collisionally accelerated ionospheric neutral oxygens which charge exchange with ambient ions, and the ions with energy above 40 eV could be the byproducts of the shaped-charges and the tail of superfast barium combined. The linear growth phase is ended when the main dense barium beam arrives at the main payload.

The basic features of the waves in growth phase are that the frequency of unstable modes started at 1.6 kHz and gradually drops to 300 Hz over the linear growth phase, the wave polarization is near isotropic, the growth rate γ is about one-tenth of observed average frequency ω_0 [Swenson, 1992]. This is in conflict with the current CIV theory from which the lower hybrid instabilities are thought to play a crucial role in electron heating [Goertz et al., 1990; Galeev and Chabibrachmanov, 1983]. The wave frequency predicted by the lower hybrid instability theory for CRIT-II experiment would be around 7 kHz and growth rate would be $\sim (n_b/n_0)^{1/3}\omega_0 \sim 0.2\omega_0$, also the wave polarization would be highly anisotropic with wave vector mainly perpendicular to the ambient magnetic field. All the features of the observed waves

presented in the linear growth phase suggest that a different kind of mechanism other than the lower hybrid instabilities played a major role during this stage of the wave-particles dynamics.

The first theoretical attempt, maybe the only published one to date, to explain these unknown waves concerns the nonlinear lower hybrid wave instability, proposed by Papadopoulos [1992]. He pointed out that due to the finite width of the beam along the magnetic field the lower hybrid instability is a backward wave instability (*i.e.* the group and phase velocities are in opposite directions), hence the single wave field-aligned structure and the backward wave-packet nature of the unstable waves play a critical role in the evolution of wave particle interaction. He also argued that the wave-packet moves at group velocity $\mathbf{V}_g$ and the wave frequency in the rest frame of wave-packet is the usual lower hybrid frequency. Therefore the frequency ω_0 measured by a stationary probe in the ionosphere is given by

$$\omega_0 = \omega_{\mathbf{k}} + \mathbf{k} \cdot \mathbf{V}_g$$

where $\mathbf{V}_g$ and $\omega_{\mathbf{k}}$ are determined by the dispersion relation of usual lower hybrid waves, but the perpendicular wave number $k_\perp$ is determined from the self-similar solutions of collapsed lower hybrid solitary waves, assuming that the field aligned length is known.

However, it should be noted that this model is highly intuitive in fashion and thus is far from quantitatively developed. Also there is no measurement evidence to support the existence of this nonlinear collapsing of a solitary wave. In fact, Seyler [1993] reports that lower hybrid waves do not collapse. In this chapter, we will introduce a different kind of explanation based on the inhomogeneous and finite-width nature of the barium beam. A general linear wave dispersion relation for

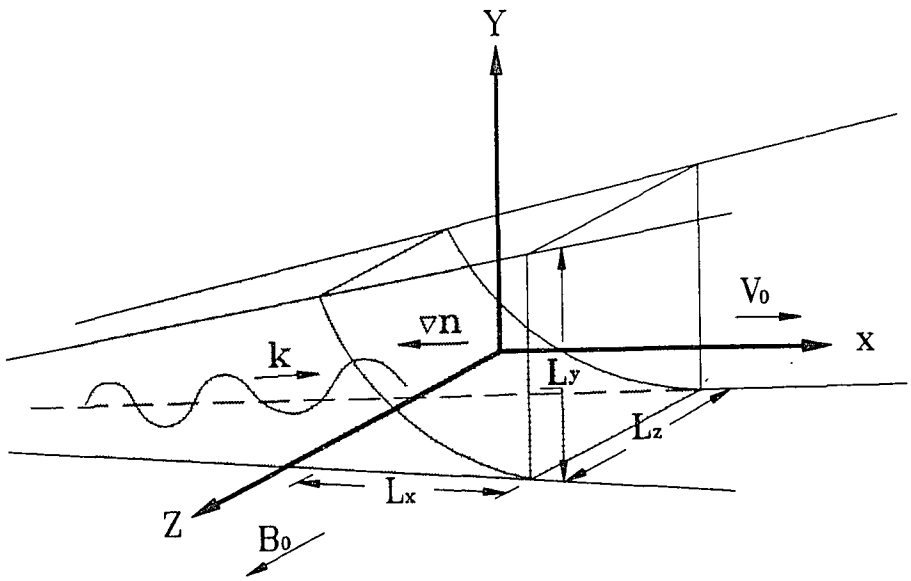

Figure 7.2: Configuration of the slab-shaped beam model.

an unmagnetized beam in a quasi-neutral magnetized plasma will be first derived from the multi-fluid theory. This dispersion relation will be solved in the parameter regimes where the CRIT-II experiment applied. Also, the change of growth rate of the lower hybrid waves due to the finite width beam effect will be investigated.

7.2 Dispersion Relation

To help derive the wave dispersion relation, several assumptions will be made in this model. First, a slab beam instead of a conical beam will be used. The width of the beam along the ambient magnetic field, $\mathbf{B}_0$, in z direction, is denoted by L_z (see figure 7.2). The origin of the z-axis is located at the center of the beam. The beam velocity, $\mathbf{V}_0$, is chosen to be perpendicular to $\mathbf{B}_0$ in x direction. The beam width, L_y, in y direction is perpendicular to both $\mathbf{V}_0$ and $\mathbf{B}_0$ and it is assumed to be much

larger than the wave number in this direction. Therefore, the boundary effect in the y direction can be ignored. Futhermore, the density of background ionospheric plasma is assumed to be homogeneous and infinite, but the density of the beam is inhomogeneous. With the use of multi-fluid approach, assuming cold plasma and beam, the governing equations for $\sigma - th$ species are given by

$$\frac{\partial n_\sigma}{\partial t} + \nabla \cdot (n_\sigma \mathbf{V}_\sigma) = 0 \tag{7.1}$$

$$\frac{\partial \mathbf{V}_\sigma}{\partial t} + \mathbf{V}_\sigma \cdot \nabla \mathbf{V}_\sigma = \frac{q_\sigma}{m_\sigma}\left(\mathbf{E} + \frac{1}{c}\mathbf{V}_\sigma \times \mathbf{B}_0\right) \tag{7.2}$$

Since the density of beam inside the slab is inhomogeneous in the plane perpendicular to the magnetic field, in order to linearize above equations, we further assume that the density inhomogeneity is only in x direction and k_x vary little over one wave length $\sim 1/k_x$. Under these assumptions, all the first order term can be represented in the form: $(\ )' \sim e^{i\mathbf{k}_\perp \cdot \mathbf{r}_\perp - i\omega t}$. Thus the perturbed density and velocity can be given by

$$n'_\sigma = -\frac{i}{\tilde{\omega}_\sigma}(n_{0\sigma} \nabla \cdot \mathbf{V}'_\sigma + \nabla n_{0\sigma} \cdot \mathbf{V}'_\sigma) \tag{7.3}$$

$$\mathbf{V}'_\sigma = -\frac{i}{\tilde{\omega}_\sigma}\left(\frac{q_\sigma}{m_\sigma}\mathbf{E}' + \mathbf{V}'_\sigma \times \mathbf{\Omega}\right) \tag{7.4}$$

where $\tilde{\omega}_\sigma = \omega - k_x V_{0\sigma}$ is the Doppler shifted frequency. Substituting equation (7.4) into equation (7.3) and assuming that the perturbation is electrostatic, we obtain the expression of perturbed density

$$n'_\sigma = -\frac{q_\sigma}{m_\sigma}\left\{\frac{\nabla_\perp \cdot (n_{0\sigma} \nabla_\perp \phi)}{\tilde{\omega}_\sigma^2 - \Omega_\sigma^2} + \frac{\nabla_{||} \cdot (n_{0\sigma} \nabla_{||} \phi)}{\tilde{\omega}_\sigma^2} + i\frac{\mathbf{\Omega}' \cdot (\nabla_\perp n_{0\sigma} \times \nabla_\perp \phi)}{\tilde{\omega}_\sigma(\tilde{\omega}_\sigma^2 - \Omega_\sigma^2)}\right\} \tag{7.5}$$

in which the first and second terms represent the density fluctuations due to the perturbed motion of the particles perpendicular and parallel to the magnetic field, respectively. Both terms are present even when $\nabla n_{0\sigma} = 0$. However, the third

term exists only if $\nabla n_{0\sigma} \neq 0$ and the perturbed electric field has a component at right angles to the density gradient and the background magnetic field. A nearly identical form of this perturbed density in inhomogeneous plasma has also been derived by Mikhailovskii [1974]. By using the equation (7.5) and after some algebraic manipulations, the Poisson's equation becomes

$$\frac{\partial}{\partial z}\left(\epsilon_{\parallel}\frac{\partial \phi}{\partial z}\right) - k_{\perp}^2 \epsilon_{\perp}\phi = 0 \tag{7.6}$$

in which

$$\epsilon_{\parallel} = 1 - \sum_{\sigma}\frac{\omega_{\sigma}^2}{\tilde{\omega}_{\sigma}^2} = \epsilon_{\parallel}^H \tag{7.7}$$

$$\epsilon_{\perp} = 1 - \sum_{\sigma}\frac{\omega_{\sigma}^2}{\tilde{\omega}_{\sigma}^2 - \Omega_{\sigma}^2} + i\sum_{\sigma}\frac{\omega_{\sigma}^2}{\tilde{\omega}_{\sigma}^2 - \Omega_{\sigma}^2}\frac{\kappa_{x\sigma}k_x}{k_{\perp}^2}\left(1 + i\frac{\Omega_{\sigma}}{\tilde{\omega}_{\sigma}}\frac{k_y}{k_x}\right) = \epsilon_{\perp}^H + \epsilon_{\perp}^N \tag{7.8}$$

where the superscript 'H' denotes the homogenous and 'N' the inhomogeneous, and $\kappa_{x\sigma} = n_{0\sigma}^{-1}\partial n_{0\sigma}/\partial x$. Note that the last term on the right hand side $\epsilon_{\perp}^N$ exists only if the inhomogeneity of density is present, *i.e.* $\kappa_x \neq 0$.

If the beam is infinitely wide in z direction, then we can use the substitution of ik_z for $\partial/\partial z$ in equation (7.6) and leads to

$$k_{\parallel}^2\epsilon_{\parallel} + k_{\perp}^2\epsilon_{\perp} = 0 \tag{7.9}$$

An identical dispersion relation has been derived by Möbius [1977] except for the difference in geometric configuration. If $\kappa_x = 0$, then the equation (7.6) is reduced to the dispersion relation for the usual homogeneous modified two stream instabilities [McBride et al., 1972; Möbius et al., 1987].

Equation (7.6) can be solved by WKB method if the density profile of the beam along the z-direction is known. To simplify this problem, we will assume that the beam density is uniform along the magnetic field. This will introduce a sharp boundary on both side of the beam along z-direction. Although this assumption is not

realistic, the effect of a finite beam width on the lower hybrid instabilities is still revealed. Accordingly, equation (7.6) can be easily solved for the outside and inside of a beam separately and their solutions can be matched at boundary with proper boundary conditions. In this approximation, the general solutions for our beam plasma system inside and outside the beam are

$$\phi^{in}(z) = A cosh\left(k_\perp \sqrt{\frac{\epsilon_\perp^{in}}{\epsilon_\parallel^{in}}} z\right) \tag{7.10}$$

$$\phi^{out}(z \geq L_\parallel/2) = B exp\left(-k_\perp \sqrt{\frac{\epsilon_\perp^{out}}{\epsilon_\parallel^{out}}} z\right) \tag{7.11}$$

where the superscripts "in" and "out" stand for inside and outside the barium beam, respectively, A and B are two constants and can be determined by boundary conditions. Also the symmetric and outgoing wave assumptions have been made for inside and outside solutions, respectively.

Since $\partial^2\phi/\partial z^2$ is finite, we would expect that the perturbed potential ϕ and its first derivative at boundary should be continuous, i, e,

$$\phi^{in}(z = L_\parallel/2) = \phi^{out}(z = L_\parallel/2) \tag{7.12}$$

$$\frac{\partial\phi^{in}}{\partial z}(z = L_\parallel/2) = \frac{\partial\phi^{out}}{\partial z}(z = L_\parallel/2) \tag{7.13}$$

Dispersion relation can be derived by applying the boundary conditions (7.12) and (7.13) into equation (7.10) and (7.11). After canceling A and B we obtain

$$\sqrt{\frac{\epsilon_\perp^{in}}{\epsilon_\parallel^{in}}} tanh\left(\frac{k_\perp L_\parallel}{2}\sqrt{\frac{\epsilon_\perp^{in}}{\epsilon_\parallel^{in}}}\right) = -\sqrt{\frac{\epsilon_\perp^{out}}{\epsilon_\parallel^{out}}} \tag{7.14}$$

This dispersion relation determines the relation between complex frequency, ω, and wave number, k. Owing to the complexity of this equation, an analytical analysis is impossible. We will solve this dispersion equation numerically and discuss its results in the following section.

7.3 Numerical Results and Discussions

In practical numerical calculation, we assume that the background plasma consists of electrons and oxygen ions. We also assume that the background oxygen ions are spatially uniform, *i.e.*$\kappa_{xo} = 0$, hence the plasma neutrality implies $\kappa_{xe} = (n_{0b}/n_{0e})\kappa_{xb}$. The dielectric constants in the dispersion relation are

$$\epsilon_{\|}^{in} = 1 - \frac{\omega_e^2}{\omega^2} - \frac{\omega_o^2}{\omega^2} - \frac{\omega_b^2}{(\omega - k_x V_0)^2} \tag{7.15}$$

$$\begin{aligned}\epsilon_{\perp}^{in} = 1 &+ \frac{\omega_e^2}{\Omega_e^2} - \frac{\omega_o^2}{\omega^2} - \frac{\omega_b^2}{(\omega - k_x V_0)^2} \\ &+ i\frac{\omega_b^2}{(\omega - k_x V_0)^2 - \Omega_b^2}\frac{\kappa_{xb} k_x}{k_\perp^2}\left(1 + i\frac{\Omega_b}{\omega - k_x V_0}\frac{k_y}{k_x}\right) \\ &+ i\frac{\omega_e^2}{\omega^2 - \Omega_e^2}\frac{\kappa_{xe} k_x}{k_\perp^2}\left(1 + i\frac{\Omega_e}{\omega}\frac{k_y}{k_x}\right)\end{aligned} \tag{7.16}$$

$$\epsilon_{\|}^{out} = 1 - \frac{\omega_e^2}{\omega^2} - \frac{\omega_o^2}{\omega^2} \tag{7.17}$$

$$\epsilon_{\perp}^{out} = 1 + \frac{\omega_e^2}{\Omega_e^2} - \frac{\omega_o^2}{\omega^2} \tag{7.18}$$

The parameters used for solving the dispersion relation are based on the observed data from CRIT-II. The plasma density $n_o = 5.41 \times 10^5\ cm^{-3}$, the beam velocity $V_0 = 1.4 \times 10^6\ cm/sec$, the beam density $n_b \sim 5 \times 10^3\ cm^{-3}$ and the maximum parallel beam width $L_{\|} = 500\ meters$ for burst one. The density for electrons is determined by plasma neutrality, *i.e.* $n_e \sim n_o + n_b$. The finite beam width effect on unstable waves will be studied first. In this case, the inhomogeneity of beam in the x direction will be ignored (*i.e.* $\kappa_x = 0$). In figure 7.3 wave frequencies and growth rates are solved and plotted against x-component wave length, λ_x, for 10 different values of $L_{\|}$ (from 100 to 1000 meters with 100 meters of increment). One can see that the wave frequencies are insensitive to the change of beam width. As long as $\lambda_x > 2\ m$, waves are characterized by beam mode ($\omega = kV_b$), while

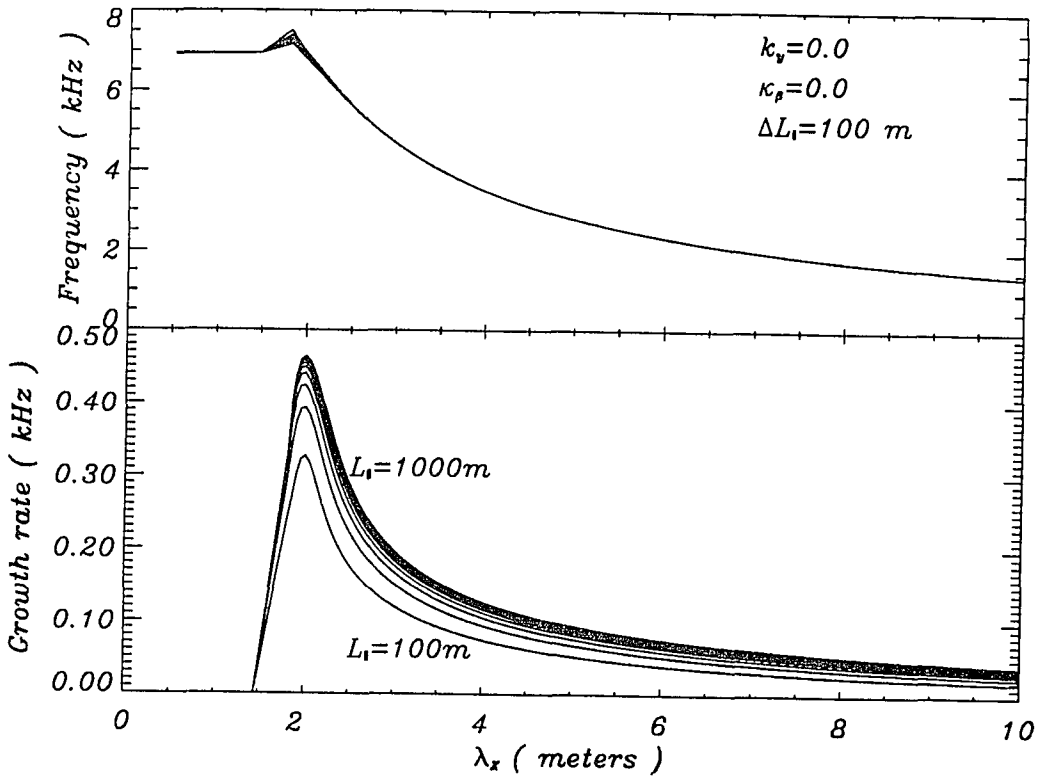

Figure 7.3: Unstable low frequency roots of the dispersion relation for a finite width unmagnetized barium beam in a cold, magnetized oxygen plasma. The frequency and growth rate for different parallel beam length are plotted.

$\lambda_x < 2\ m$, wave frequency approaches the lower hybrid plateau. However, the wave growth rate increases with increasing of $L_{||}$ and approaches the maximum growth rate at $L_{||} \sim 500\ m$; this is consistent with the theoretical prediction from the usual two stream instability. One should point out that, although the maximum growth rate decreases with decreasing parallel beam width, according to our calculation the maximum growth rate decrease is not substantial: One can see that a factor of 5 down from the maximum growth length results only 25 % decrease in growth rate.

In figure 7.4, wave frequencies and growth rates are solved and plotted against

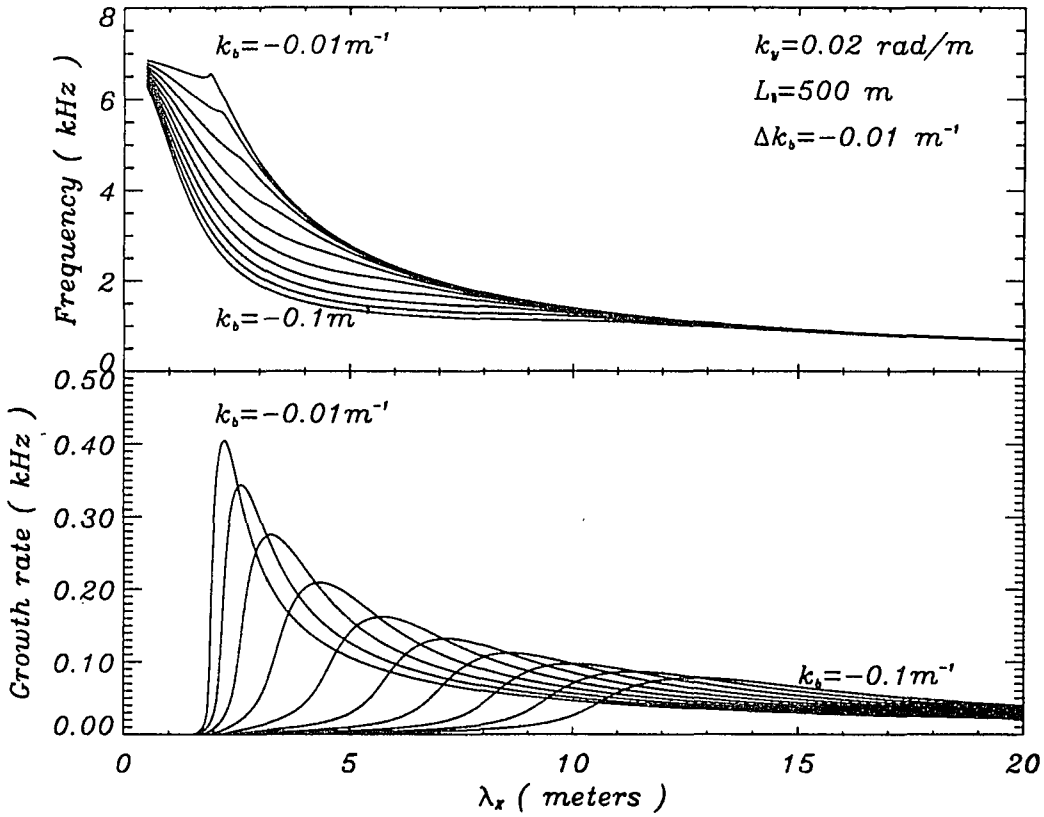

Figure 7.4: Unstable low frequency roots of the dispersion relation for a finite width unmagnetized barium beam in a cold, magnetized oxygen plasma. The frequency and growth rate for different beam inhomogeneities are plotted.

x-component wave length λ_x in ten steps of varying κ_{xb} from 0 to -0.1 m^{-1} with increment $\triangle\kappa_{xb} = -0.01\ m^{-1}$. The y-component of wave number, $k_y = 2\pi/\lambda_y$, is fixed at 0.02 rad/cm (about 3 meters). When the inhomogeneity of the beam is small, *i.e.* $\kappa_{xb} = -0.01\ m^{-1}$, the unstable wave behaves like a usual lower hybrid instability, and the wave growth rate peaks at about the lower hybrid frequency of ambient oxygens ($\sim 6.9\ kHz$). The wave maximum growth rate and its corresponding frequency decreases with the increasing of κ_{xb}; so does the wave length where the maximum growth is occurred. When $\kappa_{xb} = -0.1\ m^{-1}$, the wave frequency is

$\sim$ 1 kHz and the maximum growth rate is about 11 meters, which is about one-tenth of its corresponding frequency. The frequency band width, $\triangle f/f$, is about 0.1 for this unstable wave. These features are consistent with the observed wave data. Since the *in situ* measurement shows that the ion density increases with time and the density gradient of ion beam could be very high particularly during the linear growth phase, it ir very obvious to see that our results could explain why the wave frequency decreases with time.

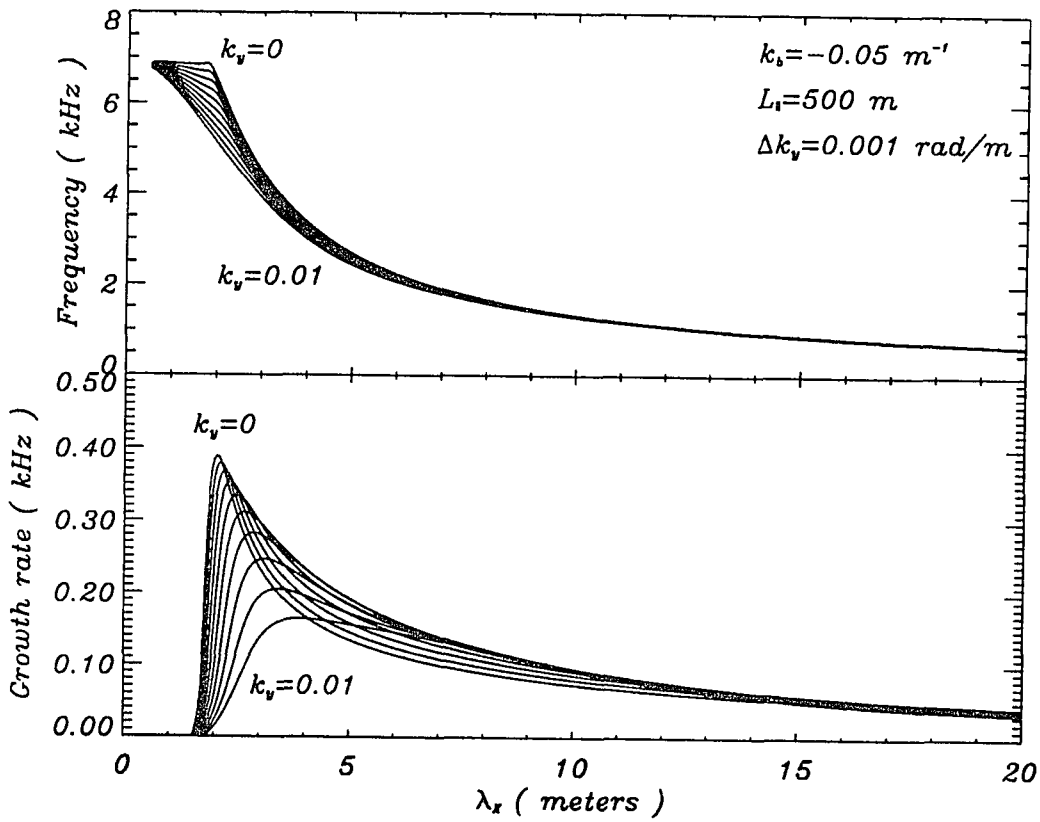

Figure 7.5: Unstable low frequency roots of the dispersion relation for a finite width unmagnetized barium beam in a cold, magnetized oxygen plasma. The frequency and growth rate for different wave numbers perpendicular to both the magnetic field and the direction of beam inhomogeneity.

As mentioned in the previous section, the density inhomogeneity is important only if the perturbed electric field has a component perpendicular to both magnetic field and density gradient. Since the inhomogeneity of beam is assumed in x-direction only, the perturbed electric field in y-direction should play a crucial role to the inhomogeneous effect. Therefore we also solve frequencies of unstable mode against λ_x for different k_y (from 0 to 0.01 rad/m) and the result is shown in figure 7.5. The parameters used are $\kappa_{xb} = -0.05\ m^{-1}$ and $L_{||} = 500$ meters. It is found that when $k_y = 0$ the unstable wave presents the usual lower hybrid instability as one would expect, and the $\lambda_{x,max}$ which corresponds to the maximum growth rate increases with the increasing of k_y hence resulting in reducing the wave frequency. When $k_y \geq 0.01\ rad/m$, however, the behavior of the maximum growth wave changes oppositely. From figure 7.5, the maximum growth rate and its corresponding frequency increase with k_y. This suggests another wave mode dominant at large k_y.

The relation between the wave frequency and the parallel beam length is also solved with $k_y = 0.02\ rad/m$, $\kappa_{xb} = -0.05\ m^{-1}$ and plotted in figure 7.6. The parallel beam width is varied from 100 to 1000 meters with increment $\triangle L_{||} = 100$ meters. The results show that the maximum growth rate decreases with increasing parallel beam width. This could be understood by the following explanation. Since the parallel wave length is about $2L_{||}$, and the condition for maximum growth for lower hybrid waves is $k_{||}/k \sim \sqrt{m_e/m_o}$, therefore increasing $L_{||}$, or decreasing $k_{||}$, will result in decreasing k_x, or equivalently increasing λ_x. However, the wave frequency corresponding to the maximum growth rate changes. This is in contradiction to the lower hybrid instability from which the wave frequency for the maximum growth is always near the lower hybrid frequency. Interestingly, if the barium is released

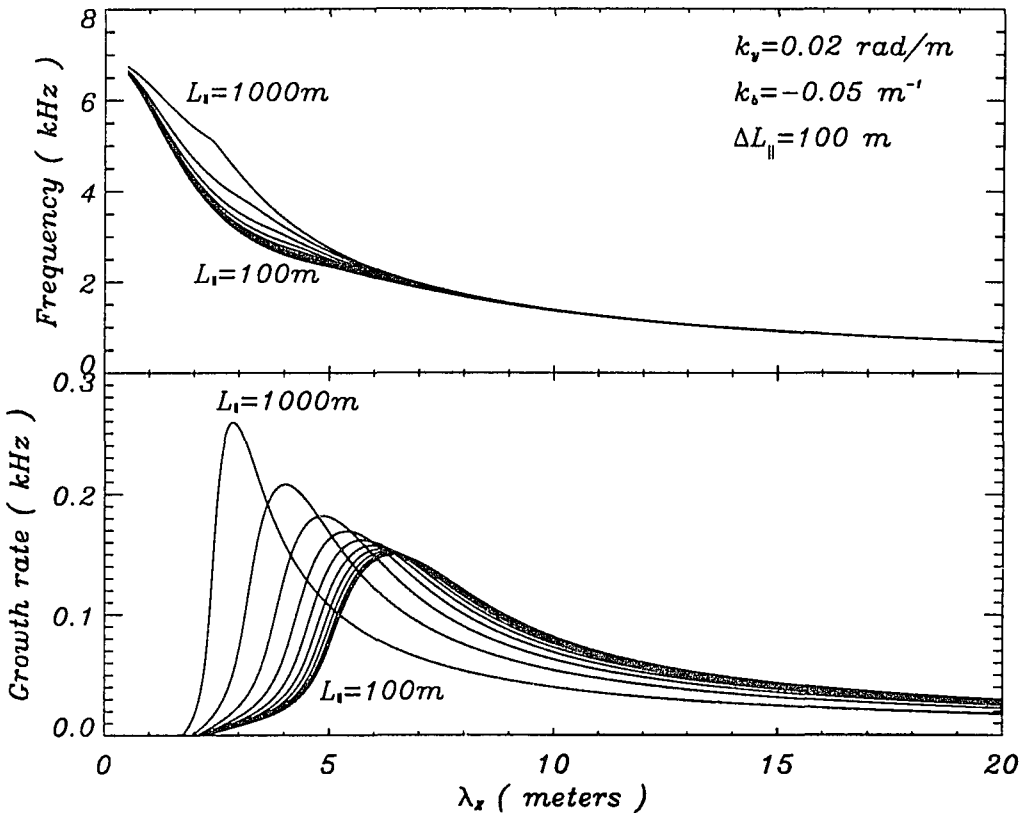

Figure 7.6: Unstable low frequency roots of the dispersion relation for a finite width unmagnetized barium beam in a cold, magnetized oxygen plasma. The frequency and growth rate for different parallel beam length

obliquely to the ambient magnetic field, it is reasonable to say that the parallel beam width will increase with time initially. The waves' frequency decreasing with time may be partially attributed to the parallel beam width.

7.4 Conclusion

In this chapter we have constructed a simple fluid model to derive the wave dispersion relation for an unmagnetized beam with finite width in a infinitely magnetized plasma. The dispersion relation has been solved numerically to investigate the fi-

nite width and inhomogeneous beam effect on the wave spectrum observed in the CRIT-II experiment. It was found that the unstable waves will be stabilized if the length of the beam parallel to the magnetic field is smaller than that of the fastest growing modes of the lower hybrid instabilities. We also found that the beam inhomogeneity could be responsible for the low frequency wave spectrum observed by CRIT-II. Although, as we know, the fluid model of lower hybrid instability is similar to the kinetic model, we are not sure whether the low frequency drift mode will be stabilized by Landau damping or not. We suggest that a kinetic model is needed to make a better interpretation.

CHAPTER 8

Quasi-DC Electric Fields

8.1 Introduction

Most of the space CIV experiments have involved the injection of a shaped-charge barium into the ionospheric plasma. Since the neutral barium beam has a finite width, when it moves across the magnetic field, a polarization electric field will be created inside the ionizing neutral cloud. To more specific, if an ionizing neutral beam moves in the x direction, the magnetic field, B_0, is along z, and if the beam is of finite extent in the y direction, there will be a Hall current, j_y, which leads to charge accumulation on the boundary creating a transverse electric field, E_y. This electric field will cause the ambient plasma undergoing the $E_y \times B$ drift across the magnetic field to reduce the relative velocity between the neutral beam and the plasma. If the accumulation of charge continues, this polarizing electric field can grow substantially and finally shut down the CIV effect. Moreover, the newly created massive ions in the beam cloud will leave the electrons behind and create a longitudinal electric field, E_x, which is anti-parallel to the beam direction at the leading edge of the neutral cloud. According to the ionizing front model [Piel et al., 1978], this longitudinal electric field is responsible for electrons performing the $E_x \times B$ drift transverse to the ambient magnetic field and driving the modified two stream instabilities to sustain

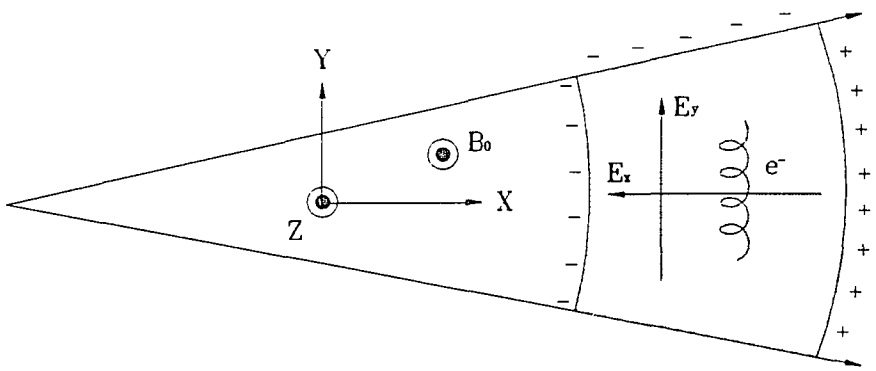

Figure 8.1: Perpendicular electric fields in a finite ionizing neutral beam.

the CIV effect (see figure 8.1).

Both longitudinal and transverse electric fields are created mainly by charge separation between ions and electrons within the beam cloud. Therefore, their characteristic time must be associated with the gyrofrequency of the ion beam. Since the ion beam atom is generally much heavier than the ambient oxygen ion, its gyroperiod is longer than that of oxygens. The term of quasi-DC will be referred to these electric fields. This type of finite-beam-width associated quasi-DC electric field has been observed in many space CIV experiments [Kelley et al., 1991; Swenson et al., 1990]. It is believed that the polarization electric field plays an important role in the momentum transfer in the space CIV experiment.

The way that a CIV effect can survive is that electrons obtain energy from the beam ions and then ionize more neutrals. Since electrons are massless and, in order to conserve momentum, the ambient plasma must absorb the momentum that is lost from the beam ions. The existence of a quasi-DC electric field enables the momentum exchange between the ambient plasma and the beam ions. Therefore, it is of importance to understand the electric field inside the cloud and it is one of

the keys to control the space CIV experiments. The purpose of this chapter is to provide a theoretical basis for the formation of the quasi-DC electric field in the shaped-charge release CIV experiments.

There are two previous works of interest under this concern. The transverse polarization electric field has been derived by the so-called "momentum coupling model" [Haerendel, 1982b]. According to this model, the momentum injection from a newly created ion is balanced by the Lorentz force. A dynamo current induced by the ion beam injections inside a magnetic flux tube will be closed by a polarization current associated with emitting Alfvén waves. The conservation of momentum inside a flux tube leads to a transverse electric field, which is characterized by the mass loading factor, λ_M, and is given by

$$\mathbf{E}_t = -\frac{\lambda_M}{1+\lambda_M}\frac{\mathbf{V}_b \times \mathbf{B}_0}{c} \tag{8.1}$$

and

$$\lambda_M = \frac{M_n \dot{n}_i L_{||}}{4\rho_a v_A} \tag{8.2}$$

where ρ_a is the mass density of ambient plasma and v_A is the Alfvén speed.

This momentum coupling model does not include the charge separation in the direction of beam and, therefore, can not predict the longitudinal electric field which is often seen in the space CIV experiments. Moreover, the deposited ions within the beam cloud are excluded. An identical result derived from a totally different approach was also given by [Torbert, 1987]. The basic idea of this model is to solve the closure of a current system within a beam cloud on the rest frame of the neutrals.

Another model of interest is the "barium swarm" [Brenning et al., 1991b]. In this model, the injected ions are considered but the neutral barium ionization rate is assumed to be zero. They also assumed that all the space charges are accumulated

on the surface of a cylinder-shape cloud. The rate of change of the electric fields is obtained by considering all types of currents generated in the cylinder cloud, including the ion dynamo current, ion displacement current, electron Hall current and field-aligned current associated with two Alfvén waves launching in both directions along B_0. They ended up with a quasi-steady-state solution as shown below

$$\mathbf{E} = -\frac{KB_0}{1+K^2}\frac{\mathbf{V}_\perp}{c} - \frac{K^2}{1+K^2}\frac{\mathbf{V}_\perp \times \mathbf{B}_0}{c} \tag{8.3}$$

where the parameter K is proportional to the cloud density and is defined by

$$K = \frac{\Delta n e \mu_0 v_A L_\parallel}{4B_0} \tag{8.4}$$

This quasi-steady electric field is entirely determined by this K parameter.

Although the barium swarm model predicts both longitudinal and transverse electric fields inside the barium cloud and does a better match on the electric field for the CRIT experiments, its biggest drawback is that it is not suitable for the case of low injected ions (low ion beam density) while the ionization rate is very high. On the contrary, the momentum coupling model is not appropriate for the case of low ionization efficiency while the injected ions are substantial. In this chapter, we will use a different approach given by Torbert [1987] to study this quasi-static electric field inside an ionizing neutral cloud. Both seeded ions and ionization rate will be considered to obtain a generalized form of static electric field and, most important, to explain the CRIT-II measurements.

8.2 Model Description

In this model, we assume that a neutral barium beam is injected into the ionospheric plasma. All types of collisions will be ignored as well as the expansion of the neutral

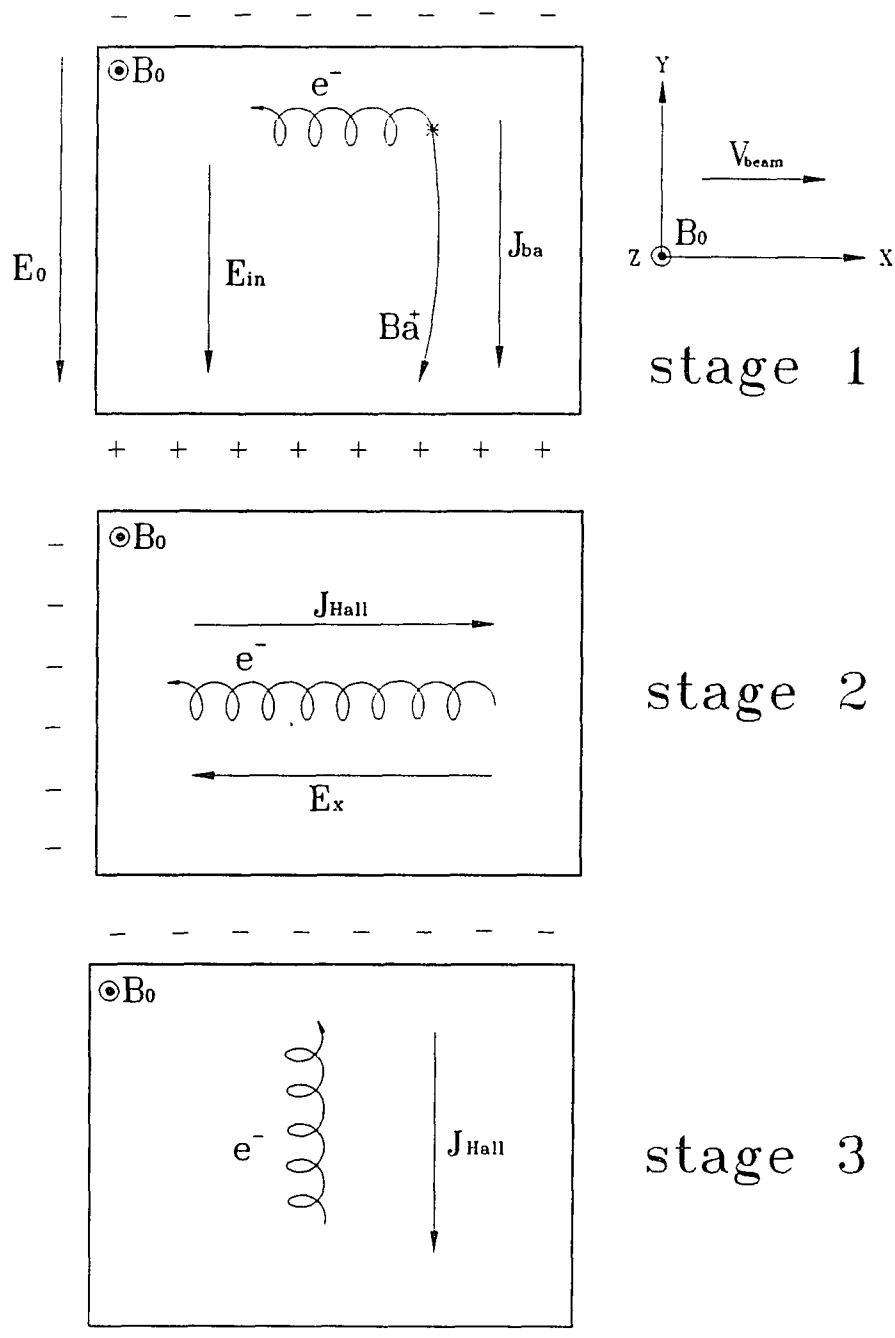

Figure 8.2: Schematic current system and associated electric field inside an ionizing cloud in the neutral frame of reference: (a) direct ion current and retarding electric field, (b) electron Hall current induced by retarding electric field, which polarize the beam cloud, and (c) electron Hall current created by polarization electric field.

cloud. The beam velocity is chosen to be in the x direction and the ambient magnetic field, B_0, in the z direction. The ionizing beam cloud is highly simplified by a parallel square-pipe with length $L_{||}$ along the magnetic field line and a cross section area $L_x \times L_y$ in the plane perpendicular to B_0. The reference frame is considered to be in the rest frame of the neutral beam so that all the neutral bariums are initially stationary and the ambient plasma will be moving at the neutral beam speed in the negative x direction. This would imply a convecting electric field $E_0 = V_b B_0/c$ in the negative y direction due to the motion of plasma across the magnetic field. A systematic diagram describing above processes is shown in figure 8.2(a) - (c).

Once a neutral barium atom is ionized (stage 1), the electric field, $\mathbf{E}_0$, will accelerate the ion in the -y direction and the electron in the opposite direction. Since electrons are fully magnetized and the heavy barium ions are effectively unmagnetized, the newly created ions will leave the electrons behind and create a current density $j_{ba} = \dot{n}_i e \rho_L$ in the same direction as $\mathbf{E}_0$, where ρ_L is the barium ion gyroradius. The ion-electron separation , up to one gyro-radii of barium, will result in a slowly oscillating electric field pointing along $\hat{y}$, which essentially is to reduce the initial electric field $\mathbf{E}_0$. At the same moment (stage 2), a Hall current density, $j_{hall} = \Delta n e c E_y/B_0$, will be created inside the neutral cloud in the x direction due to excess electrons, Δn, performing the $E_y \times B_0$ drift in the -x direction. These drifting electrons will be accumulated on the left boundary to polarize the neutral cloud and create a new electric field E_x -$\hat{x}$. Due to this electric field (stage 3), the ambient plasma will undergo the $E_x \times B$ drift in the y direction but create no current, only the excess electrons can contribute a Hall current density, $j_{hall} = \Delta n e c E_y/B_0$. Again these Hall current electrons will charge up the top side boundary to create an

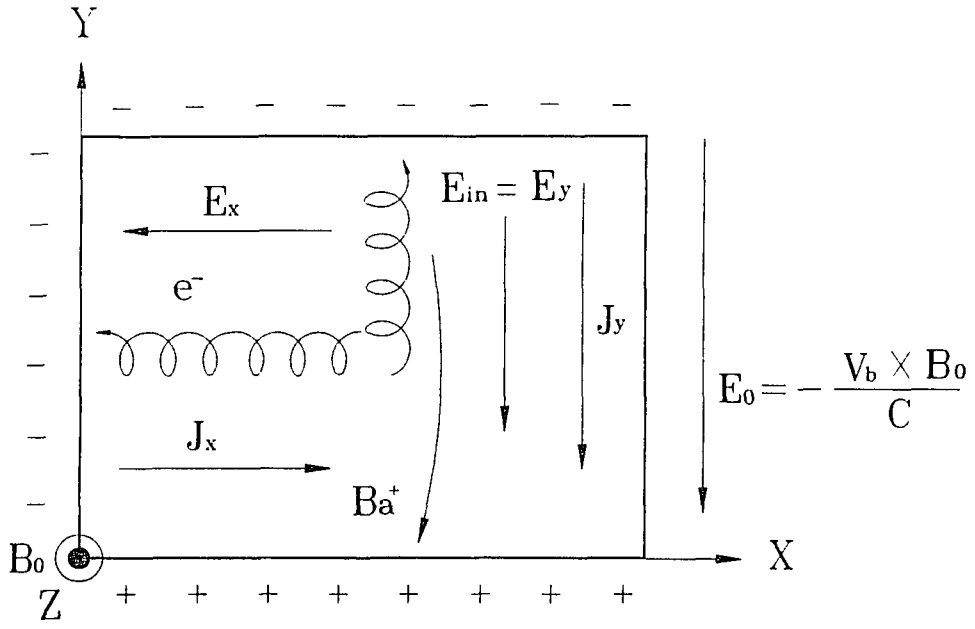

Figure 8.3: System currents and electric fields within an ionizing cloud in the neutral frame of reference.

electric field and reduce the original electric field $\mathbf{E}_0$. If there is no current drain, this process of charge accumulation will continue until the electric field inside the cloud is reduced to zero.

The system current density and electric field within the neutral cloud is given by adding the total currents and electric fields described above and is illustrated in figure 8.3. After summing up all the current sources, one finds the relations between the system current density and electric field

$$j_x = -\frac{\Delta n e c E_y}{B_0} \tag{8.5}$$

$$j_y = \dot{n}_i e \rho_L + \frac{\Delta n e c E_x}{B_0} = \frac{\dot{n}_i M c^2}{B_0^2} E_y + \frac{\Delta n e c E_x}{B_0} \tag{8.6}$$

Futhermore, we assume that the current density is uniform within the ionizing neutral cloud, thus the system current can be obtained by multiplying the current

density by the area which it passes through, *i.e.*

$$I_x = -\frac{\Delta necE_y}{B_0} L_y L_{||} \tag{8.7}$$

$$I_y = \frac{\dot{n}_i M c^2 E_y}{B_0^2} L_x L_{||} + \frac{\Delta necE_x}{B_0} L_x L_{||} \tag{8.8}$$

As mentioned previously, the current I_y will be accumulated on the cloud boundary to reduce the electric field E_y, which is equal to E_0 initially, and consequently reduce the velocity of the background moving plasma. In order to maintain charge neutrality, the ambient plasma must drain up the excess electrons or supply electrons to neutralize any charge unbalance inside the ionizing neutral cloud. This process is accomplished by field-aligned currents, *i.e.* emitting two shear Alfvén waves from each side of the cloud along the magnetic field line as illustrated in figure 8.4. The field-aligned currents can be calculated by combining the Ampere's law and Faraday's law with the displacement current neglected. After eliminating B one obtains

$$\frac{\partial \mathbf{J}}{\partial t} = -\frac{c^2}{4\pi} \bigtriangledown \times \bigtriangledown \times \mathbf{E} \tag{8.9}$$

The z component, assuming E_z=0, is

$$\frac{\partial j_z}{\partial t} = -\frac{c^2}{4\pi} \frac{\partial}{\partial z} \left(\frac{\partial E_x}{\partial x} + \frac{\partial E_y}{\partial y} \right) \tag{8.10}$$

Knowing that two Alfvén waves will be emitted in either direction along the magnetic field line, the combination of the time and spatial derivative can be replaced by the Alfvén velocity to give

$$j_z = \Sigma_A \left(\frac{\partial E_x}{\partial x} + \frac{\partial E_y}{\partial y} \right) \tag{8.11}$$

where $\Sigma_A = c^2/4\pi v_A$ is the Alfvén conductivity. Thus

$$\begin{aligned} I_{||} &= \int \Sigma_A \left(\frac{\partial E_x}{\partial x} + \frac{\partial E_y}{\partial y} \right) dxdy \\ &= \Sigma_A L_y E_x + \Sigma_A L_x (E_0 - E_y) = I_{||x} + I_{||y} \end{aligned} \tag{8.12}$$

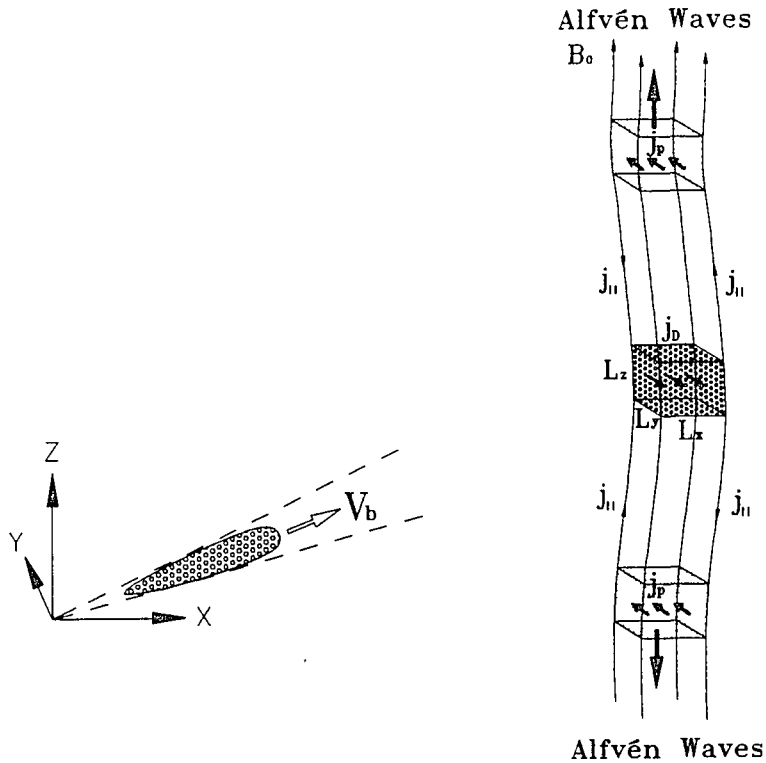

Figure 8.4: Configuration of a neutral beam interaction with the ionospheric plasma. Bending of the magnetic field line is due to the ionizing barium mass injection.

The electric field inside the cloud is given from an analogy of parallel charged plates on the x and y boundaries in a dielectric media, *i.e.* the ionospheric plasma, one has

$$E_x = \frac{4\pi}{\epsilon}\frac{Q_x}{L_y L_{||}} \tag{8.13}$$

$$E_y = E_0 - \frac{8\pi}{\epsilon}\frac{Q_y}{L_x L_{||}} \tag{8.14}$$

where $\epsilon = 1 + \omega_{o+}^2/\Omega_{o+}^2$ is the dielectric constant of the ionospheric plasma, Q_x and Q_y are the total charges on the bottom and left plates, respectively. We also have assumed that an equal amount of negative charges was built up on the top plate. These surface charges can be eliminated by applying the conservation of the total

charges to the system, this gives

$$\dot{Q}_x = I_x - 2I_{Ax} = \frac{\Delta n e c L_y L_{||}}{B_0} E_y - 2L_y \Sigma_A E_x \tag{8.15}$$

$$\dot{Q}_y = I_y - 2I_{Ay} = \frac{\dot{n}_i M c^2 L_x L_{||}}{B_0^2} E_y + \frac{\Delta n e c L_x L_{||}}{B_0} E_x - 2L_y \Sigma_A (E_0 - E_y) \tag{8.16}$$

in which a factor of 2 on the I_As is due to the fact that two Alfvén waves will be emitted. A system equation for the time dependent electric fields inside a neutral cloud can be obtained by taking the time derivative of equations (8.13) and (8.14) and combining with equations (8.15) and (8.16) to delete the charge terms. After some algebraic manipulations, one has

$$\gamma \dot{E}_x = -E_x + \kappa E_y \tag{8.17}$$

$$\frac{\gamma}{2} \dot{E}_y = -\kappa E_x - (1 + \lambda_M) E_y + E_0 \tag{8.18}$$

where the parameter $\gamma = L_{||}\epsilon / 8\pi\Sigma_A = (\epsilon/2)(L_{||} v_A / c^2)$ has a unit of time, the parameter $\kappa = L_{||}\Delta n e c / 2B_0\Sigma_A$ is dimensionless and is identical to the barium swarm's K factor [Brenning et al., 1991b] except a factor of 2 smaller. This discrepancy could be due to different assumptions for the cloud geometry made in the two models. The parameter λ_M is the mass loading factor [Haerendel, 1982a; Torbert, 1987]. A quasi-static solution can be obtained algebraically by setting the time derivatives on the left hand side of equations (8.17) and (8.18) to be zero. One has

$$E_{0x} = \frac{\kappa}{1 + \lambda_M + \kappa^2} E_0 \tag{8.19}$$

$$E_{0y} = \frac{1}{1 + \lambda_M + \kappa^2} E_0 \tag{8.20}$$

transforming back to the plasma reference frame, the electric field, in a vector form, becomes

$$\mathbf{E} = -\frac{\kappa}{1 + \lambda_M + \kappa^2} \frac{B_0}{c} \mathbf{V}_b - \frac{\lambda_M + \kappa^2}{1 + \lambda_M + \kappa^2} \frac{\mathbf{V}_b \times \mathbf{B}_0}{c} \tag{8.21}$$

The first term on the right hand side of equation (8.21) is the longitudinal electric field, which is anti-parallel to $\mathbf{V}_b$, the second term is the transverse electric field with respect to $\mathbf{V}_b$. The difference between this model result, equation (8.21), and others, equation (8.1) and equation (8.3), is obvious. Equation (8.21) essentially is a combination of the two results from the momentum coupling and the barium swarm models. The quasi-DC electric field is now determined by the mass loading factor, λ_M, and the κ parameter. When κ=0, only the transverse electric field exits and it is identical to equation (8.1), the momentum coupling model result. On the other hand, when $\lambda_M = 0$, it reduces to equation (8.3), the barium swarm model result. A similar result derived from a "generalized momentum balance model" was presented as a seminar by Haerendel in the physics department of UNH in 1992. However, we found an error in sign was made in his momentum equation, which turns out a different solution and is inconsistent with the direction of the observed electric fields.

Equations (8.17) and (8.18) can be solved if all the related parameters are independent of time. Therefore, the characteristic time τ_{DC}, a time required to build up the static electric field, can be found to be $\sim \gamma$. This γ parameter has a physical meaning associated with the Alfvén waves. The plasma dielectric constant can be rewritten as $\epsilon = 1 + c^2/v_A^2$. In the ionospheric plasma the Alfvén speed is much less than the speed of the light, therefore the vacuum term can be neglected from the dielectric constant. After some reductions the characteristic time has the form of $\tau_{DC} \sim \gamma \sim (L_{||}/2)/v_A$. It means that the time required to reach a static electric field is about the same as the time needed for two emitted Alfvén waves covering the whole range of cloud area, *i.e.* $L_{||}$, or each Alfvén wave covers the range of $L_{||}/2$.

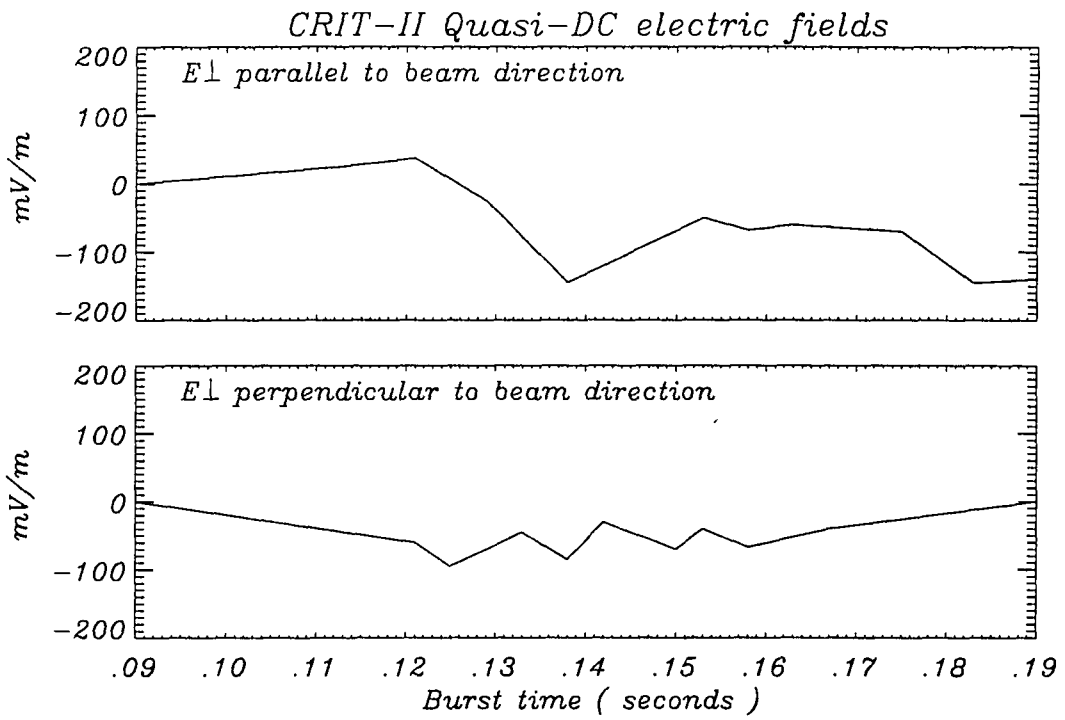

Figure 8.5: Perpendicular component of quasi-DC electric field, $E_\perp$ (0 - 60Hz), in the magnetic coordinates (after Swenson, 1992).

8.3 Applications

The observed quasi-DC electric field on CRIT-II for burst one is shown in figure 8.5. The top panel presents the longitudinal electric field, E_l, and the bottom one presents the transverse electric field, E_t. One can see that before 0.125 seconds (the arrival time for the main barium beam), E_l was rather stable and close to zero while E_t was growing up steadily to 70 mV/m (near its maximum). This could be understood from our model result. Since at this time there were few deposited barium ions, but the ionization rate could be very high and it would increase with the increasing of the barium neutral density, this gives a small value

of κ but a large value of λ_M. One would expect that E_l (proportional to Δn_i) is small while E_t (proportional to $\dot{n}_i$) would be increasing with time. During the passage of the main barium cloud, both E_l and E_t reach their maximum value at about 100 mV/m and 80 mV/m, respectively. For a given λ_M (proportional to $\dot{n}_i$) and κ (proportional to Δn_i), this characteristic value of quasi-static electric field measured by CRIT-II can be calculated from equation (8.21). To estimate the λ_M and κ parameters, the barium beam and plasma parameters are taken from Table 3.1, Δn and $\dot{n}$ will be estimated by using the RF plasma density profile illustrated in figure 3.5. The choice of Δn and $\dot{n}_i$ is somehow flexible and leaves an uncertainty to our estimations. The characteristic values were estimated giving $\Delta n = 5 \times 10^5\ cm^{-3}$ and $\dot{n}_i = 9 \times 10^6\ /cm^3 sec$ for burst one. This gives $\lambda_M = 0.12$ and $\kappa = 0.19$ or $E_l = 82\ mV/m$ and $E_p = 68\ mV/m$. They are smaller than the observation data by about 20 % and are reasonably consistent with the observations. For burst two, however, the electric field data has not been fully analyzed and published at this time.

From the energy point of view, the condition to sustain the CIV ionization effect is

$$\eta_e \frac{1}{2} M \left(\frac{cE_{in}}{B} \right)^2 \geq e\phi_{ion} + e\phi_{exc} \tag{8.22}$$

where η_e is a fraction of ion beam energy being converted to electron energy, ϕ_{ion} and ϕ_{exc} are the ionization and the excitation potential for the barium atoms, respectively. Newell and Torbert [Newell and Torbert, 1985] pointed out that in the electron impact collisions about 50 % of the hot electron energy will be wasted to the barium line excitation. Therefore a double amount of ionization energy is needed in average to ionize one barium atom. Substituting equation (8.21) into equation

(8.22), one has

$$\eta_e \geq (1 + \lambda_M + \kappa^2)^2 \frac{4e\phi_{ion}}{Mv_b^2} \tag{8.23}$$

Since both λ_M and κ are inversely proportional to the ambient plasma density, in a higher (lower) density plasma the threshold for the electron heating efficiency to sustain the CIV ionization would be lower (higher). This could be the reason why the barium ionization yield was relative high in Porcupine [Haerendel, 1982b] and CRIT-II [Stenbaek-Nielsen et al., 1990b] compared to Star of Lima [Wescott et al., 1986a] and CRIT-I [Stenbaek-Nielsen et al., 1990a]. For a typical beam velocity of 10 km/sec, one finds that $\eta_e \geq 0.13$. Thus it requires 13 % of beam energy transfer to maintain the CIV effect. This is not physically impossible because the theoretical value for the maximum η_e is 2/3 [Formisano et al., 1982]. An analysis from the electron CPA data shows that the average hot electron energy density was about 4-5 % of total energy density of beam ions. However, this ratio was much higher (greater than 20 %) during the linear growth region. This indicates that the CIV effect did exist and was not totally quenched by the law of the momentum conservation. Therefore the question is not to doubt if the CIV effect can take place in space but why most of the space CIV experiments have yielded so little neutral ionizations.

From equation (8.23), one can find the threshold velocity for CIV to occur as

$$v_b \geq v_{thr} = (1 + \lambda_M + \kappa^2)\sqrt{\frac{2}{\eta_e}} v_c \tag{8.24}$$

where $v_c = \sqrt{2e\phi_{ion}/M}$ is the Alfvén's critical ionization velocity. For a fixed η_e, the CIV threshold velocity increases with the increasing of the ionization rate and the density of deposited ions. This implies that the CIV effect in a finite width beam is a self-limited ionization process. On CRIT-II, the perpendicular velocity of the barium beam was up to $3.4v_c$, if $\eta_e = 0.5$, therefore v_b must greater than

$2(1 + \lambda_M + \kappa^2)\nu_c$ or equivalently $\lambda_M + \kappa^2 \leq 0.7$. This condition could be violated during the growth phase where the ionization rate could be very high such that $\lambda_M \geq 0.7$. Furthermore, if $\eta_e = 0.25$, $\lambda_M + \kappa^2$ must be less than 0.2. This condition is reasonably consistent with the CRIT-II data during the active region.

To briefly summarize this chapter, a simple barium cloud model has been developed for studying the quasi-DC electric field inside a neutral barium cloud. Our model result is essentially a combination of the results from the momentum coupling and the barium swarm model. The prediction of the static electric field from our model is reasonably consistent with the observations on CRIT-II. Also, we have further demonstrated that the CIV effect could have taken place in CRIT-II. However, due to the momentum balance requirement, the space CIV is a self-limited ionization process. This could have resulted in low ionization yields in most of the space CIV experiments.

CHAPTER 9

Summary, Recommendations, and Conclusions

9.1 Summary of Original Work

The CRIT-II experiment was probably the most elaborate sounding rocket to date to investigate the Alfvén's CIV effect in space. A rich amount of particle data from CRIT-II has been analyzed and presented in this thesis. The most exciting result from CRIT-II is that some of the essential features predicted by the CIV theories such as plasma density enhancement, anomalous energy and momentum loss from fast ion beams, excitation of plasma waves, and electron heating, were measured. However, the total ionization yield of neutral barium was not convincingly high as predicted by the CIV hypothesis (up to only 4% of neutral barium atoms were ionized by CIV ionization mechanism [Stenbaek-Nielsen et al., 1990a]).

Theoretical models, which comprise half of this thesis, have been developed to interpret the observed phenomena and to understand why the CIV effect did operate but at such a low level. The fundamental results of these models are summarized as follows.

In chapter 4 the charge exchange cross section for the atomic barium with the oxygen ion was calculated and found to range from about $1 \times 10^{-17}\ cm^{-2}$ at velocity

of 4 km/s to about 1×10^{-15} cm^{-2} at velocity of 20 km/s. It should be noted that this charge exchange cross section varies widely over the velocity ranges at which most of the space CIV experiments were conducted. Therefore, the charge exchange ionization process should be carefully investigated case by case in every space CIV experiment. Our barium density model showed that hot electrons observed by the CPA detector were responsible for about 45 % of the barium ion production observed by the ESA detector in the first release. In the second release, however, this percentage was reduced to 25 %. We suspect this difference between the two releases is due to the over estimated payload-release separation. According to our model result, the $(Ba - O^+)$ charge exchange ionization could be responsible for the rest of the barium ion production observed by the ion detector.

An elastic collision model has been developed in Chapter 5. It confirmed that the precursor ions originated from the collisionally accelerated neutral oxygen which underwent charge exchange with the local oxygen ions. In the precursor region, lower hybrid waves and heated electrons were also observed. It is believed that the precursor ions were important for the preheating of electrons and the triggering of CIV anomalous ionization. In chapter 6, we employed the quasi-linear theory to investigate the possible sources for the preheated electrons observed by the CPA detector. It was found that the heated electrons were created locally by the lower hybrid instabilities, induced by a thin barium beam; but only later when barium arrives.

In chapter 7, a multi-fluid dispersion relation which describes linear waves excited by an unmagnetized ion beam with finite width in a magnetized plasma was derived to interpret low frequency waves observed in the linear growth region. The finite

parallel length of an injecting beam, which could suppress the growth rate of the LHI, has long been suspected as one of the main reasons resulting in a low ionization yield in many space CIV injection experiments. However, we found that the maximum growth rate of the lower hybrid instability is not very sensitive to the parallel length, at least in the case of CRIT-II. We also found that the inhomogeneous beam effect could be the main driver which altered the plasma wave spectrum from the typical lower hybrid waves predicted by the homogeneous beam-plasma theory.

Finally, Chapter 8 studied the momentum coupling between an ionizing neutral cloud and the ionospheric plasma. A DC electric field model based on the closure of a current system in an ionizing neutral cloud was developed. According to the assumption of the critical ionization velocity, equation (1.1), from which the CIV effect can occur, we found that the self-polarizing effect occurring in the ionizing cloud could have quenched the CIV's anomalous ionization in the CRIT-II experiment. Therefore we concluded that the ionization during CRIT-II might have been self-limited due to the conservation of momentum.

9.2 Conclusions and Recommendations

Although repeatedly confirmed by numerous laboratory experiments under a wide variety of conditions, the hypothesis of Alfvén's critical ionization velocity effect has not yet been successfully produced in space. The controversy between the laboratory and space experiments has put the CIV concept in doubt. On the other hand, the space CIV may have existed in each experiment and perhaps, ghost-like, escaped from the measurements. Also, it could be due to the lack of a comprehensive theory which can identify the CIV process from each of the CIV experiments.

There is only one barium injection experiment, Porcupine [Haerendel, 1982a], to date which offers compelling evidence that the CIV effect can occur in space plasma. The CRIT-II experiment was conducted in a high plasma density region, which is similar to that in Porcupine, to maximize the efficiency of the CIV effect, but only 4% of ionization yield was observed, a factor of 7-8 smaller than that observed by Porcupine. A comparison of CRIT-II and Porcupine with other very low ionization yield CIV experiments, high plasma density seems to be a necessary condition to achieve a substantial ionization yield. However the discrepancy between CRIT-II and Porcupine still remains unexplained and the lack of the *in situ* measurement on Porcupine makes it impossible to compare two experiments in detail. In light of the success of CRIT-II, we hope that another similar CIV experiment will be conducted in the near future to extend to a wider parameter regime. However, no experiment is perfect and CRIT-II is no exception. Based on the CRIT-II experiment and this thesis work, several improvements in the payload instrumentation design and the experimental concept are recommended for a better performance in a future CIV experiment. They are summarized as follows.

(1) Attitude control system provides information on the orientation of the instrumented payloads relative to the injecting beam. It plays a crucial role to the chemical injection related CIV experiments since an error in ACS could result in a failed experiment. We suggest a reliable attitude gyro or a star sensor should be used in the next flight.

(2) The CRIT-II experiment was carried out at dusk at altitude about 100 *km* under the neutral barium solar fluorescent emission line of 4554 Å. It was found that both green (6300 Å) and red (5535 Å) photometers were exposed to sunlight,

which made a quantitative analysis of the photometer data very difficult or even impossible. We suggest that a more reliable calculation for the barium screen height is needed. Also the 6300 Å oxygen excitation line has about 120 seconds of life time, and is therefore not a good candidate for observing the short time features of the CIV process. We suggest that the short-lived oxygen excitation line ($^1S - ^3P$) at 2959 Å will be desirable.

(3) The electron ESA detector was over saturated due to an excess electron flux in the active period. We suggest a modified version of the ESA, for example the SESA (a shrunk version of ESA and with smaller geometric factor), or a pair MCP with higher strip current capability, like those used on the CPA detector, can avoid this problem. In addition to this, the advantage of the SESA is its smaller structure which is capable of measuring the electron energy down to 0.1 eV. Since only one pair of MCP is needed on the SESA compared to five pairs of MCP used on ESA, this will largely cut down the cost of the detector.

(4) Since the structure of the injected beam in the Earth's magnetic field is neither isotropic nor gyrotropic, a detector which is capable of three dimensional measurement will be desirable in order to determine the distribution of the beam ions. This can be implemented by opening the acceptance angle of the ESA detector to 2π. However, in order to keep the time resolution of measurement as high as that in CRIT-II, a super fast sweeping rate will be required, which is much costlier. Another way to approach this is through the coupled use of the same ESA detector and a scheme for imaging the spatial location of the beam particles.

(5) We have shown in chapter 3 that a fraction of the ions measured by the ion detector was oxygen which could mimic the barium ions and makes data interpretation

difficult. Therefore, a mass spectrometer will be helpful.

(6) During the passage of main barium beam, a steady growing low frequency (less than the lower hybrid frequency of the ambient oxygen) wave was measured. We suspect that the low level CIV operation on CRIT-II was due to this non-LHI, which could result in a lower electron heating rate. This low frequency wave should be studied in detail by using the quasilinear theory. A Vlasov computer simulation scheme will be good enough to resolve this problem. According to our theoretical analysis, this low frequency wave was excited by the density inhomogeneity at the leading edge of the barium beam. To avoid this, we suggest that an injection beam with a slow change in density be used in the next flight.

(7) The $(Ba - O^+)$ charge exchange ionization accounted for about half of the total barium ion yields. One of the consequences of this is that the available free energy to ignite the CIV process is increased. We don't know what the barium ion CIV production would have been without the contribution of charge exchange, but it could mess up the CIV ionization process. We suggest that a material with a small charge exchange cross section, for instance the Cesium (Cs), should be considered for the next CIV experiment. Cesium has an atomic weight of 132.9 amu and ionization potential of 3.893 eV to give a critical velocity of 2.4 km/s, which is lower than of Barium (2.7 km/s). The cross section for Cesium impact ionization has also been measured [Heil and Scott, 1966], it has a maximum cross section of $1.0 \times 10^-16\ cm^2$ around 10 eV. Also, the cross section for $(Cs - O^+)$ charge exchange is expected to be small because the smallest energy defect is found to be very large at 2.582 eV. Another alternative is to reduce the beam velocity (reduce the cross section of charge exchange) but keep the beam velocity still higher than the acoustic

speed of the ambient plasma, where the lower hybrid instability starts to operate. Since the wave length of the lower hybrid waves is proportional to the beam velocity, reducing the beam velocity is equivalent to reducing the parallel wavelength for the maximum growth will be reduced. However, the negative effect is that the growth *rate* of the lower hybrid waves will decrease.

Appendix A

CRIT-II Sequence of Events

Table A.1: BBX 35.019 UE (3-Fin) Sequence of Events

Event	Time(seconds)	Timer
BBVB ignition	12.00	I/H
Nihka separation	86.00	I/H
Despin	112.00	I/H
Nose cone ejection	114.00	Daughter
Separation/ACS on	115.00	I/H
LEO fire	116.50	Nose cone
Strobe light on	130.00	C.M. 1
Daughter booms deployment	142.00	Daughter
Daughter deploy	147.00	Daughter
Daughter HV on	175.00	Daughter
Deploy Chem. No. 1	180.00	Mother
Deploy Chem. No. 2	185.00	Mother
Deploy SAAB and Weitzmann doors	190.00	Mother
Deploy particle detector doors	195.00	Mother
Deploy SAAB booms	200.00	Mother
Deploy Weitxmann booms	205.00	Mother
Deploy particle detectors	240.00	Mother
Mother HV on	270.00	Mother
ACS gas off	335.00	ACS
Enable Chem. No.2 firing circuit	340.00	C.M. 2
All fire detonate Chem. No.2	355.00	C.M. 2
ACS gas on	372.00	ACS
ACS gas off	425.00	ACS
Enable Chem. No.1 firing circuit	430.00	C.M. 1
All fire detonate Chem. No.1	445.00	C.M. 1

Appendix B

Photometer Raw Data

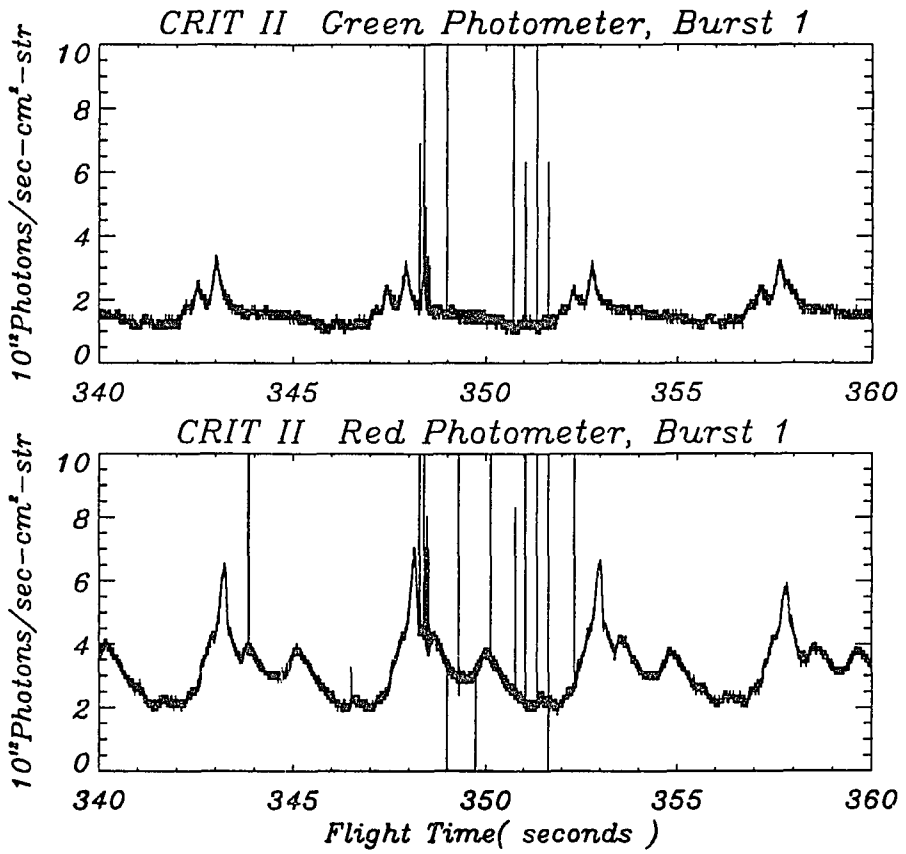

Figure B.1: Brightness from the "Green" and "Red" Photometers in the first release of the CRIT-II experiment.

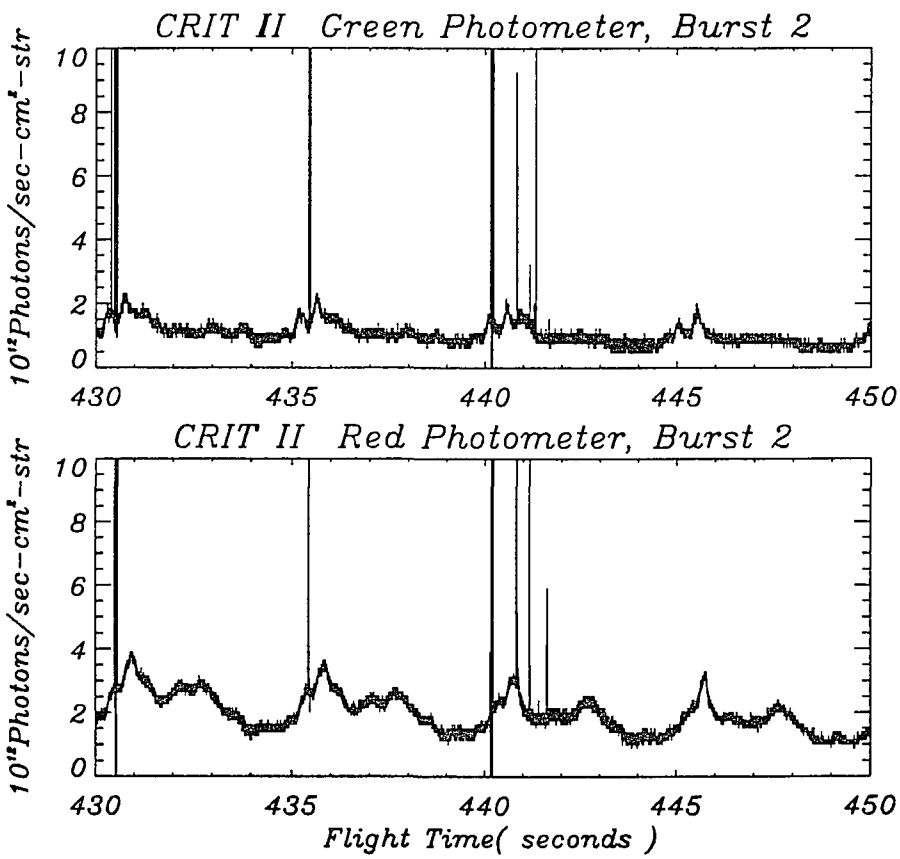

Figure B.2: Brightness from the "Green" and "Red" Photometers in the second release of the CRIT-II experiment.

REFERENCES

Alfvén, H., *On the Origin of the Solar System*, Clarendon Press, Oxford, New York, 1954.

Alfvén, H., Collision between a non-ionized gas and a magnetized plasma, *Rev. Mod. Phys.*, *32(4)*, 710–713, 1960.

Ames, W. F., *Numerical Method for Partial Differential Equations*, Oxford University Press, New York, 1977.

Angerth, B., U. Fahleson, L. Block, and K. Soop, Experiments with partly ionized rotating plasmas, *Nucl. Fusion Suppl., Pt. 1*, 39–46, 1962.

Axnäs, I. and N. Brenning, Experiments on the magnetic field and neutral density limits on CIV interaction, *Adv Space Res.*, *10(7)*, 27–32, 1990.

Axnäs, I., Experimental investigations of an ionizing wave in a coaxial plasma gun, Technical report, Royal Institute of Technology, Stockholm, TRITA-EPP-72-31, 1972.

Axnäs, I., Experimental investigation of the critical ionization velocity in gas mixtures, *Astrophys. Space Sci.*, *55*, 139–146, 1978.

Axnäs, I., The radial variation of the ionization in a coaxial plasma gun operated under critical velocity conditions, Technical report, Royal Institute of Technology, Stockholm, TRITA-EPP-81-07, 1981.

Bagenal, F. and J. D. Sullivan, Dircet plasma measurenents in the Io torus and inner magnetosphere of Jupiter, *J. Geophys. Res.*, *86(A10)*, 8447–8466, 1981.

Banks, P. M., P. R. Williamson, and W. J. Raitt, Space shuttle glow observations, *Geophys. Res. Lett.*, *10(2)*, 118–121, 1983.

Brenning, N., C. -G. Fälthammar, G. Haerendel, M. Kelley, G. Marklund, R. Pfaff, J. Providakes, H. C. Stenbaek-Nielson, C. Swenson, R. B. Torbert, and E. M. Wescott, Critical ionization velocity interaction in the CRIT-I rocket experiment, *Adv. Space Res.*, *10(7)*, 63–66, 1990.

Brenning, N., C. -G. Fälthammar, G. Haerendel, M. Kelley, G. Marklund, R. Pfaff, J. Providakes, H. Stenbaek-Nielsen, C. Swenson, R. Torbert, and E. Wescott, Interpretation of the electric fields measured in an ionospheric critical ionization velocity experiment, *J. Geophys. Res.*, *96(A6)*, 9719–9733, 1991a.

Brenning, N., M. Kelley, J. Providakes, H. Stenbaek-Nielsen, , and C. Swenson, Barium swarm: An ionospheric alternation current generator in CRIT I, *J. Geophys. Res., 96(A6)*, 9735–9743, 1991b.

Brenning, N., Experiments on the critical ionization velocity interaction in weak magnetic field, *Plasma Phys., 23*, 967–977, 1981.

Brenning, N., Review of the CIV phenomenon, *Space Science Reviews, 59*, 209–314, 1992.

Bridge, H. S., J. W. Belcher, A. J. Lazarus, J. D. Sullivan, R. L. McNutt, F. Bagenal, J. D. Scudder, E. C. Sittler, G. L. Siscoe, V. M. Vasyliunas, C. K. Goertz, and C. M. yeates, Plasma observations near Jupiter: Initial results form Voyager 1, *Science, 204*, 987, 1979.

Brown, R. A., Optical line emission from Io, in *Exploration of Planetary System*, A. Woszczyke and C. Iwaniszewska, editors, L. Reidel Publ. Co., Dordrecht, Holland, 1974.

Burden, R. L. and J. D. Faires, *Numerical Analysis*, Prindle, Weber & Schmidt, Boston, 1985.

Carlson, C. W., D. W. Curtis, G. Paschmann, and W. Michael, An instrument for rapidly measuring plasma distribution functions with high resolution, *Adv. Space Res., 12(7)*, 67–70, 1983.

Chang, T. -F., H. U. Rahman, and R. S. White, Laboratory simulation of cometary neutral gas ionization, *J. Geophys. Res., 94(A5)*, 5533–5538, 1989.

Chen, S. T. and Alan Gallagher, Excitation of the Ba and Ba^+ resonance lines by electron impact on Ba atoms, *Physical Review A, 14(2)*, 593–601, 1976.

Cloutier, P. A., R. E. Daniell, A. J. Dessler, and T. W. Hill, A cometary ionosphere model for IO, *Astrophys. Space Sci., 55*, 93–112, 1978.

Danielsson, L. and N. Brenning, Experiment on the interaction between a plasma and a neutral gas. II, *Phys. Fluids, 18(6)*, 661–671, 1975.

Danielsson, L. and G. H. Kasai, Laboratory simulation of plasma phenomena in comets, *J. Geophys. Res., 73*, 259–266, 1968.

Danielsson, L., Experiment on the interaction between a plasma and a neutral gas, *Phys. Fluids, 13(9)*, 2288–2294, 1970.

Danielsson, L., Review of the critical velocity of gas-plasma interaction I: Experimental observations, *Astrophys. Space Sci., 24*, 459–485, 1973.

Davidson, R. C., *Methods in nonlinear plasma theory*, Academic Press, New York, 1972.

Deehr, C. S., E. M. Wescott, H. Stenbaek-Nielson, G. J. Romick, T. J. Hallinan, and H. Föppl, A critical velocity interaction between fast barium and strontium atoms and the terrestrial ionospheric plasma, *Geophys. Res. Lett., 9(3)*, 195–198, 1982.

E. C. Sittler, Jr., K. W. Ogilvie, and J. D Scudder, Survey of low-energy plasma electrons in saturn's magnetosphere: Voyaters 1 and 2, *J. Geophys. Res., 88(A11)*, 8847–8870, 1983.

Eninger, J., Experimental investigations of an ionizing wave in cross electric and magnetic fields, *Proc. 7th Int. Conf. Phen. Ioniz. Gases, Belgrade, 1*, 520, 1966.

Fahleson, U. V., Experiments with plasma moving through neutral gas, *Phys. Fluids, 4(1)*, 123–127, 1961.

Formisano, V., A. A. Galeev, and R. Z. Sagdeev, The role of the critical ionization in the production of inner coma cometary plasma, *Planet. Space Sci., 30*, 491–497, 1982.

Galeev, A. A. and I. C. Chabibrachmanov, Origin and energetics of the Io plasma torus, *Adv. Space Res., 3(3)*, 71–75, 1983.

Galeev, A. A., K. I. Gringaus, S. I. Klimov, A. P. Remizov, R. Z. Sagdeev, S. P. Savin, A. Yu. Sokolov, M. I. Verigin, and K. Szgo, Critical ionization velocity effects in the inner coma of comet Halley: Measurements by Vega-2, *Geophys. Res. Lett., 13(8)*, 845–848, 1986.

Goertz, C. K., S. Machida, and G. Lu, On the theory of CIV, *Adv. Space Res., 10(7)*, 33–45, 1990.

Goretz, C. K., S. Machida, and R. A. Smith, An asymptotic state of the critical ionization velocity phenomenon, *J. Geophys. Res., 90*, 12230–12234, 1985.

Haerendel, G., Plasma flow and critical velocity ionization in cometary comae, *Geophys. Res. Lett., 13(3)*, 255–258, 1986.

Haerendel, G., Alfven's critical velocity effect tested in space, *Z. Naturforsch. A, 37*, 728–735, 1982a.

Haerendel, G., Critical velocity experiments in space, *on the porceedings of on Alfvén's Critical Velocity Effect*, 1982b, Max Planck-institut für Extraterrestrische Physik, Garching bei Munich, Federal Republic of Germany.

Heil, H. and B. Scott, Cesium ionization cross section from threshold to 50 ev, *Phys. Rev., 145(1)*, 297–284, 1966.

Heppner, J. P. and L. H. Meredith, Nightgrow emission altitudes from rocket measurements, *J. Geophys. Res., 63(1)*, 51–65, 1958.

Himmel, G. and A. Piel, The velocity limitation in a rotating plasma device of the homopolar type, *J. Phys. D: Appl. Phys*, *6*, L108–L111, 1973.

Himmel, G., E. Möbius, and A. Piel, Investigation of the particle velocities in a "critical velocity" rotating plasma, *Z. Naturforsch*, *32(A)*, 577–579, 1977.

Huebner, K. H. and E. A. Thornton, *The Finite Element Method for Engineers*, John Wiley & Sons, New York, 1982.

Ishihara, O. and A. Hirose, High-energy ion tail formation in the ion-acoustic instabiblity– three dimensional quasilinear approach, *Phys. Fluids*, *26(1)*, 100, 1983.

Kelley, M. C., R. F. Pfaff, and G. Haerendel, Electric field measurements during the condor critical velocity experiment, *J. Geophys. Res.*, *91(A9)*, 9939–9946, 1986.

Kelley, M. C., C. Swenson, N. Brenning, K. Baker, and R. Pfaff, Electric and magnetic field measurements inside a high velocity neutral beam undergoing ionization, *J. Geophys. Res.*, *96(A6)*, 9703–9718, 1991.

Kennel, C. F. and F. Englemann, Velocity space diffusion from weak plasma turbulence in a magnetic field, *Phys. Fluids*, *9(12)*, 2377–2388, 1966.

Kliore, A., K. L. Cain, G. Fjeldbo, B. L. Seidel, and S. I. Rasool, Preliminary results on the atmospheres of Io and Jupiter from the Pioneer 10 S-band occultation experiment, *Science(USA)*, *183(4122)*, 323–324, 1974.

Lopez-Moreno, J. J., S. Vidal, R. Rodrigo, and E. J. Llewellyn, Rocket borne photometric measurements in the $O_2(^1\Delta g)$ green line and OH meinel bands in the night glow, *The Tenth Annual Meeting on the Study of the Atmosphere by Optical Methods, Grasse, France*, September 1982.

Machida, S. T. and C. K. Goertz, A simulation study of the critical ionization velocity, *J. Geophys. Res.*, *91*, 11965–11976, 1986.

Machida, S. and C. K. Goertz, The electromagnetic effect on the critical ionization velocity process, *J. Geophys. Res.*, *93*, 11945–11506, 1988.

Massey, H. S. W., E. H. S. Burhop, and H. B. Gilbody, *Electronic and Ionic Impact Phenomena, 2nd ed., Vol. 1-5*, Oxford Univ. Press, London and New York, 1970-1974.

McBride, J. B., E. Ott, J. P. Boris, and J. H. Orens, Theory and simulation of turbulent heating by the modified two-stream instability, *Phys. Fluids*, *15(12)*, 2367–2383, 1972.

Mende, S. B., O. K. Garriott, and P. M. Banks, Observations of optical emissions on sts-4, *Geophys. Res. Lett.*, *10(2)*, 122–125, 1983.

Mendis, D. A., H. L. F. Houpis, and M. L. Marconi, The physics of comets, *Fundamentals of Cosmic Physics, 10*, 1–380, 1985.

Mikhailovskii, A. B., *Theory of Plasma instabilities, Vol. 2*, Consultants Bureau, New York, 1974.

Möbius, E., A. Piel, and G. Himmel, Determination of the plasma parameters and the suprathermal microfields in a critical velocity rotating plasma, *Z. Naturf., 23(a)*, 405, 1979.

Möbius, E., K. Papadopoulos, and A. Piel, On the turbulent heating and the threshold conditions in the critical ionization velocity interaction, *Planet. Space Sci, 35*, 345–352, 1987.

Möbius, E., Ph.D. thesis, Ruhr-Universität Bochum, 1977.

Möbius, E., Critical velocity experiments in space, Active Experiments in Space Symposium in Alpbach, 24-28 May, 1983, *ESA SP-195*, pages 215–266, 1983.

Morfill, G. E., O. Havnes, and C. K. Goertz, Origin and maintenance of the oxygen torus in Saturn's magnetosphere, *J. Geophys. Res., 98(A7)*, 11285–11297, 1993.

Newell, P. T. and R. B. Torbert, Competing atomic processes in Ba and Sr injection critical velocity experiments, *Geophys. Res. Lett., 12*, 835–838, 1985.

Newell, P. T., *A magnetospheric critical ionization velocity experiment*, Ph.D. thesis, University of California, San Diego, La Jolla, California, 1985.

Newell, P. T., Review of the critical ionization velocity effect in space, *Rev. Geophys., 23*, 93–104, 1985.

Papadopoulos, K., Electron and ion driven plasma discharges with collective dissipation, *on the porceedings of on Alfvén's Critical Velocity Effect*, page 178, 1982, Max Planck-institut für Extraterrestrische Physik, Garching bei Munich, Federal Republic of Germany.

Papadopoulos, K., On the shuttle glow (the plasma alternative), *Radio Science, 19(2)*, 571–577, 1984.

Papadopoulos, K., The CIV processes in the CRIT experiments, *Geophys. Res. Lett., 19(6)*, 605–608, 1992.

Petelski, E. F., H. J. Fahr, H. W. Ripken, N. Brenning, and I. Axnäs, Enhanced interaction of the solar wind and the interstellar neutral gas by virtue of a critical velocity effect, *Astron. Astrophys., 87*, 20–30, 1980.

Petelski, E. F., Critical ionization velocity and the interaction of stellar winds with the interstellar medium, *Proceedings Solar Wind IV Conference, Burghausen, W. Germany*, 1978.

Petelski, E. F., Viability of the critical ionization velocity concept in selected space situations, in *Relation Between Laboratory and Space Plasmas*, H. Kikuchi, editor, pages 23–44, D. Reidel Publishing Company, Boston, Mass., 1981.

Pfaff, R., M. C. Kelley, N. Brenning, J. Providakes, C. Swenson, and R. B. Torbert, Plasma waves created by a heavy neutral/ion beam in the mid-latitude ionosphere, *J. Geophys. Res., to be Submitted*, 1992.

Piel, A., E. Möbius, and G. Himmel, The origin of turbulent heating in a critical velocity rotating plasma, research report 78-m2-037, Technical report, Inst. für Experimentalphysik II der Ruhr- Universität Bochum, 1978.

Piel, A., E. Möbius, and G. Himmel, The influence of the the plasma inhomogeneity on the critical velocity phenomenon, *Astrophys. Space Sci.*, *72*, 211–221, 1980.

Podgorny, I. M. and R. Z. Sagdeev, Physis of interplanetary ionization velocity mechanism, *Sov. Phys. Usp.*, *98*, 445, 1970.

Pontius, D. H. and T. W. Hill, Departure from corotation of the Io plasma torus : local plasma production, *Geophys. Res. Lett.*, *9*, 1321–1324, 1982.

Press, W. H., B. P. Flannery, S. A. Teukolsky, and W. T. Vetterling, *Numerical Recipes*, Cambridge University Press, New York, 1986.

Raadu, M. A., The role of electrostatic instabilities in the critical ionization velocity mechanism, *Astrophys. Space Sci.*, *55*, 125–138, 1978.

Raadu, M. A., The critical ionization velocity, in *Relation between laboratory and space plasmas*, H. Kikuchi, editor, pages 13–21, D. Reidel Publishing Company, Boston, Mass., 1981.

Rutherford, R. F., R. F., and D. A. Vroom, Formation of iron ions by charge transfer, *J. Chem. Phys.*, *57*, 3091, 1972.

Rutherford, R. F., R. F. Mathis, B. R. Turner, and D. A. Vroom, Formation of calcium ions by charge transfer, *J. Chem. Phys.*, *57*, 3087, 1972b.

Scholer, M., On the motion of artificial ion clouds in the magnetosphere, *Planet. Space Sci.*, *18*, 977–1004, 1970.

Seyler, C. E., Lower hybrid waves and ionospheric spikelets, *Eos Trans. AGU*, *74*, 532, 1993.

Sherman, J. C., The critical velocity of gas-plasma interactions and its possible hetegonic relevance, in *Nobel. Symp. No.21*, Almqvist and Wiksell, editors, page 315, Academic press, New Youk, 1972.

Sherman, J. C., Review of the critical velocity of gas-plasma interaction II: Theory, *Astrophys. Space Sci.*, *24*, 487–510, 1973.

Singh, N., Simulations of field-aligned plasma expansions in CIV experiments, *Adv. Space Res., 10(7)*, 59–62, 1990.

Slanger, T. G., Conjectures of the origin of the surface glow of space vehicles, *Geophys. Res. Lett., 10(2)*, 130–133, 1983.

Smirnov, B. M., *Introduction to Plasma Physics*, Engl. Transl., Mir Publishers, Moscow, 1977.

Stegman, J., G. Witt, E. J. Llewellyn, T. H. G. Dickenson, and D. B. Jenkins, On the triplet states of molecular oxygen in the upper atmosphere, *The Tenth Annual Meeting on the Study of the Atmosphere by Optical Methods, Grasse, France*, September 1982.

Stenbaek-Nielsen, H. C., D. Rees E. M. Wescott, A. Valenzuela, and N. Brenning, Non-solar UV produced ions observed optically from the "CRIT-I" critical velocity ionization experiment, *J. Geophys. Res., 95(A6)*, 7749–7757, 1990.

Stenbaek-Nielsen, H. C., E. M. Wescott, G. Haerendel, and A. Valenzuela, Optical observations on the CRIT-II critical ionization velocity experiment, *Geophys. Res. Lett., 17(10)*, 1601–1604, 1990.

Stenbaek-Nielsen, H. C., E. M. Wescott, and T. J. Hallinan, Observed barium emission rates, *J. Geophys. Res., 98(A10)*, 17491–17500, 1993.

Stenbaek-Nielsen, H. C., Barium and strontium releases in the ionosphere, *on the porceedings of on Alfvén's Critical Velocity Effect*, 1982, Max Planck-institut für Extraterrestrische Physik, Garching bei Munich, Federal Republic of Germany.

Swanson, D. G., *Plasma Waves*, Academic Press, San Diego, CA, 1989.

Swenson, C. M., M. C. Kelley, F. Primdahl, and K. D. Baker, CRIT II electric, magnetic, and density measurements within an ionizing neutral stream, *Geophys. Res. Lett., 17(12)*, 2337–2340, 1990.

Swenson, G. R., S.B. Mende, R. E. Meyerott, and R. L. Rairden, Charge exchange contamination of CRIT II barium CIV experiment, *Geophys Res. Lett., 18(3)*, 401–403, 1991.

Swenson, C. M., *In-situ Observation of an Ionospheric Critical Velocity Experiment*, Ph.D. thesis, Cornell University, 1992.

Tanaka, M. and K. Papadpoulos, Creation of high-energy electron tails by means of the modified two-stream instability, *Phys. Fluids, 26*, 1697, 1983.

Thomas, L. D. and R. K. Nesbet, Low-energy electron scattering by atomic oxygen, *Phys. Rev. A, 1175*, 170–173, 1975.

Torbert, R. B. and P. T. Newell, A magnetospheric critical velocity experiment: particle results, *J. Geophys. Res., 91*, 9947–9955, 1986.

Torbert, R. B., C. A. Kletzing, K. Liou, and R. David, Prompt ionization in the CRIT II barium releases, *Geophys. Res. Lett*, *19*, 973, 1992.

Torbert, R. B., Critical velocity effect in ionospheric shaped-charge releases, *Eos Trans. AGU*, *68*, 1424, 1987.

Torr, M. R., Optical emissions induced by spacecraft-atmosphere interactions, *Geophys. Res. Lett.*, *10(2)*, 114–117, 1983.

Vainshtein, L. A., V. I. Ochkur, V. I. Rakhovskii, and A. M. Stepanov, Absolute values of electron impact ionization cross sections for magnesium, calcium, strontium and barium, *Soviet Physics JETP, Engl. Transl.*, *34*, 271–275, 1972.

Wallis, D. D. and C. D. Anger, High-altitude observations of a luminous wake behind two Black Brant II rockets, *Can. J. Phys.*, *46*, 2753, 1968.

Wallis, Max K., Comet-like interaction of Venus with the solar wind, I, *Cosmic Electrodynamics*, *3*, 45–49, 1972.

Wescott, E. M., E. P. Rieger, H. C. Stenbaek-Nielsen, and T. N. Davis, The L=6.7 quiet time barium shaped charge injection experiment "Chachalaca", *J. Geophys. Res.*, *80(19)*, 2738–2744, 1975.

Wescott, E. M., H. C. Stenbaek-Nielsen, T. Hallinan, C. S. Deehr, J. Romick, J. Olson J. G. Roederer, and R. Sydora, A high altitude barium radial injcetion experiment, *J. Geophys. Res.*, *7(12)*, 1037–1040, 1980.

Wescott, E. M., H. Stenbaek-Nielsen, D. W. Swift, A. Valenzuela, and D. Rees, SR90, strontium shaped-charge critical ionization velocity experiment, *J. Geophys. Res.*, *95(A12)*, 21069–21075, 1990.

Wescott, E. M., H. C. Stenbaek-Nielsen, D. Hampton, and P. Delemere, Results of critical velockty experiments with barium, strotium and calcium releases from CRRES satellite, *J. Geophys. Res., to be submitted*, 1993.

Wescott, E. M., H. C. Stenbaek-Nielsen, T. Hallinan, H. Föppl, and A. Valenzuela, Star of lima: Overview and optical diagnostics of a barium Alfvén critical velocity experiment, *J. Geophys. Res.*, *91(A9)*, 9923–9931, 1986a.

Wescott, E. M., H. C. Stenbaek-Nielsen, T. Hallinan, H. Föppl, and A. Valenzuela, Star of Condor: A strontium critical velocity experiment, Peru, 1983, *J. Geophysical Res.*, *91(A9)*, 9933–9938, 1986b.

Wilcox, J. M., E. Pugh, A. Datiner, and J. Eninger, Experimental study of the propagation of an ionizing wave in a coaxial plasma gun, *Phys. Fluids Suppl.*, *7*, S51–S56, 1964.

Wurm, K., Die natur der koneten, *Mitt. Hamburg. Sternw.*, page 51, 1943.

Yee, J. H. and V. J. Abreu, Visible glow induced by spacecraft-environment interaction, *Geophys. Res. Lett.*, *10(2)*, 126–129, 1983.